

A First Principles Study of Paramagnetic Defects in Diamond

by Khaled Mohamed Etmimi

A thesis submitted to Newcastle University for the degree of Doctor of Philosophy.
December 2010.

Dedicated to
My wife, Mum, Dad and Sons.

Declaration

This thesis has not previously been submitted by the candidate for a degree in this or any other university.

K. M. Etmimi
December 2010.

Acknowledgements

First of all I thank my God for giving me the strength and guidance during my studies. I would also like to thank my supervisors, Dr. Jonthan Goss and Dr. Patrick Brodden, for their assistance and support throughout my studies and for giving me opportunity to be part of the research group. I will not forget the help you gave me during my studies, and I really appreciate your efforts and trying to be there whenever I needed your help. I would like to thank my wife, and my Mum and Dad, sisters and brothers for their love and support. Also my thanks to Dr. Jerry for his help throughout my first year. I also thank all of the past and present AIMPRO group.

Abstract

Diamond is a radiation-hard material with a wide band-gap which is typically electrically insulating. A wide range of diamond-based material is available, including natural gemstones and synthetic diamond manufactured by chemical vapour deposition (CVD) and high pressure and temperature (HPHT) techniques. The wide band-gap and electrical insulation properties mean that defects introduced by irradiation and plastic deformation, during growth or otherwise, may exist in more than one charge and/or electronic-spin state. Of these, defects with unpaired electrons give rise to characteristic spectroscopic signatures in electron paramagnetic resonance (EPR) experiments. In favourable situations these spectra provide chemical specificity, defect symmetry, effective spin-state, and wave function character (such as sp hybridisation), and when combined with temperature effects can yield data relating to thermal stability (for example binding and migration energies) and temperature dependent symmetry effects.

Recent advances in quantum chemical simulation allow for reasonable accuracy in simulated hyperfine interaction (HFI) tensors (electron-spin and nuclear-spin interactions). Indeed, many assignments for EPR centres are tentative in nature. Where the proposed model yields calculated hyperfine values that differ substantially from those measured, in addition

to refuting the current model, an examination of a wide range of candidate defects may lead to more realistic models. Defects observed in natural and synthetic diamonds provide a finger-print of their differing growth conditions, as well as the thermal and mechanical processes they have experienced.

A challenge that has existed for decades in the effort to produce diamond suitable for electronics is in overcoming the difficulty in production of low resistivity n-type material. N, a dopant one might naively assume would be effective, undergoes a significant structural relaxation, rendering it a very deep donor at around $E_c - 1.7$ eV. Phosphorus is a better candidate since the substantial difference in atomic radius relative to the host suppresses large structural relaxations associated with nitrogen. However, with a donor level at around 0.6 eV below the conduction band, it has a low ionisation fraction at room temperature.

This thesis presents the results of calculations performed with the ab initio modelling (AIMPRO) code. The initial stages studied the stability, defect symmetry, Kohn Sham orbitals and the hyperfine interaction of di-nitrogen substitutionals diamond. Analysis was then conducted of nitrogen pair defects relating to published theoretical and experimental models of W24, N1, W7, M2, N4 and M3 electron-paramagnetic-resonance centres in diamond in which pairs of nitrogen donors are separated by different numbers of intervening host sites, both in ionised $S = 1/2$ and neutral $S = 1$ forms. Using density functional techniques, these models are confirmed, but in order to do so for the N4 centre, for example, it is shown to be essential that extremely low energy reorientation takes place. Charge exchange and chemical re-bonding effects also provide an explanation for the distinct forms of the $S = 1$ neutral configurations observed.

Other proposed models were then considered, including a detailed analysis of the hyperfine interactions for muonium centres, including the effects of vibration. This was combined with the experimental examination of N-containing diamond, where muon-spin relaxation experiments suggest a strong interaction between N-aggregates and the implanted muon.

Structures made from two arrangements of pairs of substitutional nitrogen and oxygen showed no direct evidence for the involvement of the oxygen. The proposed model for N3 broadly agreed with experimental results but not for the OK1 centre.

Despite its high ionisation energy, the n-type dopant of choice in diamond is currently phosphorus. Chemical vapour deposited diamond can be grown with high concentrations of P, and the substitutional donor has been characterised via a number of experimental techniques including electron paramagnetic resonance. Substitutional P undergoes a Jahn-Teller distortion at low temperature, where the EPR tensors reflect a tetragonal symmetry. Other P-containing EPR centres have also been detected but their structure remains uncertain.

Contents

Abstract	iv
Table of Contents	xi
List of Figures	xvii
List of Tables	xxi
List of Publications	xxii
1 Introduction	1
1.1 Introduction	1
1.2 Properties of Diamond	2
1.3 Classification of Diamond	4
1.4 Defects in Diamond	7
1.5 Diamond Synthesis	8
1.5.1 High pressure high temperature (HPHT)	8
1.5.2 Chemical vapour deposition (CVD)	9

1.5.3	Applications of Diamond	10
1.6	Thesis Summary	11
1.6.1	Part I: Theoretical Framework	11
1.6.2	Part II: Applications	12
1.6.3	Part III: Conclusions	13
1.7	Abbreviations and Acronyms	14
I	Theoretical Framework	15
2	Background Theory and AIMPRO Modelling Package	16
2.1	Introduction	16
2.2	The Many Body Problem	17
2.3	Born-Oppenheimer Approximation	17
2.4	The Hartree Approximation	17
2.5	The Hartree-Fock Approximation	18
2.6	Density Functional Theory	19
2.6.1	Hohenberg-Kohn theorems	19
2.6.2	The Kohn-Sham approach	21
2.6.3	The exchange-correlation functional	22
2.7	Pseudopotentials	23
2.8	Supercell Approach	24
2.9	Brillouin Zone Sampling	25
2.10	Basis Sets	26
2.11	Self-Consistency Approach	26
2.12	Structural Optimisation	27
3	Modelling of Experimental Observables	28
3.1	Introduction	28
3.2	Diffusion Method in AIMPRO	29
3.3	Vibrational Modes	29

3.4	Electrical Levels	31
3.4.1	Marker method	31
3.4.2	Formation energy method	31
3.5	Electron Paramagnetic Resonance	32
3.6	Hyperfine Interactions	35
3.7	Muon Spin Relaxation (μ SR)	39
3.8	Conclusion	40
II	Applications	41
4	Nitrogen-Pair Paramagnetic Defects	42
4.1	Introduction	42
4.2	Methodology	45
4.3	Computation results	47
4.3.1	First-shell pairs and W24	49
4.3.2	Second-shell pairs and N1	49
4.3.3	Third-shell pairs and W7	54
4.3.4	Fourth-shell pairs and M2	58
4.3.5	Fifth-shell pairs and N4	60
4.3.6	Sixth-shell pairs and M3	63
4.3.7	Seventh-shell pairs	68
4.3.8	Eighth-shell pairs	70
4.3.9	Ninth- and tenth shell pairs: NOC-3 and NOC-1	72
4.4	Discussion	73
4.4.1	Total energies	73
4.4.2	Electrical activity: why are the dissociated pairs in the positive charge state?	74
4.4.3	Ferro- vs anti-ferromagnetic interactions for neutral pair	75
4.5	Conclusions	77

5	Muonium and Hydrogen in Nitrogen-Aggregate containing diamond: the Mu_x centre	78
5.1	Introduction	78
5.2	Methodology	80
5.3	Computation results	80
5.3.1	Muonium in diamond	80
5.3.2	Muonium N-aggregate complexes	82
5.3.3	Muonium in nitrogen-vacancy complexes	86
5.3.4	Muonium in other sites	86
5.4	Discussion and conclusions	91
6	Nitrogen-Oxygen Pairs in Diamond: the N3 and OK1 EPR Centres	94
6.1	Introduction	94
6.2	Methodology	96
6.3	Computation results	97
6.3.1	The N3 EPR centre	97
6.3.2	The OK1 EPR centre	101
6.4	Conclusions	109
7	Calculated Hyperfine Interaction Parameters for P-Containing Point Defects in Diamond	111
7.1	Introduction	111
7.2	Methodology	113
7.3	Substitutional P	113
7.4	Phosphorus–nitrogen pairs	115
7.5	Phosphorus–boron pairs	116
7.6	Phosphorus–oxygen pairs	118
7.7	Phosphorus–vacancy complexes	119
7.8	Phosphorus pair	121

7.9	Conclusions	122
III	Conclusions	123
8	Summary	124
8.1	Summary	124
	Bibliography	127

List of Figures

1.1	Conventional unit cell of diamond, where a_0 is the lattice constant.	3
1.2	The First Brillouin zone of (a) an FCC lattice (b) an SC lattice, with high symmetry \mathbf{k} -points marked.	5
1.3	Schematics showing the calculated structures of nitrogen defects in diamond. (a) C-centre, (b) A-centre, and (c) B-centre. Blue and grey atoms are nitrogen and carbon respectively. Horizontal and vertical directions are approximately [110] and [001] respectively.	6
1.4	Schematic setup of a system for the production of HPHT synthetic diamonds.	9
1.5	Schematic setup of a system for the production of CVD synthetic diamond. (hot filament for example can be used instead of plasma for ionisation) . . .	10
2.1	Schematic illustrating the pseudo-wave function (top) and the pseudo-potential (bottom) core electrons. The cut-off radius r_c indicates the defined region at which point the systems must match. The pseudo-wave function and potential are plotted with a brown line whilst the true all-electron wave function and core potential are plotted with the red lines.	24

3.1	Schematic shows energy levels of a system with $S = 1/2$ and $I = 1/2$ in applied magnetic field.	34
3.2	Schematic of EPR spectra for an unpaired electron $S = 1/2$ interacting with nuclear spin $I = 1/2$	36
3.3	A spherical coordinate system with origin O.	38
4.1	Schematics showing the calculated structures of nitrogen defects in diamond: (a) ionised C-centre (N_s^+), (b) neutral C-centre (N_s^0), (c) negatively charged C-centre (N_s^-), and (d) A-centre. Labelled sites are N for nitrogen and R indicating the carbon radical or anion site. Horizontal and vertical directions are approximately [110] and [001], respectively. Percentages indicate the calculated extension of the respective interactions over that of the host C–C bond-length. The transparent cylinders represent broken bonds.	43
4.2	The Kohn-Sham band structure in the vicinity of the band-gap for the P1 centre (N_s^0). Filled and empty circles show filled and empty bands respectively, with the bands from the defect-free cell superimposed in full lines for comparison. The energy scale is defined by the valence band top at zero energy ($E_v = 0$ eV). The left and right panels show the spin up and down spectra, respectively. The path of the k -points are illustrated in the Brillouin zone of a simple-cubic (Fig.1.2(b))	44
4.3	Schematics showing shells of neighbours in diamond: (a) sites embedded in the diamond lattice; with (b) showing only prototypical sites for each shell of neighbours relative to the first nitrogen site, N_1 . The two types of seventh-shell site are labelled 7a and 7b in accordance with Ref. [1].	46
4.4	The Kohn-Sham band structure in the vicinity of the band-gap for (N1N). Symbols and scales are as indicated in Fig. 4.2.	50
4.5	Schematics of N2N in diamond in the (a) neutral and (b) positive charge states. Colours and axes are as in Fig. 4.1. (c) The Kohn-Sham band structure in the vicinity of the band-gap for (N2N). Symbols, axes and scales are as indicated in Fig. 4.1 and Fig. 4.2.	51

4.6	The barrier of energy between (N – CN) and (NC – N) in neutral (red line) and positive (black line) charge states.	54
4.7	Kohn-Sham functions for N3N between two neighbouring carbon radicals: (a) partial p_π -bond, and (b) partial p_π^* -bond.	55
4.8	Schematics of the N3N complex in diamond in the (a) neutral and (b) positive charge states, with (c) showing the Kohn-Sham band structure in the vicinity of the band-gap for (N3N). Symbols, axes and scales are as indicated in Fig. 4.1 and Fig. 4.2.	56
4.9	Schematic showing three modes for reorientation as discussed in the text for (N3N) ⁺ . Colours and orientation as in Fig. 4.1.	58
4.10	Schematics of the N4N complex in diamond: (a) and (b) show two forms of the neutral, $S = 0$ state; in (c) the $S = 1$ configuration is assigned to NOC-2; and (d) the lowest energy structure is in the positive charge state. Structures are presented as indicated in Fig. 4.1.	60
4.11	The Kohn-Sham band structure in the vicinity of the band-gap for (N4N). Symbols and scales are as indicated in Fig. 4.2.	61
4.12	The reorientation barrier of (N4N) ⁺ between N sites.	63
4.13	Schematics of the N5N complex in diamond in the (a) neutral and (b) positive charge states. Colours and orientation are as indicated in Fig. 4.1.	63
4.14	The Kohn-Sham band structure in the vicinity of the band-gap for (N5N). Symbols and scales are as indicated in Fig. 4.2.	64
4.15	The reorientation barrier of (N5N) ⁺ between N sites.	64
4.16	Schematics of the N6N complex in diamond in the (a) neutral charge state; (b) and (c) show two forms of positive charge states. Colours and orientation are as indicated in Fig. 4.1.	66
4.17	The Kohn-Sham band structure in the vicinity of the band-gap for (N6N). Symbols and scales are as indicated in Fig. 4.2.	67
4.18	The reorientation barrier of (N6N) ⁺ between N sites.	68

4.19	Schematics of the N7aN and N7bN complexes in diamond: (a) and (b) show two energetically degenerate forms of N7aN; with (c) being the model structure for NOC-3, and (d) shows the most stable structure for N7bN. Colours and orientation are as indicated in Fig. 4.1.	69
4.20	Schematics of the N8N complex in diamond in the (a) neutral and (b) positive charge states. Colours and orientation are as indicated in Fig. 4.1.	70
4.21	The Kohn-Sham band structure in the vicinity of the band-gap for (N8N). Symbols and scales are as indicated in Fig. 4.2.	71
4.22	Schematics of the N9N and N10N complexes in diamond in the neutral charge state. Colours and orientation are as indicated in Fig. 4.1.	73
4.23	Plot of the variation of donor (blue dashed line) with shell-number. The zero of energy is fixed at E_c , and the levels plotted as the ionisation energy relative to this fixed point. The horizontal dot-dashed line at -1.7 eV shows the location of the donor level of isolated N_v^0	74
5.1	Schematics of (a) the Muonium in bond-centre (Mu_{BC}) and (b) the Muonium in tetrahedral site (Mu_T). Vertical and horizontal directions are approximately [001] and [110] respectively. Grey and white atoms are C and H/muonium, respectively.	81
5.2	The barrier of energy between tetrahedral and bond-centred sites.	82
5.3	Schematics of (a) the A-centre, (b) the B-centre, (c) the A-centre–muonium complex, and (d) the B-centre–muonium complex in diamond. Vertical and horizontal directions are approximately [001] and [110] respectively. Small grey, large blue and white atoms are C, N and H/muonium, respectively. The transparent cylinders in (c) and (d) represent broken bonds relative to (a) and (b).	83
5.4	Unpaired electron Kohn-Sham functions for (a) B-centre–muonium complex and (b) neutral substitutional nitrogen (P1 EPR centre). Orientation is as in Fig. 5.3.	85

5.5	Schematics of (a) the H2-centre, (b) the H3-centre ((b) is chemically identical to (a) the only different is extra electron on (a)), (c) the H2-centre–muonium complex, and (d) the H3-centre–muonium complex in diamond. Orientation is as in Fig. 5.3.	87
5.6	The barrier of energy for chemical reaction between the muonium and the lattice in a V_2N_6 cavity.	88
5.7	Schematics showing selected structures of muonium in the platelet defect. The grey and white atoms are carbon and muonium, respectively. Vertical and horizontal directions are approximately [001] and [110] respectively. . .	90
6.1	Schematics of three structures proposed for the N3 EPR centre in diamond: (a) N_s-O_s , (b) NV_2 and (c) N_s-Ti_s . Vertical and horizontal directions are approximately [001] and [110] respectively. Impurities are as labelled with V indicating vacant sites.	98
6.2	Schematic of N_s-C-O_s complexes. Vertical and horizontal directions are approximately [001] and [110] respectively. In each case the impurity on the left is N and that on the right is O. The inter-nuclear interactions best described as broken bonds are shown as transparent sticks, and covalent bonds as solid sticks.	102
6.3	Schematics of models proposed for OK1: (a) the Ti_s-V-N_s and (b) N_s-V-O_s complex. Vertical and horizontal directions are approximately [001] and [110] respectively.	107
7.1	Kohn-Sham iso-surface for the highest occupied orbital of the $D_{2d}(2)$, Jahn-Teller distorted configuration of substitutional P in diamond.	114
7.2	Schematics of phosphorus-nitrogen complexes in diamond: (a) $(P-N)^+$ and (b) $(P-C-N)^+$. In both cases the structures may be viewed as $P_s^+-N_s^0$ pairs, leading to the approximate axial symmetry for the dilated N–C bond. Horizontal and vertical directions are [110] and [001] respectively.	116

7.3	Schematics of phosphorus-boron complexes (a) The ionised (P–B) ⁺ and (b) The ionised (P–C–B) ⁺	117
7.4	Schematics of phosphorus-oxygen complexes in diamond: (a) P–O and (b) P–C–O. In both cases the structures may be viewed as P _s ⁺ –O _s [–] pairs in the overall neutral charge state. Horizontal and vertical directions are [110] and [001] respectively.	119
7.5	Schematic showing the P–V structure and the directions of the three components of the hyperfine interactions at P and a neighbouring C site.	120
7.6	Schematic showing the P–N–P structure and the directions of the three components of the hyperfine interactions at P and a neighbouring C sites.	122

List of Tables

3.1	Muon compared to proton.	40
3.2	Muonium compared to hydrogen.	40
4.1	Relative energies for different structures with different cell size (216 and 512), wave function basis ($C44G^*$ and $pdpp$) and \mathbf{k} -points (MP222 and MP444). The zero of energy is set to the A-centre (N1N).	48
4.2	Hyperfine tensors (MHz) for ^{14}N and their six ^{13}C neighbours in (N1N) $^+$. Directions are indicated in parentheses using spherical polar coordinates. Experimental data for W24 are taken from Ref. [2]. All calculated data are rounded to the nearest MHz or degree.	48
4.3	Calculated hyperfine tensors (MHz) for ^{14}N and ^{13}C , for the sites identified in Fig. 4.5. Tensors are listed as in Table 4.2, and the experimental data for N1 are taken from Ref. [3].	52
4.4	^{13}C hyperfine for sites in N2N (Fig. 4.5), and those obtained experimentally for the N1 EPR centre, with labels and values taken from Refs. [4, 5]. n indicates the number of equivalent sites in each case.	53

4.5	Calculated hyperfine tensors (MHz) for ^{14}N and ^{13}C , for the sites identified in Fig. 4.8. Experimental data are taken from Ref. [6]. Notation is as in Table 4.3. The motional averages are indicated as dynamic values for A , with the two cases as indicated in the text.	57
4.6	Calculated hyperfine tensors (MHz) for ^{14}N and ^{13}C , for the sites identified in Fig. 4.10(d). Experimental data are taken from Ref. [7]. Notation is as in Table 4.3. The orientation of the centre has been chosen to match the experimental data.	62
4.7	Calculated hyperfine tensors (MHz) for ^{14}N and ^{13}C , for the sites identified in Fig. 4.13. Experimental data taken from Ref. [5]. Notation is as in Table 4.3.	65
4.8	Calculated hyperfine tensors (MHz) for ^{14}N and ^{13}C , for the sites identified in Fig. 4.16(b). Experimental data are taken from Ref. [7], notation is as in Table 4.3, and the defect crystallographic orientation has been chosen to facilitate comparison with experimental values.	67
4.9	Calculated hyperfine tensors (MHz) for ^{14}N and ^{13}C , for the sites identified in Fig. 4.20(b). Notation is as in Table 4.3.	72
5.1	Calculated hyperfine tensors of Mu_T and Mu_{BC} (MHz). f is the ratio of the isotropic hyperfine interaction for the defect to that for muonium in vacuum (4463 MHz).	82
5.2	Calculated hyperfine tensors of muonium-complexes with A- and B-centres (MHz). The directions are indicate in spherical polar coordinates, θ degrees from the z - axis, and ϕ from the x -axis toward y in the xy -plane.	84
5.3	Calculated hyperfine tensors for muonium in a range of model cavities (MHz). f and f' are ratios of A_s to the experimental and calculated values for free muonium respectively. The experimental values for Mu_X are shown for comparison.	89
5.4	Calculated hyperfine tensors for muonium in a model platelet, (MHz), for the structures presented in Fig. 5.7.	91

6.1	Hyperfine tensors for ^{14}N , ^{17}O and ^{47}Ti based upon the models for the N3 centre depicted in Fig. 6.1. In each case the magnitude (MHz) precedes the spherical-polar angles θ and ϕ in parentheses, where θ is relative to [001], and ϕ is measured from [100] toward [010] in the xy -plane. θ' is the magnitude of the angle A makes with $\langle 110 \rangle$ within the mirror plane. Experimental values are taken from Ref. [8]. (s) and (d) indicate the values for static and dynamically reorientating geometries respectively, as described in the text.	100
6.2	Calculated relative energies (E^{rel} , eV) of ^{14}N hyperfine tensors (MHz) for structures in Fig. 6.2. In each case, θ and ϕ are given as indicated in Table 6.1, θ' indicates the directions of A_{\parallel} with $\langle 110 \rangle$ for axially symmetric tensors. Experimental parameters for ^{14}N in OK1 are taken from ref. [9]. Where a range of structures is indicated, the corresponding hyperfine tensors represent an average over these geometries. For averages involving (a), both the form shown and its symmetric equivalent reflected in the $(1\bar{1}0)$ plane are included.	104
6.3	Calculated hyperfine tensors of ^{13}C in N-C-O complexes as shown in Fig. 6.2 (MHz). θ and ϕ are given as indicated in Table 6.1, θ' indicates the directions of A_{\parallel} with [001] for axially symmetric tensors. Experimental values are from Ref. [10].	105
6.4	Calculated ^{17}O hyperfine tensors (MHz) for structures in Fig. 6.2, as specified in Table 6.2.	106
6.5	Hyperfine tensors for the Ti-V-N and NVO complexes (MHz). θ and ϕ are as indicated in Table 6.1, θ' is the angle A_{\parallel} makes with $\langle 110 \rangle$ within the mirror plane for axially symmetric tensors. Experimental values are taken from Refs. [8, 11, 12]	108
7.1	Hyperfine tensor magnitudes (MHz) and directions in spherical polar angles for ^{31}P in substitutional P in diamond for different distortions. Symmetries follow the labelling in Ref. [13].	115

7.2	Calculated isotropic (A_s) and anisotropic (A_p) hyperfine interactions (MHz) of ^{31}P , the under-co-ordinated ^{13}C and ^{14}N in $(\text{P-N})^+$ and $(\text{P-C-N})^+$ complexes in diamond. These should be compared with the experimental [14] values for the monoclinic-I NIRIM-8 EPR centre, with $A_s = 98$ MHz, and $A_p = 85$ MHz.	116
7.3	Calculated hyperfine interactions for ^{31}P - ^{11}B complexes in diamond (MHz). For axially symmetric $(\text{P-B})^q$ centres, A_{\parallel} lies along [111]. For $(\text{P-C-B})^q$ complexes in diamond both magnitude and direction (θ, ϕ) are in terms of the inclination, θ , with respect to [001] and azimuthal angle, ϕ , measured from [100] towards [010] (degrees).	118
7.4	Calculated isotropic (A_s) and anisotropic (A_p) hyperfine interactions (MHz) of ^{31}P , the under-co-ordinated ^{13}C and ^{17}O in $(\text{P-O})^0$ and $(\text{P-C-O})^0$ complexes in diamond.	119
7.5	Hyperfine interactions (MHz) of ^{31}P and ^{13}C for the sites indicated in Fig. 7.6. The directions in parentheses are indicated in spherical-polar co-ordinates with θ measured from [001] and ϕ from [100] towards [010].	121

List of Publications

EPR centres in diamond publications, in chronological order,

1. **K. M. Etmimi**, M. A. Ahmed, P. R. Briddon, J. P. Goss, A. M. Gsiewa, Nitrogen-pair paramagnetic defects in diamond: A density functional study, *Phys. Rev. B* **79**, 20, 205207 (2009).
2. **K. M. Etmimi**, J. P. Goss, P. R. Briddon, A. M. Gsiewa, Density functional studies of muonium in nitrogen aggregate containing diamond: the Mu_X centre, *J. Phys. - Condens. Matter*, **21**, 36, 364211 (2009).
3. **K. M. Etmimi**, J. P. Goss, P. R. Briddon, A. M. Gsiewa, A density functional theory study of models for the N3 and OK1 EPR centres in diamond, *J. Phys. - Condens. Matter*, **22**, 38, 385502 (2010).
4. **K. M. Etmimi**, J. P. Goss, P. R. Briddon, Calculated hyperfine interaction parameters for P-containing point defects in diamond, submitted to *J. Phys. - Condens. Matter*.
5. **K. M. Etmimi**, J. P. Goss, P. R. Briddon, Substitutional oxygen and oxygen-vacancy complexes in diamond, in preparation.

List of Conferences,

1. Aimpro meeting 2008, 10-12 December 2008, Institute of Materials Jean Rouxel, Nantes, France.
2. Postgraduate Research Conference 2010, 13-14 January 2010, School of Electrical, Electronic & Computer Engineering, Newcastle University, Newcastle upon Tyne, UK.
3. Diamond conference 2009, 07-10 July, 2009, University of Warwick, Warwick, UK.
4. Postgraduate Research Conference 2010, 21-22 January 2010, School of Electrical, Electronic & Computer Engineering, Newcastle University, Newcastle upon Tyne, UK.
5. AIMPRO meeting 2010, 19-22 April, 2010, University of Nottingham, Nottingham, UK.
6. Diamond conference 2010, 13-16 July, 2010, University of Warwick, Warwick, UK.

CHAPTER

1

Introduction

1.1 Introduction

First principle calculations have been used to study the properties of a variety of point defects in diamond. First principle or ab initio means that no experimental data has been used as input. The only experimental input data has been used is the atomic numbers of the atoms are modelled. In this work the calculations are performed using density functional theory (DFT) implanted in AIMPRO code. AIMPRO has the ability to calculate various experimental observables such as hyperfine interactions, activation energy, vibration modes and electrical levels. This enables us to compare theoretical values against experimental ones, which can give an understanding of what is going on experimentally.

Unique properties such as high hardness, high thermal conductivity and high carrier mobility make diamond a very interesting material in terms of high power, speed, pres-

sure and temperature applications in addition to the gemstone market. This interest has increased since developments in the synthesis of diamond via high pressure, high temperature (HPHT) and chemical vapour deposition (CVD) techniques. Point defects play a major role in changing the thermal and electrical conductivities and colour properties of diamond, which could affect its performance in semiconductor applications. On the other hand point defects such as boron can be successfully grown in diamond to produce p-type semiconductors [15]. However the lack of shallow donors to produce n-type semiconductors make it difficult to produce p-n junctions to be exploited in electronic devices. Nitrogen is the most common impurity in natural and synthetic diamond, and natural diamond is classified according to nitrogen content. Nitrogen is a relatively deep donor with a level at 1.7 eV below the bottom of the conduction band [16]. With a donor level at around 0.6 eV below the conduction band [17], phosphorus is a good candidate, but ionisation fractions do not reach appropriate levels at room temperature. One promising field is the use of diamond for quantum computing by using the nitrogen-vacancy centre [18].

Hydrogen can be incorporated along with other impurities during CVD diamond growth. Hydrogen can passivate donors or acceptors, which could lead to difficulty in producing electrically active p-types. There is a little information about hydrogen defects in diamond. Mounium can be considered as an isotope of hydrogen and the moun spin relaxation (μSR) technique can help us to understand hydrogen in diamond. In order to study the properties of diamond it is crucial to understand the defects involved. One powerful technique is electron spin resonance (EPR), which has the ability to determine the chemical species that have unpaired electrons and its symmetry, which can be calculated by AIMPRO code.

1.2 Properties of Diamond

Diamond is composed of pure carbon. Carbon is the sixth element in the periodic table, which has four electrons in its valence orbital (group IV) with an electronic ground-state configuration $(1s^2)2s^22p^2$. The structure of diamond requires s and p atomic orbitals to form tetrahedral sp^3 hybridisation, and to form four-fold coordination with other C atoms.

This hybridisation appears in methane, ethane, and so on. Diamond has very strong C-C covalent bonds with relatively short bond lengths (1.54 \AA) and the C-C-C bond angles are 109.47° . Furthermore, the strong covalent bonding between carbon atoms make diamond the hardest natural material on the earth, defining 10 out of 10 on the Mohs scale developed by the mineralogist Frederich Mohs in 1812 which tests unknown minerals against one of ten standard minerals by measuring which scratches the other. The hardness value also depends on the crystal orientation, with a value of 137 GPa for the (100) face and a value of 167 GPa for the (111) face [19].

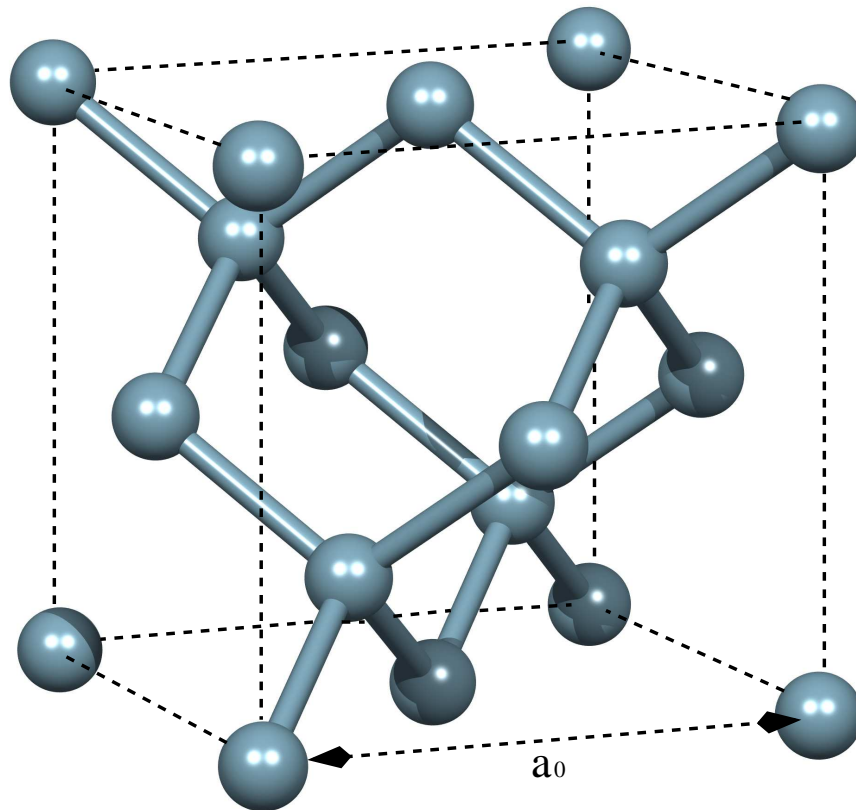


Figure 1.1: Conventional unit cell of diamond, where a_0 is the lattice constant.

Diamond has a two-atom basis at $(0\ 0\ 0)$ and $(\frac{1}{4}\ \frac{1}{4}\ \frac{1}{4})$, which can be considered as two interpenetrating face-centred cubic (fcc) lattices, where one lattice is shifted diagonally

by one-quarter of the lattice constant. The diamond structure shown in Fig. 1.1 shows a conventional unit cell which contains eight C atoms, where a_0 is the lattice constant with a value of 3.566 Å at room temperature [20], giving diamond the atomic density ($\frac{8}{a^3}$) $\approx 1.76 \times 10^{23}$ atom per cm^{-3} . The natural abundance of ^{12}C and ^{13}C are 98.9% and 1.1% respectively.

Diamond is an indirect, wide-band gap insulator with a band-gap of 5.47 eV at room temperature [20]. The top of the valence band at Γ -point and the bottom of the conduction band at $\approx \frac{3}{4}$ towards the X-point in the Brillouin zone, as indicated in Fig. 1.2(a). Diamond is often also viewed using the conventional unit cell (Fig. 1.1) which has a simple cubic structure. The Brillouin zone of a simple-cubic lattice is also simple-cubic, as shown in Fig. 1.2(b).

Diamond has several unique properties, such as its thermal conductivity. This is believed to be highest in natural diamond where thermal energy is transmitted quickly due to low atomic mass and strong covalent bonds. Conductivity in the range of 8.95 - 23 W/cm.K at 300 K [21] depends on the concentration of impurities such as nitrogen [22], and also depends strongly on temperature [23]. This value compares favourably with those of silicon at 1.48 W/cm.K and of copper at 4.01 W/cm.K (both at 300 K). Diamond has optical transparency in the near ultraviolet, visible, and infrared spectra. This remarkable property provides uses in many optical applications. The p-type semiconductor does exist naturally in diamond type IIb (see section 1.3) due to boron impurities. However this type is very rare and commercially very valuable due to its blue colour from the presence of boron. The majority of natural diamonds are brown in colour [24], however, high-pressure high-temperature (HPHT) treatment techniques can change brown diamonds [24–26] to colourless or the more valuable fancy yellow colour.

1.3 Classification of Diamond

Several impurities have been confirmed in diamond which turn its colour brown, yellow red, pink, green or blue. However the origin of the colour of diamonds is still not com-

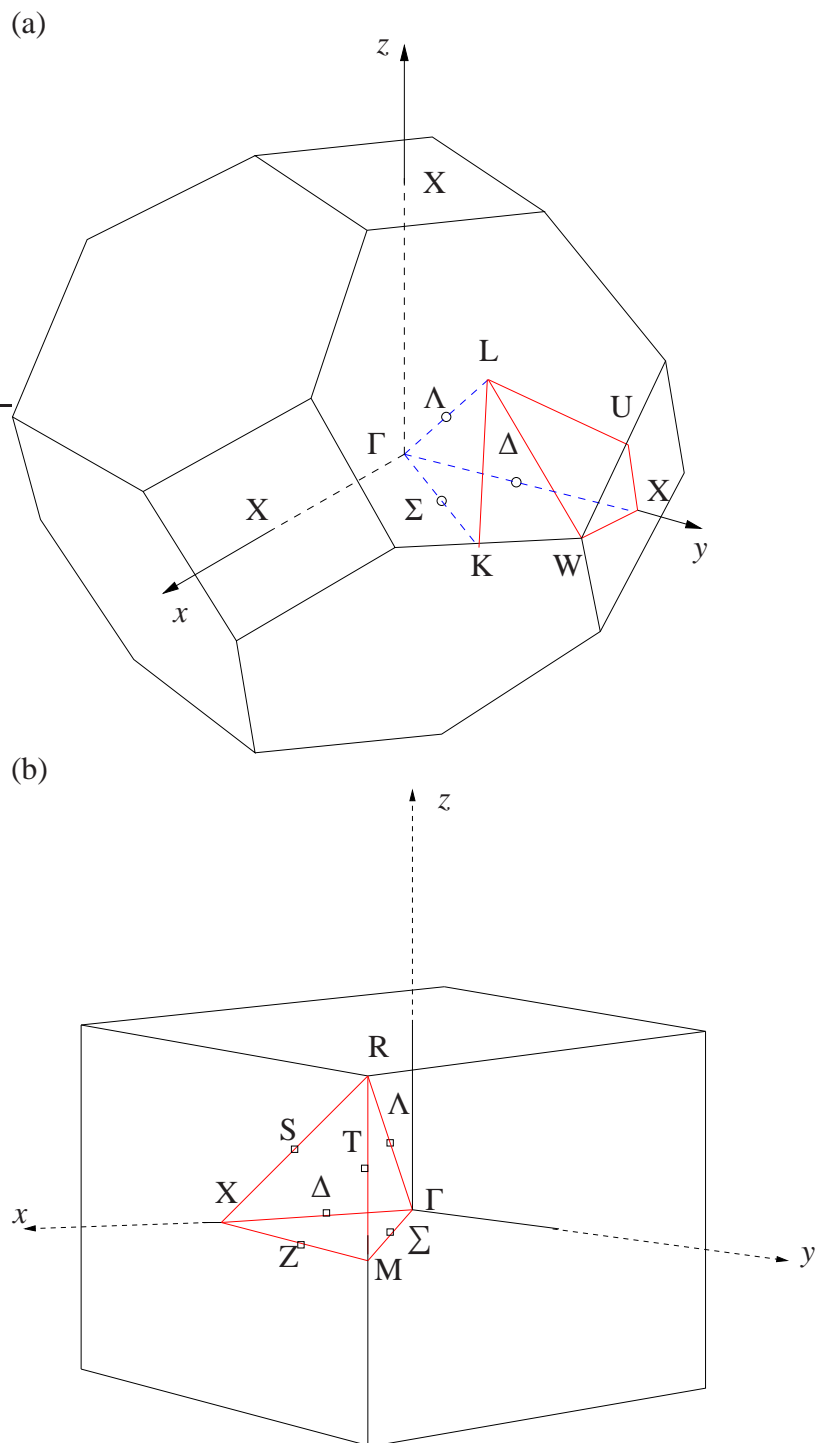


Figure 1.2: The First Brillouin zone of (a) an FCC lattice (b) an SC lattice, with high symmetry \mathbf{k} -points marked.

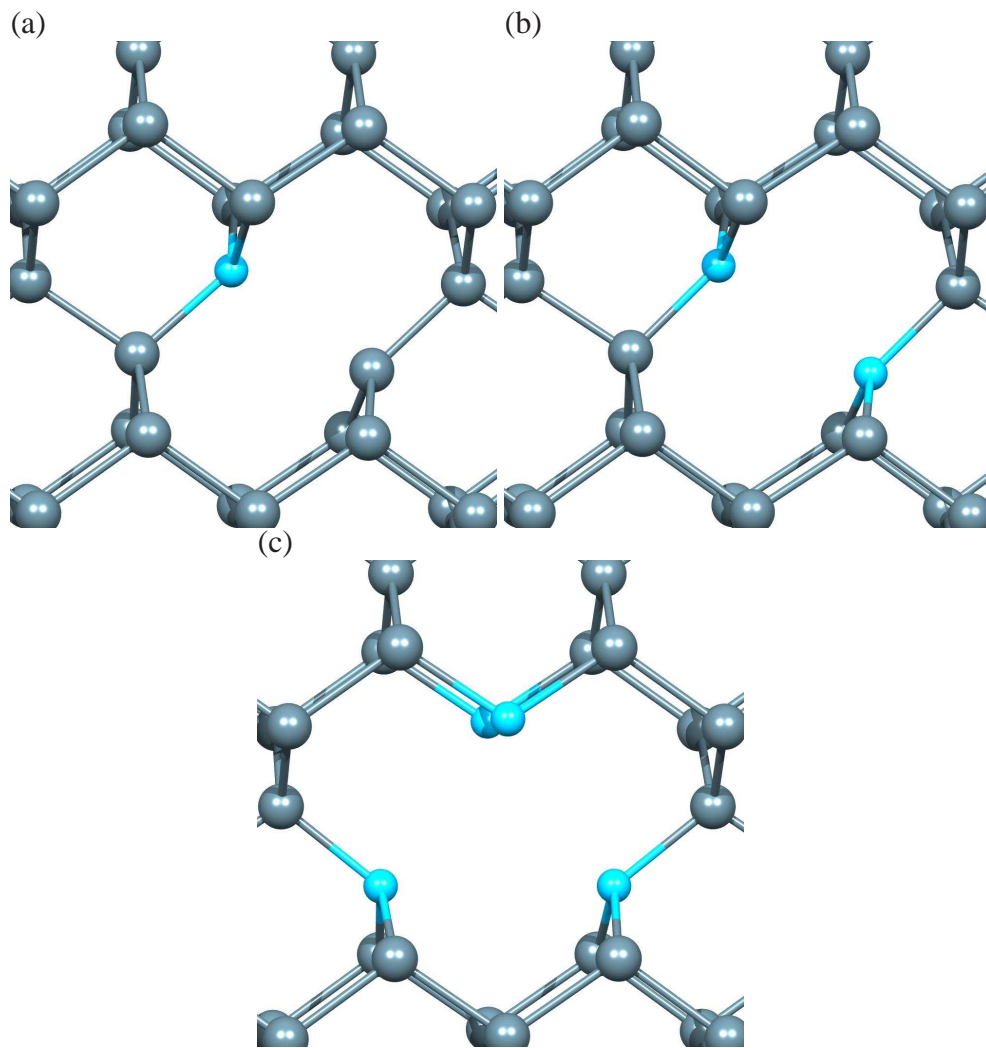


Figure 1.3: Schematics showing the calculated structures of nitrogen defects in diamond. (a) C-centre, (b) A-centre, and (c) B-centre. Blue and grey atoms are nitrogen and carbon respectively. Horizontal and vertical directions are approximately $[110]$ and $[001]$ respectively.

pletely understood. Because of the dominance of nitrogen impurities, natural diamonds are classified into two types according to nitrogen content.

1. **Type I:** contain high concentrations of nitrogen. Some diamond of type I exhibits a yellow colour, which is known to arise from nitrogen impurities [27].

- **Type Ia:** those which contain nitrogen in an aggregated form. About 98% of natural diamond is this type, again is divided to two sub-groups according to two different forms of nitrogen aggregation.
 - IaA: contains nitrogen in A-centre form (Fig. 1.3 (b)) with two nitrogen atoms the nearest neighbours.
 - IaB: contains nitrogen in B-centre form (Fig. 1.3 (c)) with four nitrogen atoms surrounding a vacancy.
 - **Type Ib:** contain nitrogen as isolated impurities which are sometimes labelled as C-centres (Fig. 1.3 (a)), where natural diamond contains less than 0.1 % of this type.
2. **Type II:** contains no nitrogen or low level (< 1-2 ppm [28]) which is undetectable by infrared or ultraviolet absorption measurements.
- **Type IIa:** rare in natural diamond and usually colourless.
 - **Type IIb:** also very rare in nature, containing boron impurities. Due to the absence of donors such as nitrogen, the boron can produce a p-type conductor. Boron is known to be responsible for a blue colouration [29].

1.4 Defects in Diamond

Diamond contains both point and extended defects. Point defects are the result of a few atoms or vacancies which are in irregular arrangements in the structure of the lattice, and extended defects involve more atoms or vacancies which may be arranged in one or more directions, such as platelets, inclusions, twins, stacking faults and dislocations.

1. **Point defects:** Point defects could be intrinsic (self-interstitial defects or vacancies) atoms, interstitial foreign impurity atoms or substitutional foreign atoms. Nitrogen and boron in addition to the ubiquitous impurity of hydrogen are the most common point defects in diamond because of their relatively similar size compared to carbon.

Electron paramagnetic resonance (EPR) is one of the most significant spectroscopy techniques which can detect an enormous number of point defects in diamond. Nitrogen and nitrogen-related defects in addition to muonium are studied in detail in subsequent sections in relation to hyperfine interaction techniques.

2. **Extended defects:** these are defects extended in one, two or three dimensions. They can be considered as a line defect like dislocations, a plane defect like stacking faults and platelets, or a volume defect like clusters of vacancies or any different volume in the structure. Extended defects are created by both intrinsic or extrinsic impurities.

1.5 Diamond Synthesis

Because of its unique properties and commercial value as gem stones, attempts to synthesise diamond started as early as the 1800s, when it was discovered that diamond forms from carbon. The first known successful attempt was in 1955 when diamond was grown using a high pressure high temperature technique [30]. Two methods of growing diamond are summarised below.

1.5.1 High pressure high temperature (HPHT)

The first attempts to grow diamond in the 1950s were by General Electric, using the HPHT technique which recreates the conditions that produce natural diamond in the earth of depths of approximately 200 km. This process needs about 5 Gpa of pressure and thousands of degrees Celsius (typically 5 Gpa and 2000 °C) to convert graphite to diamond. In addition to the appropriate pressure and temperature, a solvent catalyst was found to be essential to complete the conversion. Different sizes and qualities of diamond can be synthesised depending on pressure and temperature conditions and upon time, since diamonds take millions of years to form naturally underground. Fig. 1.4 shows a schematic design for the production of HPHT synthetic diamonds.

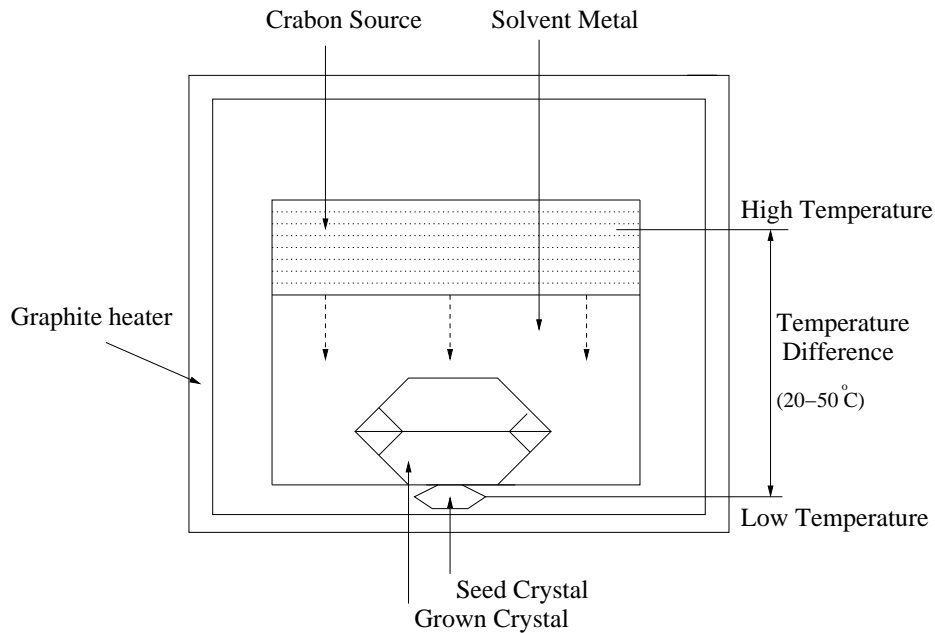


Figure 1.4: Schematic setup of a system for the production of HPHT synthetic diamonds.

1.5.2 Chemical vapour deposition (CVD)

CVD [31] is a very common method for growing diamond films where, in contrast to HPHT, a temperature between 800-1000 °C and approximately atmospheric pressure are needed. CVD has recently gained prominence because a technique to grow relatively high areas of high quality single crystals has been achieved which can be exploited in diamond technology. H_2 is usually used as an etchant to prevent the formation of sp^2 -bonds and the gas always contains sources of carbon such as methane CH_4 compounds (with a typical ratio of 1% in H_2 gas). This is dissociated at low temperatures and pressures to decompose the carbon atoms onto an appropriate substrate heated to between 800-1000 °C to form diamond type Ib, which contains a single nitrogen as result of the presence of nitrogen in the gas. Usually, due to the inappropriate temperature and pressure, aggregations of nitrogen do not occur in CVD diamond.

A microwave beam is often used to create plasma in order to obtain the right conditions for the decomposition, and the ionisation can also be achieved thermally using a hot

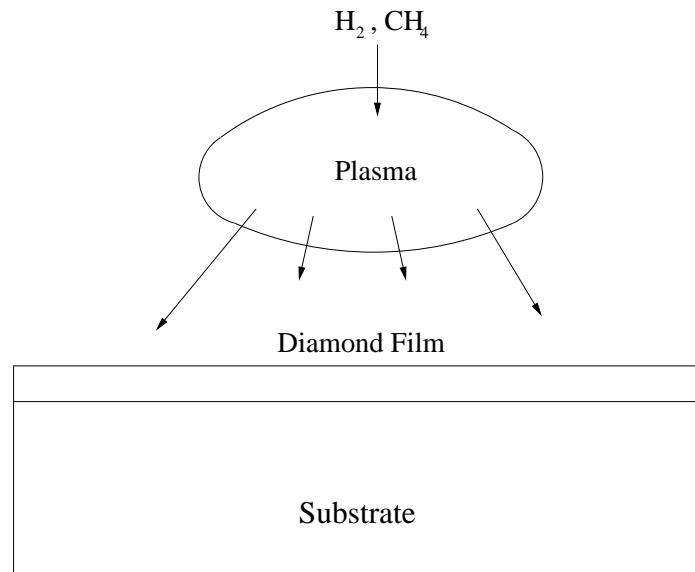


Figure 1.5: Schematic setup of a system for the production of CVD synthetic diamond. (hot filament for example can be used instead of plasma for ionisation)

filament. The growth rate varies depending on area. For an area less than 1 cm^2 growth is about 1 mm/h , however the quality of film increases with decreasing growth rate. Furthermore the type of substrate determines whether single- or poly-crystal can occur. Single crystal diamond is obtained when the substrate is made from single crystals of diamond, and polycrystalline diamond is obtained when the substrate is made of silicon, tungsten or molybdenum. Fig. 1.5 shows a design for the production of CVD synthetic diamond.

1.5.3 Applications of Diamond

In addition to commercial purposes as gemstones, diamond is used in industrial applications as an abrasive, in sawing, grinding and cutting tools, as a result of its hardness and wear resistance. Recently, due to its low thermal expansion coefficient and thermal conductivity, diamond has been used in heat dissipation devices [32]. CVD techniques give the ability to deposit diamond on substrates such as glass, water filters and cutting tools to produce a protective coating. Diamond can also be used in radiation detectors and X-ray dosimeters [33].

Diamond is currently also being exploited in optical and electronic applications, because

it is optically transparent over a large wavelength range due to a large band gap (~ 5.5 eV). Its hardness has also been used for radiation windows where high energy and extreme mechanical and thermal loads are operated [34]. Also quite recently, diamond has been used for so-called quantum information [35] by performing spin operations from point defects in diamond such as nitrogen-vacancy complexes.

1.6 Thesis Summary

The thesis is divided into three parts. Each part is subdivided into chapters.

1.6.1 Part I: Theoretical Framework

Chapter 2 - Background theory and AIMPRO modelling package

This chapter explains the background theory that has been used to solve the many-body Schrödinger equation, starting with the Born-Oppenheimer approximation, and presents a review of approximations using the wave function-based approach to solve the problem. Then the discussion proceeds to the ab initio method density functional theory, which made noticeable advances in terms of calculation accuracy. The exchange-correlation term approaches, such as the generalised gradient approximation, are also discussed, followed by pseudopotential approximation which replaces the motion of the core electrons of an atom and its nucleus. Finally electron paramagnetic resonance and hyperfine interaction are defined.

An extended discussion is then given of the implementation of quantum mechanical density functional theory (DFT) using the ab initio modelling programme called AIMPRO. This includes the supercell approach, Brillouin zone sampling, basis set, self-consistency, and vibration modes.

Chapter 3 - Modelling of experimental observables

This chapter links density functional theory with experimental techniques. This enables us to compare the calculated and experimental values of the physical properties of the material.

1.6.2 Part II: Applications

Chapter 4 - Nitrogen-pair paramagnetic defects

Electron-paramagnetic-resonance centres of nitrogen pairs separated by different numbers of intervening host sites, both in ionised, $S = 1/2$, and neutral $S = 1$ forms are reviewed using density functional techniques. The hyperfine interaction are discussed in details, an additional to the activation energies in this chapter.

Chapter 5 - Muonium and hydrogen in nitrogen-aggregate containing diamond: the μ_X centre

Hydrogen is involved in electrically active defects in CVD diamond, and muonium, via μ SR, can provide useful characterisations of the configurations adopted by H atoms in a crystalline material. This chapter presents the results of a computational investigation into the structure of the μ_X centre proposed to be associated with nitrogen aggregates. It is found that the propensity of hydrogen or muonium to chemically react with the lattice makes the correlation of μ_X with nitrogen aggregates problematic, and suggest alternative structures.

Chapter 6 - Nitrogen-oxygen pairs in diamond: the N3 and OK1 EPR centres

This chapter presents the results of density functional simulations of N-O pairs in diamond, reviewing them in the light of the experimental evidence. Also presents the analysis of other structures proposed for the EPR spectra, based upon nitrogen-multi-vacancy centres and nitrogen decorating titanium-vacancy complexes, and show that none of the current models are entirely plausible.

Chapter 7 - Calculated hyperfine interaction parameters for P-containing point defects in diamond

This study presents the results of density functional simulations of P-containing point defects, focusing on the hyperfine interactions of unpaired electrons with the $I = 1/2$ nucleus of ^{31}P . It is shown that the calculated magnitudes for distorted P are consistent with experimental values, and present predictions for complexes of P with itself, lattice vacancies, nitrogen, hydrogen, boron and oxygen.

1.6.3 Part III: Conclusions**Chapter 8 - Summary**

This chapter summarises the work presented in the thesis.

1.7 Abbreviations and Acronyms

The following abbreviations and acronyms are used within this thesis.

AIMPRO	<i>Ab Initio</i> Modelling PROgram.
CVD	Chemical Vapour Deposition.
DFT	Density Functional Theory.
EPR	Electron Paramagnetic Resonance.
GGA	Generalised Gradient Approximation.
HFI	Hyperfine Interaction
HGH	Hartwigsen-Göedecker-Hutter.
HK	Hohenberg-Kohn.
HPHT	High Pressure High Temperature.
KS	Kohn-Sham.
LDA	Local Density Approximation.
MP	Monkhorst-Pack.
μ SR	Muon Spin Relaxation.
NEB	Nudged Elastic Band.

Part I

Theoretical Framework

CHAPTER

2

Background Theory and AIMPRO Modelling Package

2.1 Introduction

This chapter gives a brief discussion of the theory applied in this work, then outlines the important elements of the computer code used in this thesis. This code is called AIMPRO [36–38] (Ab Initio Modelling Program), which enables us to apply the DFT theory to problems in diamond.

2.2 The Many Body Problem

The many body Schrödinger equation for a system of interacting electrons and nuclei is given as:

$$\hat{H} = \hat{T}_e + \hat{T}_n + \hat{V}_e + \hat{V}_n + \hat{V}_{en} \quad (2.1)$$

where \hat{T}_e , \hat{T}_n correspond to the kinetic energy of the electrons and nuclei respectively. \hat{V}_e , \hat{V}_n and \hat{V}_{en} are electron-electron, nuclear-nuclear and electron-nuclear interaction potentials respectively. Using atomic units, i.e. $\hbar = e = m_e = 4\pi\epsilon_0 = 1$, the Hamiltonian will be:

$$\hat{H} = -\frac{1}{2} \sum_{i=1}^N \nabla_i^2 - \frac{1}{2} \sum_k \frac{1}{M_k} \nabla_k^2 + \frac{1}{2} \sum_{i \neq j} \frac{1}{|\mathbf{r}_i - \mathbf{r}_j|} + \frac{1}{2} \sum_{k \neq l} \frac{Z_k Z_l}{|\mathbf{R}_k - \mathbf{R}_l|} - \sum_{i,k} \frac{Z_k}{|\mathbf{r}_i - \mathbf{R}_k|} \quad (2.2)$$

where \mathbf{r} and \mathbf{R} are the positions of electrons and nuclei respectively, M_k are the nuclear masses, and Z_l is the charge of the l -th nucleus. The equation $\hat{H}\Psi = E\Psi$ is complicated and cannot be solved directly in such a form; however several approximations can be used to obtain a solution.

2.3 Born-Oppenheimer Approximation

This approximation [39], which is also known as the adiabatic approximation, essentially depends upon assuming that due to the large mass of nuclei compared to the mass of electrons, the motion of electrons is much faster than that of nuclei. So the electron movement can be considered in a fixed field of nuclei. This simplifies the equation 2.2 to the electron Hamiltonian:

$$\hat{H} = -\frac{1}{2} \sum_{i=1}^N \nabla_i^2 + \frac{1}{2} \sum_{i \neq j} \frac{1}{|\mathbf{r}_i - \mathbf{r}_j|} - \sum_{i,k} \frac{Z_k}{|\mathbf{r}_i - \mathbf{R}_k|} \quad (2.3)$$

2.4 The Hartree Approximation

The Hartree approximation [40] considers the many electron wave function Ψ as a product of single electron wave function by neglecting the antisymmetric requirement; and therefore:

$$\Psi(\mathbf{r}_1, \mathbf{r}_2, \dots, \mathbf{r}_N) = \prod_{i=1}^N \psi_i(\mathbf{r}_i) \quad (2.4)$$

where $\psi_i(\mathbf{r}_i)$ are normalised and satisfy one-electron equations

$$-\frac{1}{2}\nabla^2\psi_i + V_i\psi_i = E_i\psi_i \quad (2.5)$$

where the potential will be:

$$V_i(\mathbf{r}) = \sum_k -\frac{Z_k}{|\mathbf{r}_k - \mathbf{r}|} + \sum_{j \neq i} \int \frac{|\psi_j(\mathbf{r}')|^2}{|\mathbf{r} - \mathbf{r}'|} d\mathbf{r}' \quad (2.6)$$

This simple approximation is not accurate enough for most modern calculations, hence a better approximation is needed.

2.5 The Hartree-Fock Approximation

The main problem with the Hartree wave function is that it is not antisymmetric. This can be rectified by writing:

$$\Psi(\mathbf{r}_1, \mathbf{r}_2, \dots, \mathbf{r}_N) = \frac{1}{\sqrt{N!}} (-1)^P \hat{P}(\psi_1(\mathbf{r}_1)\psi_2(\mathbf{r}_2)\dots\psi_N(\mathbf{r}_N)) \quad (2.7)$$

where N is the number of electrons and P is the permutation operator that interchanges the electron labels.

This may be expressed as the Slater determinant:

$$\Psi(r_i) = \frac{1}{\sqrt{N!}} \begin{vmatrix} \psi_1(\mathbf{r}_1) & \psi_1(\mathbf{r}_2) & \cdots & \psi_1(\mathbf{r}_N) \\ \psi_2(\mathbf{r}_1) & \psi_2(\mathbf{r}_2) & \cdots & \psi_2(\mathbf{r}_N) \\ \vdots & \vdots & \ddots & \vdots \\ \psi_N(\mathbf{r}_1) & \psi_N(\mathbf{r}_2) & \cdots & \psi_N(\mathbf{r}_N) \end{vmatrix} \quad (2.8)$$

Exchanging any two electrons changes the sign of the determinant, and if two electrons have identical spin and position, the determinant will be zero. This ensures that Ψ is antisymmetric and obeys the Pauli exclusion principle. The Hartree-Fock method [41] has been used in quantum chemistry and gives reasonable results for atoms and many molecules.

However, in solids these calculations are relatively complicated and do not include correlation energy, which represents Coulomb repulsion due to the motion of the individual electrons.

2.6 Density Functional Theory

Density functional theory (DFT) makes use of the one-to-one relation between a non-degenerate ground state wave function and electron density. This concept was initially applied by Thomas and Fermi in 1927 [42, 43] and later proved by Hohenberg and Kohn [44] and Kohn and Sham [45] respectively.

2.6.1 Hohenberg-Kohn theorems

The non-degenerate ground state wave function of a many-electron system in an external potential \hat{V} can be uniquely determined by its electron charge density, which means one can use the electron density as a basic variable instead of the many-electron wave functions. To see this, start by considering the Hamiltonian for two systems:

$$\hat{H}_1 = \hat{T} + \hat{U} + \hat{V}_1 \quad (2.9)$$

$$\hat{H}_2 = \hat{T} + \hat{U} + \hat{V}_2 \quad (2.10)$$

where \hat{T} and \hat{U} are the kinetic and electron interaction energy operators, and \hat{V} is the external potential. Now, assume that there are two different potentials, \hat{V}_1 and \hat{V}_2 , which give rise to two ground state wave functions ψ_1 and ψ_2 respectively where both have the same charge density $n(\mathbf{r})$. It is quite clear that these two ground states wave functions are not equal ($\psi_1 \neq \psi_2$). The energy of the first and second systems are:

$$E_1 = \langle \psi_1 | H_1 | \psi_1 \rangle, E_2 = \langle \psi_2 | H_2 | \psi_2 \rangle. \quad (2.11)$$

By applying the variational principle one obtains two inequalities

$$E_1 < \langle \psi_2 | H_1 | \psi_2 \rangle \quad (2.12)$$

and

$$E_2 < \langle \psi_1 | H_2 | \psi_1 \rangle \quad (2.13)$$

These two inequalities can be written in term of external potentials.

$$E_1 < \langle \psi_2 | H_1 | \psi_2 \rangle = \langle \psi_2 | T + U + V_1 | \psi_2 \rangle \quad (2.14)$$

$$= \langle \psi_2 | T + U + V_2 | \psi_2 \rangle + \langle \psi_2 | V_1 - V_2 | \psi_2 \rangle \quad (2.15)$$

Now, $E_2 = \langle \psi_2 | H_2 | \psi_2 \rangle$, so we have,

$$E_1 < E_2 + \langle \psi_2 | V_1 - V_2 | \psi_2 \rangle \quad (2.16)$$

Similarly,

$$E_2 < E_1 + \langle \psi_1 | V_2 - V_1 | \psi_1 \rangle \quad (2.17)$$

Then by using a universal functional $F[n]$ introduced by HK:

$$E[n(r)] = F[n(\mathbf{r})] + \int V(\mathbf{r})n(\mathbf{r})d\mathbf{r} \quad (2.18)$$

The Eq. 2.16 will be:

$$E_1 < E_2 + \int (V_1 - V_2)n(\mathbf{r})d\mathbf{r} \quad (2.19)$$

Similarly,

$$E_2 < E_1 + \int (V_2 - V_1)n(\mathbf{r})d\mathbf{r} \quad (2.20)$$

By adding together these inequalities, we get an impossible result.

$$E_1 + E_2 < E_2 + E_1 \quad (2.21)$$

So the assumption that $n(\mathbf{r}) = n'(\mathbf{r})$ must be wrong, and hence V_1 is a unique function of the density $n(\mathbf{r})$ and therefore the Hamiltonian can be established by the density.

Hohenberg and Kohn [45] wrote the total energy as:

$$E = \int V(\mathbf{r})n(\mathbf{r})d\mathbf{r} + \frac{1}{2} \int \frac{n(\mathbf{r}_1)n(\mathbf{r}_2)}{|\mathbf{r}_1 - \mathbf{r}_2|} d\mathbf{r}_1 d\mathbf{r}_2 + G[n] \quad (2.22)$$

where the second term is called the Hartree energy and $G[n]$ contains all electron-electron effects beyond this. However Hohenberg and Kohn failed to give a sufficiently accurate formula for $G[n]$.

2.6.2 The Kohn-Sham approach

The Kohn-Sham theorem [46] suggests that $G[n]$ is separated into two parts:

$$G[n] = T_s[n] + E_{xc}[n] \quad (2.23)$$

where $T_s[n]$ is the kinetic energy of a non-interacting system of electrons which has the same density as the real system and $E_{xc}[n]$ is the exchange and correlation energy. $T_s[n]$ can be treated in the same way as the Hartree-Fock wave functions. For a non-interacting system of N electrons,

$$n(\mathbf{r}) = \sum_{i=1}^N |\psi_i(\mathbf{r})|^2 \quad (2.24)$$

where the ψ_i are called the Kohn-Sham wave function. The kinetic energy function can be therefore written as

$$T_s[n] = -\frac{1}{2} \sum_{i=1}^N \int \psi_i(\mathbf{r}) \nabla^2 \psi_i(\mathbf{r}) d\mathbf{r} \quad (2.25)$$

Then the Kohn-Sham wave functions are constrained to be normalised:

$$\int |\psi_i(\mathbf{r})|^2 d\mathbf{r} = 1 \quad (2.26)$$

By using Lagrange multipliers ϵ_i and following the variational principle:

$$\frac{\partial}{\partial \psi_i^*(\mathbf{r})} \left[E - \sum_i \epsilon_i \int |\psi_i(\mathbf{r})|^2 \right] = 0 \quad (2.27)$$

This leads to the Kohn-Sham equation

$$-\frac{1}{2} \nabla^2 \psi_i(\mathbf{r}) + V_{\text{eff}}(\mathbf{r}) \psi_i(\mathbf{r}) = \epsilon_i \psi_i(\mathbf{r}) \quad (2.28)$$

where $V_{\text{eff}}(\mathbf{r})$ is an effective potential that can be written as

$$V_{\text{eff}}(\mathbf{r}) = V(\mathbf{r}) + \int \frac{n(\mathbf{r}')}{|\mathbf{r} - \mathbf{r}'|} d\mathbf{r}' + \frac{\partial E_{xc}[n]}{\partial n(\mathbf{r})} \quad (2.29)$$

2.6.3 The exchange-correlation functional

Several approximations have been made to avoid the problem of the unknown exchange-correlation energy E_{xc} . The most common are the local density (LDA) and generalised gradient (GGA) approximations.

Local Density Approximation (LDA)

One of the most common approximations is the local density approximation (LDA) [45, 47, 48] in which E_{xc} can be obtained by using the homogeneous electron gas formula.

The exchange-correlation energy is assumed to be local, and can be separated into exchange and correlation parts:

$$E_{xc}[n_{\uparrow}, n_{\downarrow}] = E_x[n_{\uparrow}, n_{\downarrow}] + E_c[n_{\uparrow}, n_{\downarrow}] \quad (2.30)$$

In a homogeneous gas the exchange function can be written in form [47]:

$$E_x[n_{\uparrow}, n_{\downarrow}] = -\frac{3}{2} \left(\frac{3}{4\pi} \right)^{\frac{1}{3}} \left(n_{\uparrow}^{\frac{4}{3}} + n_{\downarrow}^{\frac{4}{3}} \right) (\text{volume}) \quad (2.31)$$

For an inhomogeneous system we form the LDA as

$$E_x[n_{\uparrow}, n_{\downarrow}] = -\frac{3}{2} \left(\frac{3}{4\pi} \right)^{\frac{1}{3}} \int \left(n_{\uparrow}^{\frac{4}{3}}(\mathbf{r}) + n_{\downarrow}^{\frac{4}{3}}(\mathbf{r}) \right) d\mathbf{r} \quad (2.32)$$

The correlation term is more complicated, but a formula has been developed [48]. The local density approximation would give good results in areas where density varies slowly. Even in areas where density changes very quickly, the local density approximation may give reasonable results. However it tends to underestimate, for examples ionisation energies and band gap while overestimating binding energies.

Generalised Gradient Approximation (GGA)

In order to move beyond LDA [45, 47, 48], an approximation for estimating the exchange-correlation energy is the generalised gradient approximation (GGA). This considers a first order expansion of E_{xc} in the charge density, and includes terms depending on $|\nabla n|$ [49, 50].

The GGA has achieved greater accuracy compared to LDA, and generally produces better total energies, binding energies, bond lengths and angles. Both of the latter are underestimated in the band gap. In the case of inhomogeneous electron gas, an improvement was made by adding a factor to the E_{xc} functional in local density approximation (LDA). This factor includes derivatives of the charge density (gradient of electron density) at a certain point in addition to the normal function of density at the same point represented by LDA. With this factor, the GGA is thus:

$$E_{xc}[n(\mathbf{r})] = \int n(\mathbf{r})\epsilon_{xc}F_{xc}[n(\mathbf{r}), \nabla n(\mathbf{r}), \nabla^2 n(\mathbf{r}), \dots]d\mathbf{r} \quad (2.33)$$

2.7 Pseudopotentials

Applying density functional theory to systems with a large number of electrons still leaves a demanding calculation. In solid-state physics and the physics of atoms and molecules, the properties of electrons and the chemical bonds between atoms are almost entirely determined by the valence electrons of the atoms, where core electrons create a screening potential or *pseudopotential* acting upon the valence electrons. To achieve this simplicity we replace the Coulomb attraction of the nuclei by a pseudopotential which is felt by valence electrons and describes the interaction with the core electrons and nucleus (see Figure 2.1). The presence of the core states would make the total energy much larger, giving rise to a need for greater accuracy in energy calculations. Furthermore, the core electrons are very localised and force valence states to oscillate rapidly near the nucleus. This requires a large number of basis functions (see section 2.10) to describe the system.

In order to calculate certain interactions, such as hyperfine interaction, the core electron wave functions need to be reconstructed [51, 52]. Throughout this project the Hartwigsen, Goedecker and Hutter (HGH) pseudopotentials [53] were implemented in AIMPRO.

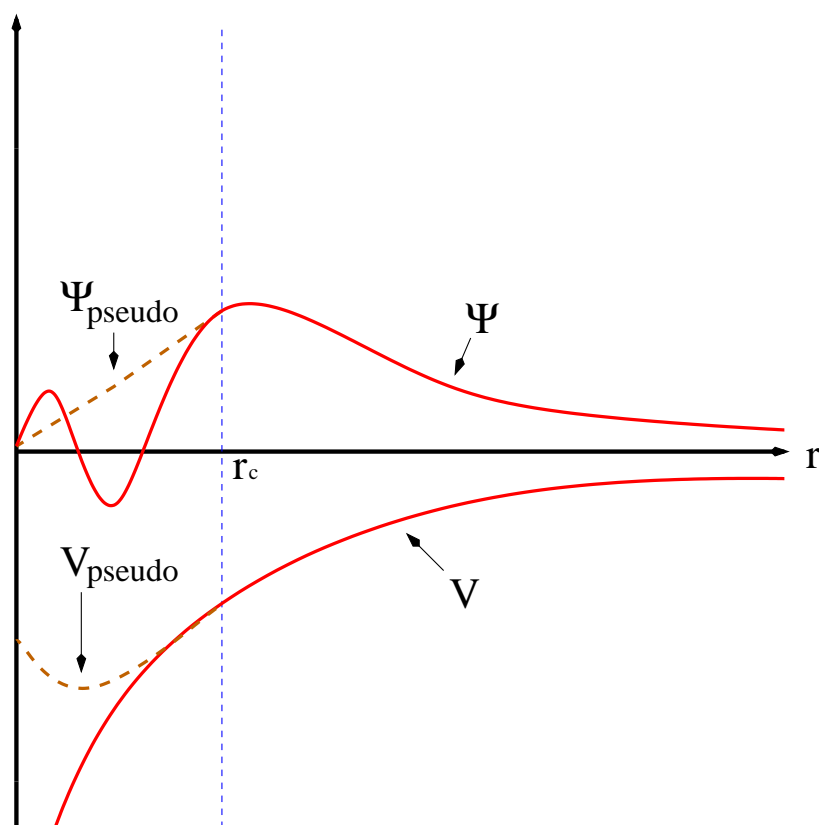


Figure 2.1: Schematic illustrating the pseudo-wave function (top) and the pseudo-potential (bottom) core electrons. The cut-off radius r_c indicates the defined region at which point the systems must match. The pseudo-wave function and potential are plotted with a brown line whilst the true all-electron wave function and core potential are plotted with the red lines.

2.8 Supercell Approach

Periodic boundary conditions have been used in this method. All systems are modelled using a unit cell which has infinite repetition in all directions. The boundary conditions applied satisfy Bloch's theorem. The supercell method overcomes the problem of defect-surface interaction which would occur if a finite cluster was used to model a defect in a solid. The cell size is crucial in the supercell method, since the defect may interact with its images in other unit cells if the number of atoms is not large enough to give sufficient

separation between defect and repeated image.

2.9 Brillouin Zone Sampling

The calculation of quantities such as total energy or charge density within the supercell framework requires an integration or averaging over the Brillouin zone. For example, a charge density may be determined at a certain value of \mathbf{k} :

$$n_k(\mathbf{r}) = \sum_n f_{nk} |\psi_{nk}|^2 \quad (2.34)$$

where f_{nk} is the occupancy of the band at wave vector \mathbf{k} . The total charge density is then given by the integral:

$$n(\mathbf{r}) = \frac{\Omega}{(2\pi)^3} \int n_k(\mathbf{r}) d^3k \quad (2.35)$$

where the integral is over the 1st BZ.

In practice, the integral is approximated as

$$n(\mathbf{r}) = \sum_{i=1}^N w_i n_{k_i}(\mathbf{r}) \quad (2.36)$$

where the points k_i can be chosen according to a number of schemes [54, 55] and w_i is the weighting factor which corresponds to the number of equivalent \mathbf{k} -points to \mathbf{k} -points i .

To solve Kohn-Sham equations, a number of \mathbf{k} -points are chosen in the Brillouin zone. By averaging over them allows the density at each point to be obtained. However convergence is not easily verified by increasing the number of \mathbf{k} -points.

Another scheme suggested by Monkhorst and Pack [56] uses a set of special \mathbf{k} -points defined by three integers I , J , and K . The integers I , J , and K define a grid of $I \times J \times K$ points in reciprocal space:

$$K(i, j, k) = \frac{2i - I - 1}{2I} \mathbf{g}_1 + \frac{2j - J - 1}{2J} \mathbf{g}_2 + \frac{2k - K - 1}{2K} \mathbf{g}_3 \quad (2.37)$$

where \mathbf{g}_1 , \mathbf{g}_2 and \mathbf{g}_3 are the unit-vectors of reciprocal space and I , J , and $K \geq 1$. When $I=J=K$ the scheme is referred to as $MP - I^3$.

2.10 Basis Sets

Cartesian Gaussian type orbitals are used in AIMPRO as a basis upon which expand the Kohn-Sham orbitals. Each Cartesian Gaussian orbital is centred at an atomic site R_i and is given by the form:

$$\phi_i(r) = (x - R_{i,x})^{n_1} (y - R_{i,y})^{n_2} (z - R_{i,z})^{n_3} e^{-\beta(r-R_i)^2} \quad (2.38)$$

where $n_\alpha \geq 0$, s , p or d -like orbitals correspond to $\sum n_\alpha = 0, 1$ or 2 respectively, and β is a constant for each function. There are a number of advantages over other basis functions in that they are localised and can decay rapidly away from the centre of the atom. In addition, integrals involving them can be found analytically. Another advantage is that the product of two Gaussian orbitals is a Gaussian function, which means that the integrals can be evaluated much more quickly.

2.11 Self-Consistency Approach

As described in section 2.6.1, the Kohn-Sham equations must be solved for self-consistency. Self-consistency is the process by which charge is redistributed around the system until a minimum energy is obtained, as a result producing an accurate simulation of the charge distribution in a real system. The first guess of the charge density coefficients is taken from the neutral atoms, then the charge density is taken from the result of the previous calculation during structural optimisation. For a better guess, the new charge density is taken by linearly combining the previous input and output charge density. So, once a potential V is generated from the input density $\mathbf{n}(\mathbf{r})$, it is used to solve KS equations (Eqs. 2.24 and 2.28), which give rise to a new output density $\mathbf{n}'(\mathbf{r})$. This process continues until the charge density and the total energy between the two sets converge, so that the difference of total energies in the self-consistency process should be smaller than a certain value (generally is $10^{-4} a.u.$).

2.12 Structural Optimisation

To determine the minimum energy configuration of the atoms, or, in other words, to optimise the structure geometrically, the forces on each atom must be determined. These can be calculated once the self-consistency charge density is obtained, as described in the previous section. Once the forces are determined, in order to obtain the minimum total energy, the atoms are moved along the force direction. This can be achieved by several techniques. Within AIMPRO the conjugate gradient method [57, 58] is applied. This method depends on determining the direction from the force components of the previous and current iterations. It cannot be guaranteed that the minimum energy obtained by this method will be the global minimum, but could be local. To try avoid such that as much as possible, one should starting with several randomised configuration.

CHAPTER

3

Modelling of Experimental Observables

3.1 Introduction

Density functional theory has the ability to calculate a large number of experimental observables. Modelling techniques can help to explain experimental results, and this is very important in making comparisons between measured and calculated values.

In this chapter, a brief explanation is given of how some of the experimental techniques relevant to the work presented in this thesis were modelled. These include the diffusion method, vibrational modes, electrical levels and electron paramagnetic resonance.

3.2 Diffusion Method in AIMPRO

AIMPRO employs several methods to determine the activation energy for the diffusion or reorientation of a defect. The nudged elastic band (NEB) [59, 60] is used in this work. This finds the saddle point and the minimum energy path between initial and final structures (which must be known). The method works by optimising a set of images along the path between known initial and final points. Each image is connected to the previous and next images and corresponds to specific positions of the atoms along the path. The constrained optimisation on each image is formulated by adding the spring forces along the direction of the band between images and then minimising the forces acting on the system. A modification of the NEB method is used to allow the highest energy image to climb towards the saddle point. Only the highest image is relaxed with the climbing constraint. If the maximum energy image is very far from the saddle point, different spacings on either side of the saddle point will be created.

Throughout this thesis a minimum of five images is used, and optimise the barrier so that image-forces are less than 0.01 atomic unit and the saddle-point energy changes by less than 1 meV. Due to the computational cost, the barriers are obtained using cubic unit cells of side length $2a_0$, unless specified otherwise. In specific cases the examination of the effect of cell size on barrier height was done and yielded satisfaction that the smaller cell yields values within 10's of meV of the larger.

3.3 Vibrational Modes

A local vibration mode is a defect vibration in which only a small number of nearby atoms move significantly that is, it is localised at the defect. AIMPRO provides a calculation of vibrational modes which can be compared with that are measured experimentally by using infra-red absorption spectroscopy or Raman scattering techniques. This method enables us to detect whether a defect is infrared or Raman active due to atomic vibrations, where the former is active if it yields a change in the dipole of the bond while the latter is active if it yields a change in polarisability.

To obtain a vibration mode, force constants are required. These are derived from second derivatives of energy with respect to position. Starting from a self-consistent converged system, an atom a is shifted from its equilibrium position along the l direction ($l = x, y$ or z) by an amount ε . The self-consistent density is recalculated at this new position. Atom b will then feel the force $f_{mb}^+(l, a)$ along the m direction. Then atom a is moved by $-\varepsilon$ giving rise to a new force on atom a of $f_{mb}^-(l, a)$. From this process, the second derivative can be calculated by:

$$\Phi_{la,mb} = \frac{f_{mb}^+(l, a) - f_{mb}^-(l, a)}{2\varepsilon} \quad (3.1)$$

The dynamical matrix is then found as

$$\mathbf{D}_{la,mb} = \frac{\Phi_{la,mb}}{\sqrt{M_a M_b}} \quad (3.2)$$

where M_a and M_b are the masses of atoms a and b . Eigenvalues of this matrix give the vibrational frequencies squares:

$$\mathbf{D} \cdot \mathbf{U} = \omega^2 \mathbf{U} \quad (3.3)$$

where \mathbf{D} is dynamic matrix, \mathbf{U} contains the normal modes and ω are the frequencies.

In chapter 6 the Vineyard [61] method is used to calculate the attempt frequency in an Arrhenius law with a diffusion barrier E^a .

$$\nu = \nu_0 \exp(-E^a/k_B T) \quad (3.4)$$

where T is temperature, and ν_0 attempt frequency. This method depends on the many-body normal mode approach. The attempt frequency can be calculated by taking the ratio of the product of the N normal frequencies of the entire crystal at the starting point to the product of $N - 1$ normal frequencies of the crystal when it is constrained to be at a saddle point.

$$\nu_0 = \prod_{p=1}^N \nu_p^e / \prod_{p=1}^{N-1} \nu_p^s \quad (3.5)$$

where ν_p^e and ν_p^s are frequencies for the equilibrium and saddle point configurations, respectively.

3.4 Electrical Levels

One characteristic of impurities in semiconductors is that they often introduce levels in the band gap. The electrical level of a defect corresponds to the electron chemical potential position when two charge states of the defect have the same energy. The donor and the acceptor levels are labelled $(0/+)$ and $(-/0)$, respectively. Two methods have been used to evaluate the electrical levels of a defect throughout this thesis.

3.4.1 Marker method

This method is empirical and uses a well known defect level as a reference to estimate the energy level of the system under study, simply by calculating the difference in donor $(0/+)$ or acceptor $(-/0)$ of structure level under study and the donor or acceptor level of the reference. The ionisation energy is represented by the energy difference between the neutral and charged structures:

$$\Delta E_d(0/+) = E_d(0) - E_d(+)$$
 (3.6)

Then the calculated donor level can be given by:

$$(0/+)_d = \Delta E_d(0/+) - \Delta E_r(0/+) + (0/+)_r$$
 (3.7)

where $\Delta E_r(0/+)$ is the calculated ionisation energy of the reference defect.

One of the advantages of this method is that there is a cancellation of errors in the two calculated values ΔE_d and ΔE_r , so the $(0/+)_d$ is often much more accurate than either of them.

3.4.2 Formation energy method

This method depends on the formation energies of charged and neutral defects where both should be of the same supercell size.

$$E^f(X, q) = E^t(X, q) - \sum_i \mu_i + q(E_v(X, q) + \mu_e) + \alpha_M \frac{q^2}{L\epsilon}, \quad (3.8)$$

where $E^t(X, q)$ is the total energy of the system, μ_i and μ_e are the chemical potentials of the atoms and electrons, respectively, E_v is the energy of valence band top in the defect cell, and the last term is called the Madelung correction or the correction for periodic boundary conditions. Usually this term is the monopole interaction but could also be a multipole interaction. α_M is the Madelung constant, L is a lattice parameter, and ϵ the permittivity of the material.

3.5 Electron Paramagnetic Resonance

Electron paramagnetic resonance (EPR) [62] is a technique which detects chemical species that have unpaired electron(s), and its use has identified a large number of centres in semiconductor materials. EPR is used successfully to study the microscopic structure and symmetry of defects.

In diamond the electronic structure of each carbon atom can be divided into the core electrons and valence electrons (with $(1s^2)2s^22p^2$ configuration). The latter are involved in the chemical bond, however the former are not. Diamond structures are created when s and p orbitals form tetrahedral sp^3 bonds forming four-fold coordinations with other C atoms. In perfect crystals, diamond acquires no net magnetic dipole moment as the number of spin up electrons is the same as spin down electrons. Furthermore with perfect directional bonds no orbital dipole moment can be obtained. By introducing a defect into the crystal, a level may be created associated with an unpaired electron in the band gap, which makes the structure EPR active. However in the case of $S = 0$ defects are EPR is inactive can be ionised thermally or optically. Depending on the position of the Fermi level, the donor and acceptor levels can either donate or accept an electron respectively, leaving the structure EPR active.

When an atom or molecule with an unpaired electron (where net spin is non-zero) is placed in a magnetic field, the spin of the unpaired electron can align either in the same

direction or in the opposite direction as the external field. This gives rise to what is known as the *Zeeman effect*. These two electron alignments have different discrete energies and the application of a magnetic field to an unpaired electron lifts the degeneracy of the $\pm\frac{1}{2}$ spins of the electron. This creates distinct energy levels for the unpaired electrons, making it possible for the net absorption of electromagnetic radiation in the form of microwaves to occur. To obtain an intense and constant microwave frequency, the sample is located in a microwave cavity with a variable applied magnetic field until resonance absorption occurs. Electromagnetic radiation with frequency ν gives rise to two different energy levels $h\nu$. The total angular momentum of a free paramagnetic ion is:

$$\mathbf{J} = \mathbf{L} + \mathbf{S} \quad (3.9)$$

where \mathbf{L} is the electron orbital angular momentum and \mathbf{S} electronic spin moment. The orbital angular momentum \mathbf{L} is simply due to system current loop.

$$I = \frac{-e\omega}{2\pi} = -e\nu \quad (3.10)$$

which gives rise to a magnetic dipole moment, μ_L

$$\mu_L = -\mu_B g_L \mathbf{L} \quad (3.11)$$

μ_B is the Bohr magneton and equals $e\hbar/2m_e c$, and $g_L=1$ is called the g_L factor associated with \mathbf{L} .

The electron spin moment leads to a second and predominant contribution, as for most defects in solids the orbital angular momentum is quenched.

$$\mu_S = \mu_B g_S \mathbf{S} \quad (3.12)$$

$g_S = 2.0023$ is called the g_S factor associated with \mathbf{S} , so the total magnetic dipole moment will be:

$$\mu = \mu_S = -\mu_B g_S \mathbf{S} \quad (3.13)$$

The Hamiltonian describes the interactions of the magnetic field.

$$\mathbf{H} = -\mu \cdot \mathbf{B} \quad (3.14)$$

Due to spin-orbit interaction ($\lambda\mathbf{L}\cdot\mathbf{S}$) the small term $\Delta\mathbf{g}$ should be added to g_S .

$$\mathbf{g} = g_S + \Delta\mathbf{g} \quad (3.15)$$

$\Delta\mathbf{g}$ represents the departure of \mathbf{g} from the isotropic free spin electron value $g_S=2.0023$ which depends on the orientation of the magnetic field applied with the crystallographic axis, so the Hamiltonian becomes:

$$H = -\mu_B\mathbf{S}\cdot\mathbf{g}\cdot\mathbf{B} \quad (3.16)$$

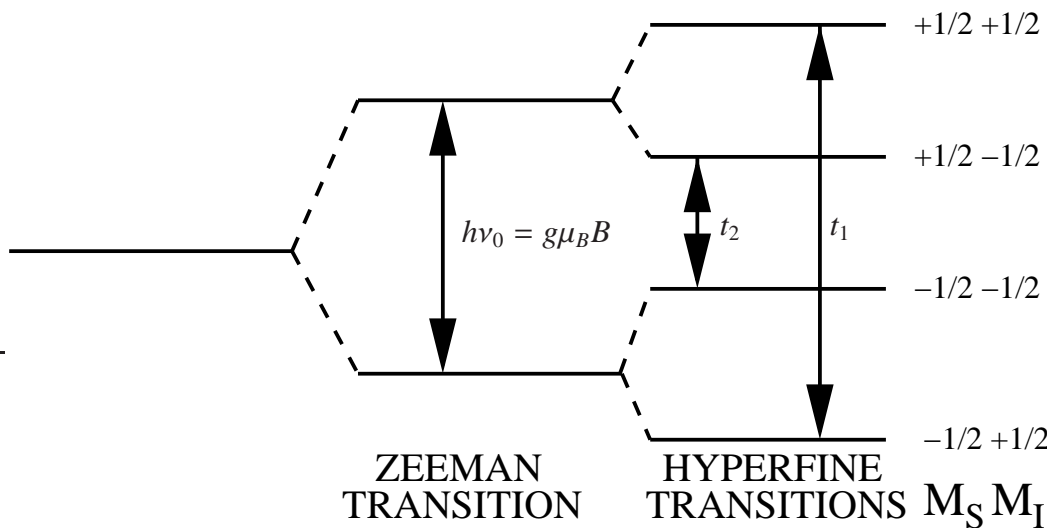


Figure 3.1: Schematic shows energy levels of a system with $S = 1/2$ and $I = 1/2$ in applied magnetic field.

A degenerate level splits as shown schematically in Fig. 3.1 (left split), where the energy splitting induced by the Zeeman effect is:

$$\Delta E = -\mu_B g B \quad (3.17)$$

Experimentally this is seen by varying the B field until the Zeeman splitting matches microwave radiation ν_0 , given an optical absorption.

$$B = \frac{h\nu_0}{g\mu_B} \quad (3.18)$$

When the applied field irradiates the sample at the resonant frequency ν_0 , transitions are induced in which unpaired electrons parallel to the field become anti-parallel, and vice versa, which give the absorption and emission processes. In cases of equal probability no net absorption or emission can be detected. However the lower level population is increased as a result of spontaneous emission and also spin lattice relaxation. The population ratio is governed by the Boltzmann distribution:

$$\frac{n_{\text{upper}}}{n_{\text{lower}}} = \exp\left(-\frac{\Delta E}{k_B T}\right) \quad (3.19)$$

where n_{upper} and n_{lower} are the number of paramagnetic centres occupying the upper and the lower energy states respectively, k_b is the Boltzmann constant, and T is the temperature in Kelvin.

3.6 Hyperfine Interactions

The previous section dealt only with an external magnetic field interacting with an unpaired electron spin. In the case of a nucleus with spin $I \neq 0$ present in a region of unpaired electron spin, so-called hyperfine interaction must also be considered in the spin Hamiltonian. As a result of the local field of the nuclear spin at the electron, there will be $(2I+1)$ orientations of nuclear spin in a magnetic field, all of which correspond to different energy levels. The right side of Fig 3.1 shows the interaction between $S = 1/2$ and $I = 1/2$, which gives rise to two transitions (t_1 and t_2) according to selection rules $\Delta M_S = \pm 1$ and $\Delta M_I = 0$. These two transitions combined with Zeeman splitting (the mid line) give rise to the EPR spectrum shown in Fig 3.2. If the KUL1 EPR centre is taken as an example, it is identified as a neutral silicon split vacancy defect [63]. So, in the presence of ^{29}Si ($S = 1/2$), ^{28}Si ($S = 0$) and ^{30}Si ($S = 0$) in the material, three lines would be observed: the centered main line from ^{28}Si and ^{30}Si and a single pair of satellite lines from ^{29}Si . The interaction between

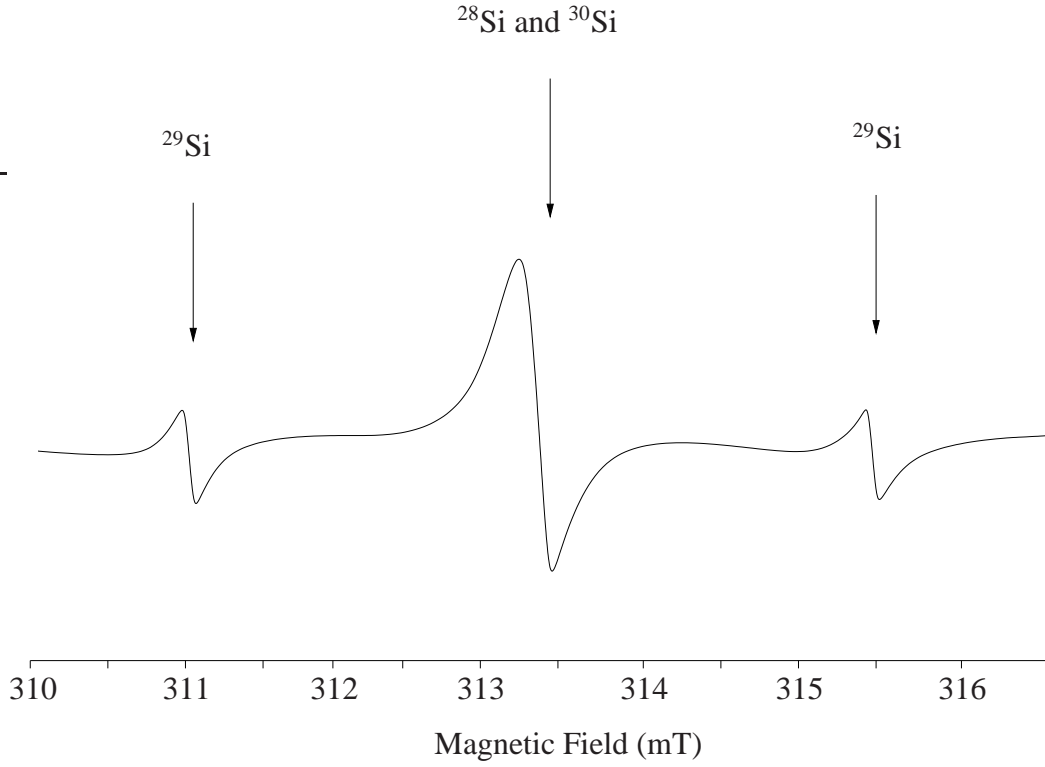


Figure 3.2: Schematic of EPR spectra for an unpaired electron $S = 1/2$ interacting with nuclear spin $I = 1/2$.

an unpaired electron magnetic moment μ_e and any nuclear magnetic moments μ_N in the vicinity of the unpaired electron is given by isotropic and anisotropic parts:

$$A_{\text{iso}} = \frac{2\mu_0}{3} g_e \mu_B g_N \mu_N |\Psi(0)|^2 \quad (3.20)$$

and

$$A_{\text{aniso}} = \frac{1}{4\pi} \mu_0 g_e \mu_B g_N \mu_N \left[\frac{3(\mathbf{I}\cdot\mathbf{r})(\mathbf{S}\cdot\mathbf{r}) - r^2(\mathbf{I}\cdot\mathbf{S})}{r^5} \right] \quad (3.21)$$

where $|\Psi(0)|^2$ is the wave function of the electron at the nucleus ($r = 0$) and \mathbf{I} and \mathbf{S} are the nuclear and electron spin operators, μ_0 is the permeability of vacuum, g_e is the electron g factor, μ_B is the Bohr magneton, and g_N is the gyromagnetic ratio of the nucleus and μ_N is nuclear magneton. r is the distance between the electron and the nucleus. Now, by integrating over the wave function, the Hamiltonian will be:

$$H_{HF} = \mathbf{S} \cdot \mathbf{A} \cdot \mathbf{I} \quad (3.22)$$

The hyperfine tensor \mathbf{A} could be isotropic or anisotropic as defined in Eq. 3.20 and Eq. 3.21 respectively, and also could be axially symmetrical, or diagonal with two components A_{\parallel} and A_{\perp} . In this case the Hamiltonian can be written as:

$$H = A_{\perp}(I_x S_x + I_y S_y) + A_{\parallel} I_z S_z = (A_{\text{iso}} - A_{\text{aniso}})S \cdot I + 3A_{\text{aniso}}S_z I_z \quad (3.23)$$

where $A_{\parallel} = A_{\text{iso}} + 2A_{\text{aniso}}$ and $A_{\perp} = A_{\text{iso}} - A_{\text{aniso}}$. A_{\parallel} and A_{\perp} can be written as functions of the spin density:

$$A_{\text{iso}} = \frac{8\pi}{3} \frac{\mu_0}{4\pi} g_e \mu_B g_I \mu_n \rho_{\text{spin}}(r) \quad (3.24)$$

and

$$A_{\text{aniso}} = \frac{1}{4\pi} \mu_0 g_e \mu_B g_I \mu_n \int \rho_{\text{spin}}(r) \frac{3\cos^2(\theta) - 1}{2r^3} d^3 r \quad (3.25)$$

where r is the electron coordinate and θ is the angle between r and the symmetry axis. ρ is the difference between the electron charge densities of spin up and spin down, which can be obtained from AIMPRO. The Hamiltonian with the additional term will be:

$$H = \mu_B \mathbf{S} \cdot \mathbf{g} \cdot \mathbf{B} + \sum_j \mathbf{S} \cdot \mathbf{A}_j \cdot \mathbf{I}_j \quad (3.26)$$

The tensor \mathbf{A}_j contains information about the distance between the nuclear and electron spins and the symmetry of the electron spin density. AIMPRO can calculate the tensor \mathbf{A}_j and this can then be directly compared with experimental values. The hyperfine values can give qualitative information about the symmetry and maybe the type of atoms involved. Furthermore the positions of the nuclei can be obtained by comparison with the theoretical values provided for various possible structures. The directions of the \mathbf{A} tensor in some cases refer to spherical polar coordinates, as shown in Fig. 3.3. Spherical-polar angles, (θ, ϕ) are given with θ the polar angle relative to [001], and the azimuth from [100], quoted in degrees.

Hyperfine-interactions are modelled as outlined previously [51]. Briefly, this involves the combination of pseudopotentials and reconstructed all-electron wave functions in the

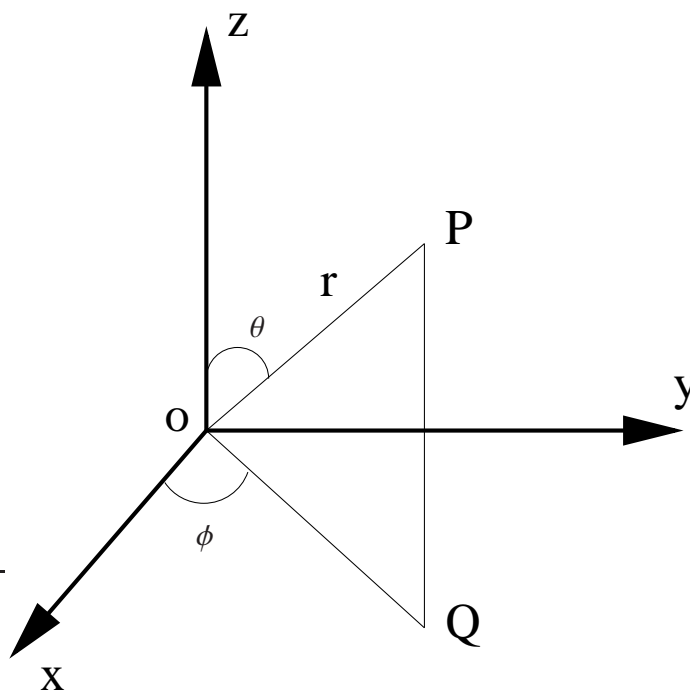


Figure 3.3: A spherical coordinate system with origin O.

core region [52, 64]. Reconstruction of the ion cores allows us to calculate the hyperfine tensor elements within a frozen-core all-electron wave function approximation, without the computational difficulties associated with a full all-electron calculation. In the text also presents simplified terms A_s and A_p for the isotropic and anisotropic components of a hyperfine tensor. In the case of axially symmetric tensors, these are given by $(A_{\parallel} + 2A_{\perp})/3$ and $(A_{\parallel} - A_{\perp})/3$, respectively, where A_{\parallel} is the magnitude of the component along the axial direction and A_{\perp} that of the two components perpendicular to the axis. Where the symmetry is only approximately axial, A_p is calculated using A_{\perp} taken as the average of the two nearly degenerate terms. In this thesis quotes hyperfine tensors calculated for ^{13}C and ^{14}N . In the latter case, the ^{15}N values can be obtained from those of ^{14}N simply by multiplication by -1.32 , a factor given by the ratio of nuclear magnetic moments divided by the corresponding nuclear spins. The calculated directions are unaffected by isotope. For the calculated hyperfine interactions, an enhanced carbon wave function basis consisting of 28-functions per atom is used to ensure a reasonable level of convergence.

3.7 Muon Spin Relaxation (μ SR)

The μ in the acronym μ SR is the Greek letter mu which stands for muon. From the acronym μ SR it can be recognised an analogy between μ SR and electron spin resonance (EPR) and nuclear magnetic resonance (NMR). μ SR is a powerful experimental technique which depends on implanted spin polarised muons in a material whose magnetic moment is 3.18 times higher than a proton. It gives rise to high microscopic sensitivity to probe magnetic moment which allows knowledge to be gained of what is going on inside materials such as semiconductors.

The muon was discovered in 1937 in cosmic rays. It has a mass about 200 times that of an electron, and scientists consider negative muons as heavy electrons, whereas positive muons are considered as light protons (9 times lighter than a proton).

The muon has a short lifetime of about 2.2 microseconds ($2.2\mu s$). They can be produced using a particle accelerator, using high-energy protons to produce pions, which then decay in very short lifetimes of about 26 billionths of a second into muons and muon neutrinos (antineutrinos). Beams of nearly 100% spin polarised muons with the beam direction shot into a material can be coupled to their local magnetic field environment via their spin. The muons spin around the local magnetic fields in the material, and unstable muon decay relies on the violation of parity into positrons (anti-electrons) emitted along the direction of muon spin.

Positive muons can trap electrons and become the so-called hydrogen-like atom muonium ($\text{Mu} \equiv \mu^+ e^-$), which is considered chemically as a light isotope of hydrogen. Mu has about Bohr radius and ionisation potential of hydrogen. Tables 3.1 and 3.2 respectively illustrate the properties of muon compared to proton and muonium compared to hydrogen.

Muonium can be used by scientists to examine how hydrogen atoms react in materials where hydrogen plays a big role in changing conductive behaviour. What is observed in muon spin resonance spectroscopy is hyperfine coupling between μ^+ and an electron, which AIMPRO can calculate.

Table 3.1: Muon compared to proton.

Property	Muon (μ^+)	Proton (p^+)
Mass (m_e)	206.768	1836.15
Charge (e)	+1	+1
Spin	1/2	1/2
Magnetic moment (ratio)	3.18	1
Half-life (μs)	2.2	stable

Table 3.2: Muonium compared to hydrogen.

Property	Muonium (Mu)	Hydrogen (H)
Reduced mass (m_e)	0.995	0.999
Radius (\AA)	0.531	0.529
Ionisation energy (eV)	-13.54	-13.59

3.8 Conclusion

The AIMPRO package can calculate many quantities which are of direct interest to an experimentalist. The following chapter looks at a series of materials problems in which the exploitation of this theory can give a deeper understanding of defect physics.

Part II

Applications

CHAPTER

4

Nitrogen-Pair Paramagnetic Defects

4.1 Introduction

As indicated in section 1.3, natural diamonds are classified by nitrogen content [65], with type-Ia referring to those which contain nitrogen in an aggregated form, and type-Ib containing N as isolated impurities (N_s^0), sometimes labelled as C-centres (Fig. 4.1(b)). Nitrogen aggregates are principally of A and B form, and the A-centre structure is illustrated in Fig. 4.1(d). The driving force for aggregation is the reduction in energy concomitant with the removal of carbon radicals associated with N_s^0 . Previous computational simulations have shown that the formation energies per N atom of A and B centres are 2.0 and 2.9 eV lower than that of a C-centre [66].

N_s^0 has been thoroughly characterised. It possesses an unpaired electron and is observed as the P1 electron paramagnetic resonance (EPR) centre [67]. Analysis of the hyperfine

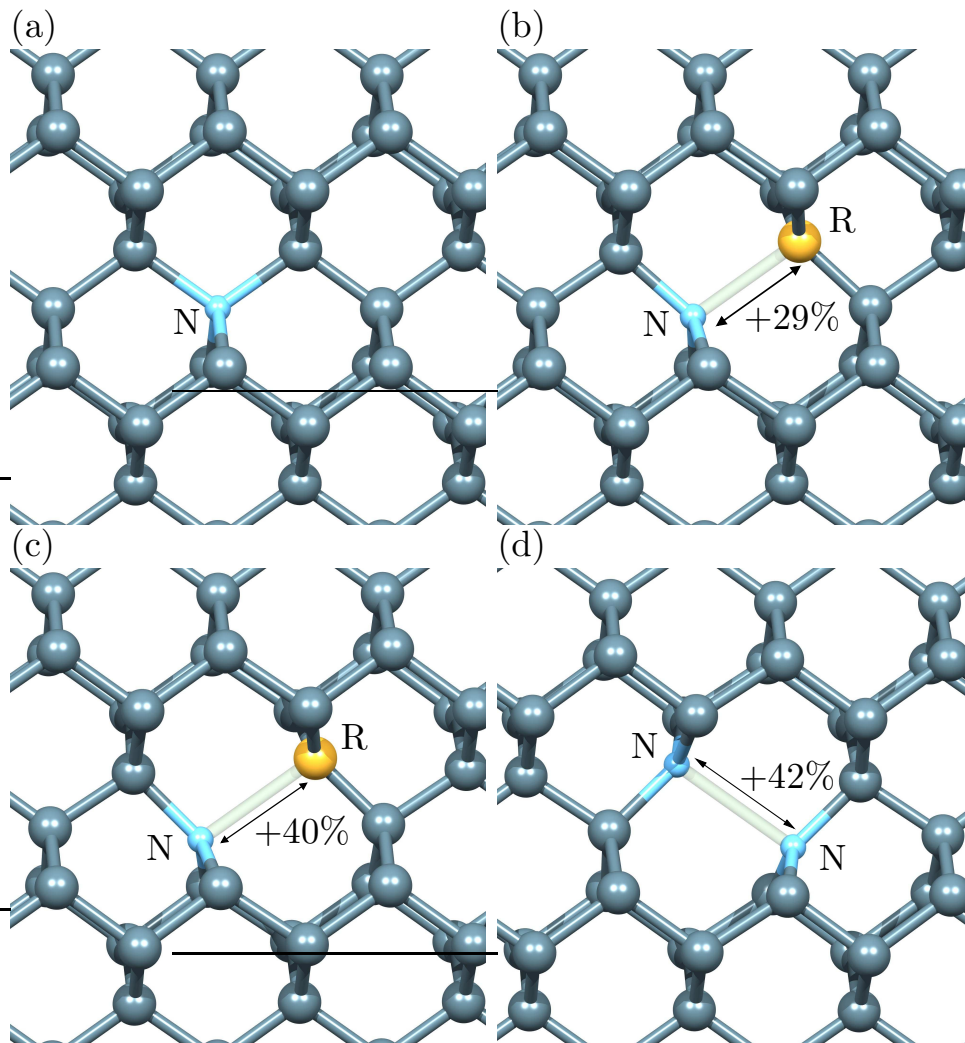


Figure 4.1: Schematics showing the calculated structures of nitrogen defects in diamond: (a) ionised C-centre (N_s^+), (b) neutral C-centre (N_s^0), (c) negatively charged C-centre (N_s^-), and (d) A-centre. Labelled sites are N for nitrogen and R indicating the carbon radical or anion site. Horizontal and vertical directions are approximately $[110]$ and $[001]$, respectively. Percentages indicate the calculated extension of the respective interactions over that of the host C–C bond-length. The transparent cylinders represent broken bonds.

interaction [67] with the ^{13}C and ^{14}N species in P1 suggests that 67% and 25% of the spin-density are associated with the central C and N atoms respectively. This is consistent with the band-gap orbitals being a carbon radical and nitrogen lone-pair (Fig. 4.2). The neutral

and ionised forms also give rise to vibrational modes [68, 69] at 1344 cm^{-1} and 1332 cm^{-1} respectively.

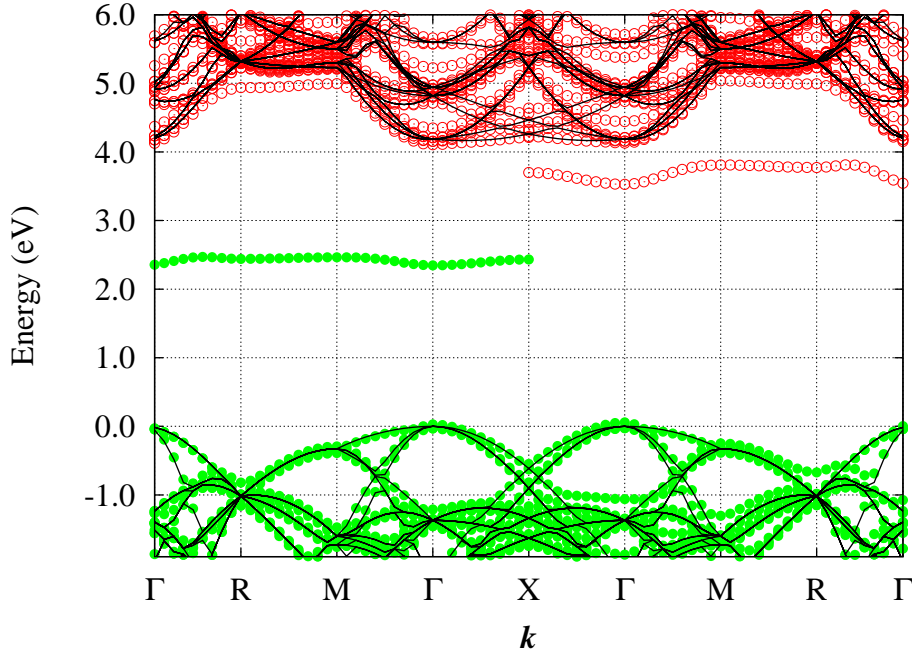


Figure 4.2: The Kohn-Sham band structure in the vicinity of the band-gap for the P1 centre (N_5^0). Filled and empty circles show filled and empty bands respectively, with the bands from the defect-free cell superimposed in full lines for comparison. The energy scale is defined by the valence band top at zero energy ($E_v = 0\text{ eV}$). The left and right panels show the spin up and down spectra, respectively. The path of the k -points are illustrated in the Brillouin zone of a simple-cubic (Fig.1.2(b))

A-centres are also characterised by vibrational modes resonant with the diamond host phonons and seen as broad peaks in infrared [70]. Indeed, the labels A, B and C for different forms of nitrogen in diamond originate from the labelling of IR absorption bands. In contrast with C-centres, A-centres have only paired electrons and are EPR-inactive. However, they may be photo-ionised (with an activation energy [71] of 3.8 eV), and in the positively charged state give rise to the W24 EPR spectrum [72, 73].

In addition to ionised A-centres, five $S = 1/2$ EPR centres have been attributed to pairs of N atoms, but these are separated by a number of intervening host sites. The N1 [3, 4],

W7 [6, 74, 75], M2 [7, 76], N4 [77, 78], and M3 [7, 76] EPR centres have models which consist of substitutional nitrogen atoms at the second to sixth shells of neighbouring sites respectively, as shown in Fig. 4.3. In contrast to W24, the ionised state does not require illumination.

Configurations of nearby P1-centres adopting a $S = 1$ spin state have also been detected: the NOC-1, NOC-2, NOC-3, and NOC-4 EPR centres [1]. Models for these centres are C-centres at 4th, 7th (or 9th), and 10th shells for NOC-1, NOC-2, and NOC-3, while NOC-4 is a superposition of spectra from more distant pairs.

N-pairs have previously been analysed as part of a broader study into the stability of impurity pairs in diamond [79]. The present study focuses on the expected hyperfine interactions for the proposed dissociated, ionised nitrogen-pair models and, by analysing the reorientation barriers, revises the models. Also the origin of cases of $S = 1$ combinations of nearby P1-centres is investigated. In so doing, it should be possible to explain why only some combinations are seen.

4.2 Methodology

All calculations were carried out using the density functional technique, implemented in AIMPRO as described in chapter 2. The wave function basis of carbon is treated using fixed linear-combinations of s - and p -orbitals with the addition of a set of d -functions to allow for polarisation, with a total of 13 functions per atom. Nitrogen is treated using independent sets of s -, p - and d -Gaussians with four widths, yielding 40 functions per atom. The charge density is Fourier-transformed using plane-waves with a cut-off of 350 Ry, yielding well-converged total energies. Core-electrons are eliminated by using norm-conserving pseudopotentials [53]. The lattice constant and bulk modulus of bulk diamond are reproduced to within $\sim 1\%$ (an overestimate) and 2% (underestimate) respectively of experimental values. The calculated direct and indirect band gaps agree with published plane-wave values [80].

Generally 216-atom, simple-cubic supercells of side length $3a_0$ are used. This ensures

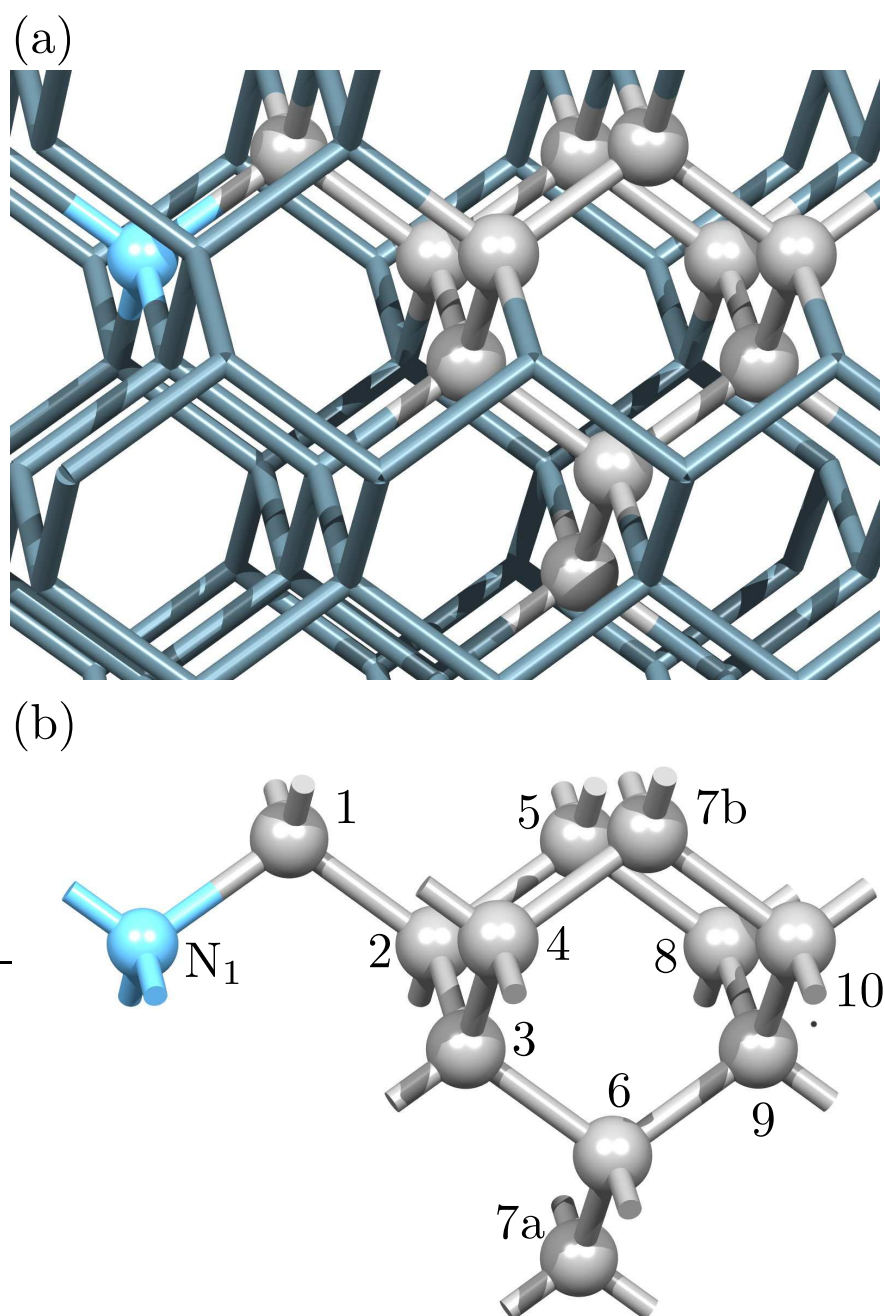


Figure 4.3: Schematics showing shells of neighbours in diamond: (a) sites embedded in the diamond lattice; with (b) showing only prototypical sites for each shell of neighbours relative to the first nitrogen site, N_1 . The two types of seventh-shell site are labelled 7a and 7b in accordance with Ref. [1].

that the N atoms are closer to one another than to any of the periodic images. For tenth-shell pairs, this is insufficient, and so a 256-atom cell with body-centred-cubic lattice vectors was used here. In all cases of sampling the Brillouin-zone by using the Monkhorst-Pack scheme [56], a sampling density of $0.64 \times 10^{-3} \text{ \AA}^{-3}$ per point or better was used. The estimation of error in the relative energies of different structures due to the Brillouin-zone sampling of $< 10 \text{ meV}$ was also tested.

In this chapter the donor levels are obtained in comparison to N_s^0 with a level at $E_c - 1.7 \text{ eV}$ [16].

4.3 Computation results

Substitutional nitrogen pairs at increasing distances are modelled. In each case geometry, electronic structure, electrical activity, reorientation barriers and, for $S = 1/2$ systems, hyperfine interaction are investigated. For neutral pairs, from all combinations of pairs of dilated N–C, one per N-site are optimised. $S = 0$ and $S = 1$ configurations have been examined with the potential anti-ferromagnetic interaction where the two N-sites are of opposite spin. Relaxation has also been initiated starting from $N_s^+ \dots N_s^-$. Throughout this chapter the notation is adopted where N-pairs in the n^{th} shell (Fig. 4.3) are labelled NnN .

The energy convergence was examined for some structures by conducting comparisons of the \mathbf{k} -point, basis cell and cell size. Table 4.1 indicates the difference between the four different sites in term of wave functions, the Brillouin-zone sampling using the Monkhorst-Pack scheme, and supercell size. The results are shown to be satisfactory, with very close values from the Monkhorst-Pack scheme with a uniform mesh of $2 \times 2 \times 2$ (MP222) and $4 \times 4 \times 4$ (MP444), and between the two wave function bases of 13 functions per atom (known in AIMPRO terminology as $C44G^*$) and 22 functions per atom (in AIMPRO known as $pdpp$).

Finally, the results are presented in order of increasing N–N separation.

Table 4.1: Relative energies for different structures with different cell size (216 and 512), wave function basis ($C44G^*$ and $pdpp$) and \mathbf{k} -points (MP222 and MP444). The zero of energy is set to the A-centre (N1N).

	Relative Energy (eV)							
	$C44G^*$				$pdpp$			
	MP222		MP444		MP222		MP444	
Supercell size	216	512	216	512	216	512	216	512
N2N	3.29	3.29	3.29	3.29	3.29	3.29	3.29	3.29
N3N	3.26	3.26	3.26	3.26	3.25	3.25	3.25	3.25
N4N	3.75	3.78	3.75	3.78	3.75	3.78	3.75	3.78
N5N	2.42	2.41	2.42	2.41	2.41	2.40	2.41	2.40
N6N	3.68	3.69	3.68	3.69	3.68	3.68	3.67	3.68
N8N	2.19	2.18	2.19	2.18	2.15	2.14	2.15	2.14

Table 4.2: Hyperfine tensors (MHz) for ^{14}N and their six ^{13}C neighbours in (N1N)⁺. Directions are indicated in parentheses using spherical polar coordinates. Experimental data for W24 are taken from Ref. [2]. All calculated data are rounded to the nearest MHz or degree.

Site	A_1	A_2	A_3	A_s	A_p
Calculations					
^{14}N	156 (125, 45)	74 (57, 343)	74 (53, 103)	101	27
^{13}C	-13 (90, 315)	-12 (9, 225)	-8 (81, 45)	-11	
Experiment (W24)					
^{14}N	155.26 [111]	81.51 \perp [111]	81.51 \perp [111]	106.09	24.58
^{13}C				12.3	

4.3.1 First-shell pairs and W24

N1N has been examined previously, and only the main points are reviewed here. The relaxed structure results in a significant dilation of the N–N distance relative to that of the host C–C bond-length, as indicated in Fig. 4.1(d). All atoms are coordinated according to their valence, and the band-gap is devoid of the partially filled states characteristic of the nitrogen donor as shown in Fig. 4.4. Above the valence band top lies an occupied-state associated with the nitrogen lone-pair orbitals. It may be noted in passing that there are metastable forms of N1N containing a N–N bond and two carbon radicals. However, these are > 4 eV higher in energy than the A-centre and are of no practical importance.

Photo-ionisation of N1N yields the W24 EPR centre [72, 73]. Ionisation is found here to reduce the dilation of the N–N separation from 42% to 31%, but the N atoms remain equivalent and the overall symmetry is D_{3d} . The calculated hyperfine interactions for the N atoms and their six equivalent carbon neighbours are presented in Table 4.2. The agreement with experimental values is excellent, lending confidence both to the assignment of W24 to the ionised A-centre, and the values presented below for the dissociated N-pairs. The sign of A_s for ^{13}C is not known experimentally, but can now be predicted to be negative.

The ease with which N1N is ionised may be estimated from two sets of data. As a purely qualitative picture, the Kohn-Sham band-structure (Fig. 4.4) shows an absence of any bands deep in the gap, which would be consistent with the need for illumination to ionise the A-centre. A more quantitative approach is to calculate the ionisation level relative to a marker system [81]: the donor-level of an A-centre is calculated to lie 2.0 eV lower than that of a C-centre, locating it at $E_c - 3.7$ eV. This hyper-deep level is in close agreement with the experimental [71] value of $E_c - 3.8$ eV.

4.3.2 Second-shell pairs and N1

There are several meta-stable structures for N2N, but the lowest in energy exhibits a single dilated N–C bond, shown schematically in Fig. 4.5. The on-site location for one N atom may indicate that N2N adopts a N_s^- -C- N_s^+ form. The next most stable structure is 0.5 eV

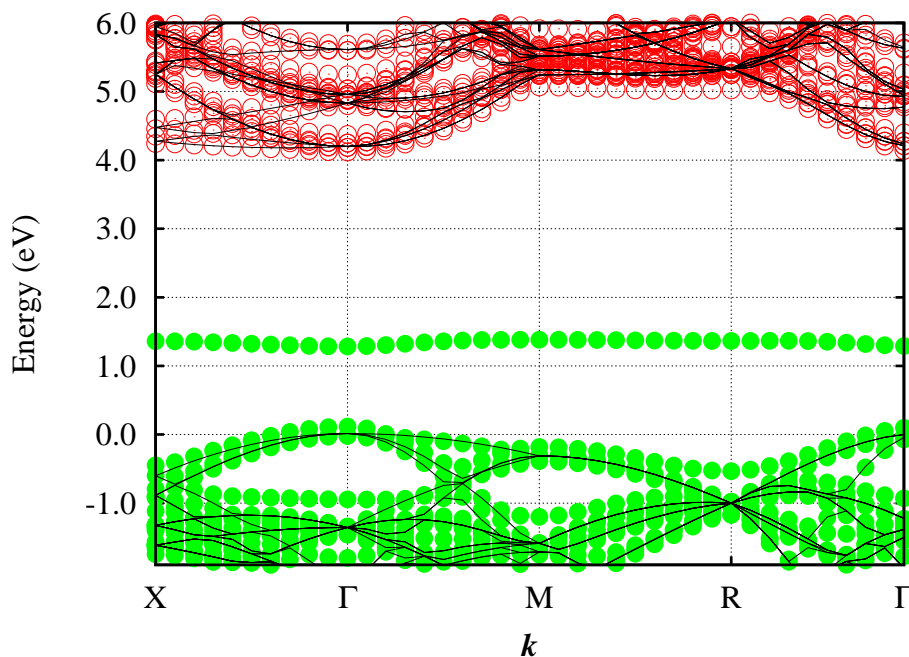


Figure 4.4: The Kohn-Sham band structure in the vicinity of the band-gap for (N1N). Symbols and scales are as indicated in Fig. 4.2.

higher in energy, with $S = 1$ and two dilated bonds.

The N1 EPR centre has been assigned to $(\text{N2N})^+$ [5]. In support of this, N2N was found here easier to ionise than an A-centre, with a donor level at $E_c - 1.9$ eV. Then mid-gap acceptors, such as vacancies [82], may ionise these defects without the need for illumination. An effect of ionising N2N is a reduction in the broken N–C dilation from 41% in the neutral charge state to 30% in the positive charge state. This is close to the calculated reduction in the dilation of N_s^- to N_s^0 , supporting the view of the charge-transfer between the N-sites in the neutral charge state of N2N.

The calculated hyperfine tensors for key atoms in $(\text{N2N})^+$ are listed in Table 4.3. Experiments indicate hyperfine tensors for two non-equivalent nitrogen sites in N1, and the agreement between the calculations and measurements is rather good. Additionally, spectra for nearby ^{13}C sites have been reported [4, 5]. Perhaps surprisingly, the large hyperfine interaction with the central carbon atom (C_1 , Fig. 4.5) is not one of them, but three more remote types of neighbour are labelled I, II, and III. Table 4.4 lists the calculated values

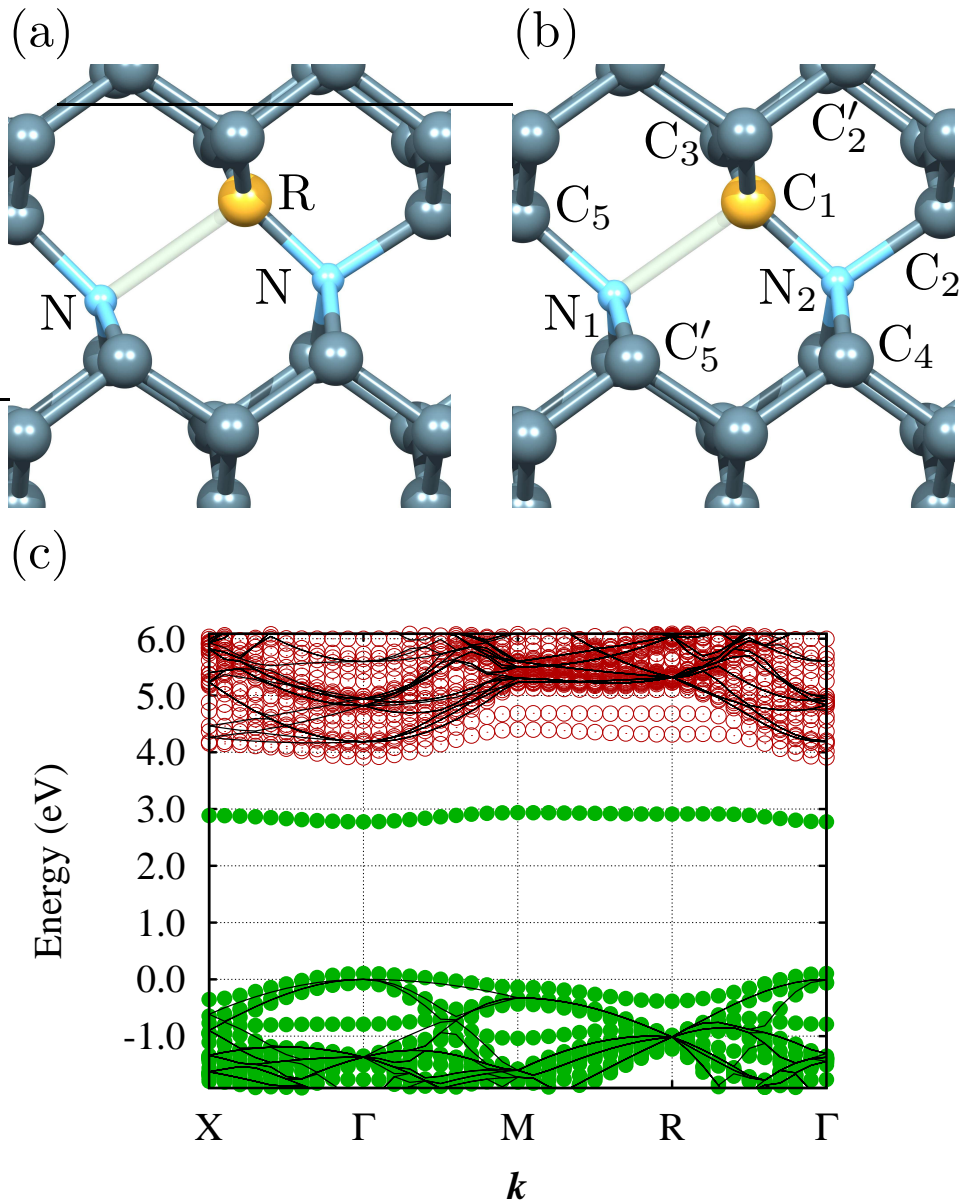


Figure 4.5: Schematics of N2N in diamond in the (a) neutral and (b) positive charge states. Colours and axes are as in Fig. 4.1. (c) The Kohn-Sham band structure in the vicinity of the band-gap for (N2N). Symbols, axes and scales are as indicated in Fig. 4.1 and Fig. 4.2.

for the isotropic and anisotropic contributions of the hyperfine tensors for carbon sites as labelled in Fig. 4.5. A good fit to experimental values [5] can be made by assigning sites I, II and III to $(C_2+C'_2)$, C_4 and C_3 , respectively.

Table 4.3: Calculated hyperfine tensors (MHz) for ^{14}N and ^{13}C , for the sites identified in Fig. 4.5. Tensors are listed as in Table 4.2, and the experimental data for N1 are taken from Ref. [3].

Site	A_1		A_2		A_3	
Calculations						
$^{14}\text{N}_1$	124	(55, 45)	80	(35, 224)	80	(90, 135)
$^{14}\text{N}_2$	-7	(90, 135)	-7	(23, 45)	-7	(67, 225)
$^{13}\text{C}_1$	408	(54, 45)	200	(90, 315)	199	(36, 225)
Experiment (N1)						
$^{14}\text{N}_1$	126.36	(55, 45)	89.20	(35, 225)	89.22	(90, 135)
$^{14}\text{N}_2$	-8.33	(90, 135)	-8.29	(20, 45)	-7.88	(70, 225)

It is perhaps surprising that C_2 and C'_2 have numerically indistinguishable hyperfine tensors, given that C_2 has a N-neighbour, and the other does not. It should be noted that, for the C_4 sites in Fig. 4.5(b), if N_2 is disregarded, there are an additional four sites symmetrically arranged relative to the N_1 - C_1 axis. However, the computed values of A_s and A_p for the four additional sites are around half that of C_4 , and as such should be distinguishable in experiment.

The present assignment of ^{13}C -sites partially agrees with the interpretation of experimental results. Due to the overall planar symmetry of the defect, the number of equivalent sites can be only 1 or 2, and not 3. For the assignment of three equivalent ^{13}C in site-I, the unique C_2 and the two labelled C'_2 in Fig. 4.5(b) would have to be combined. However, the calculated values for these non-equivalent sites are numerically the same, and thus this assignment may be supported despite the C_2 and C'_2 sites being non-equivalent by symmetry. The assignment of the experimental site III to the two C_3 sites is also in accord with calculations. However, type II sites have to be re-assigned to C_4 from $C_5+C'_5$, for which very small hyperfine interactions are found. This requires a change in the number of equivalent C-sites from 3 to 2.

Table 4.4: ^{13}C hyperfine for sites in N2N (Fig. 4.5), and those obtained experimentally for the N1 EPR centre, with labels and values taken from Refs. [4, 5]. n indicates the number of equivalent sites in each case.

Site	A_s	A_p	n
Calculations			
C ₁	269	70	1
C ₂	29	3	1
C' ₂	29	3	2
C ₃	-21	~ 1	2
C ₄	14	2	2
C ₅	-6	1	1
C' ₅	-6	1	2
Experiment (N1)			
I	28.3	2.6	3
II	21.3	0.6	3
III	16.7	1.1	2

The reorientation barriers also have been examined, yielding 1.4 eV and 0.7 eV in the neutral and positive charge states respectively as shown in Fig. 4.6. The reorientation barrier for N1, assigned to the positive charge state, has been measured experimentally [3, 83] to be 0.4 eV. The apparently large difference between the calculated and experimental values is mitigated by two factors. First, the calculation is classical, and quantum-mechanical effects such as tunnelling would tend to lower the effective barrier. Indeed, the distance travelled by the radical site is small and it remains on the same C atom throughout the process. Secondly, there is only a single measurement of the activation energy, and the uncertainty in the value is not clear. Given these factors, the agreement can be viewed as tolerable. It is shown later that the calculated activation energies for other N-pair configurations are somewhat different from that for (N2N)⁺, and overall the trend in the energetics fits well

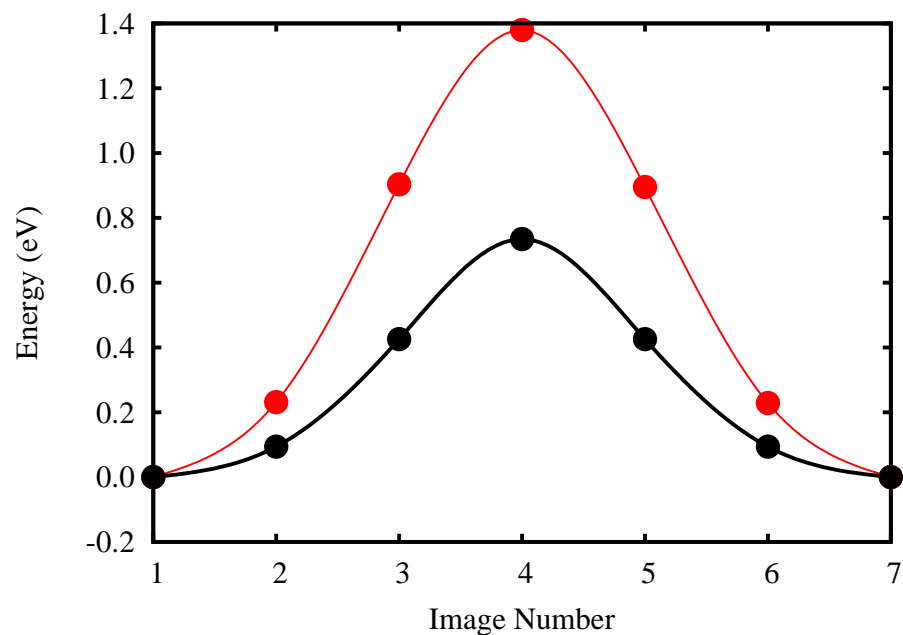


Figure 4.6: The barrier of energy between (N – CN) and (NC – N) in neutral (red line) and positive (black line) charge states.

with observation.

In summary, from combining the ground state structures, hyperfine interaction data, ionisation energy and reorientation barrier, it is concluded here that the modelling agrees with the assignment of N1 to (N2N)⁺, subject to the revision of the assignments for nearby carbon hyperfine interactions and the number of equivalent sites.

4.3.3 Third-shell pairs and W7

The most stable structure found for N3N has C_2 symmetry and is shown in Fig. 4.8(a). In contrast with N2N, each N-site has an associated broken N–C bond, which is favoured in this case since the neighbouring carbon radicals form a partial p_π -bond as shown in Fig. 4.7(a). The re-bonding renders it 0.5–0.8 eV more favourable than other metastable structures.

The corresponding band structure is plotted in Fig. 4.8(c). Again, it contrasts with that

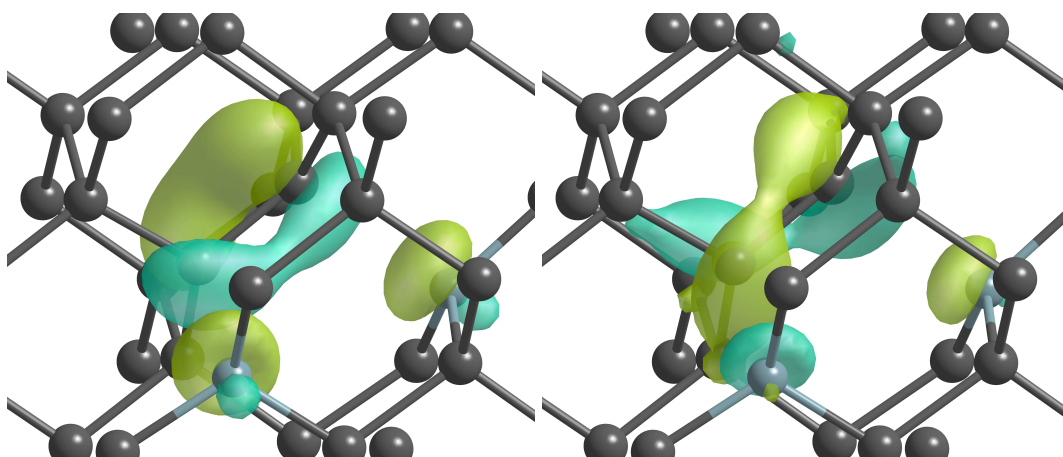


Figure 4.7: Kohn-Sham functions for N3N between two neighbouring carbon radicals: (a) partial p_{π} -bond, and (b) partial p_{π}^* -bond.

of N2N (Fig. 4.5(c)), with both occupied and unoccupied bands lying well within the band-gap. These roughly correspond to p_{π} and p_{π}^* combinations of the two C-radical sites, as shown in Fig. 4.7(a) and (b) respectively.

Upon ionisation, one broken bond reforms, leaving a paramagnetic centre resembling a perturbed P1 defect. This $S = 1/2$ complex has been assigned to the W7 EPR centre [5], and in Table 4.5 the calculated hyperfine interactions are reported in comparison to the measured values.

The agreement in both magnitude and direction for the N_s^0 component is good. Furthermore, the directions for the ionised N site are reasonable, and the isotropic components computed at 18 MHz agree well with the measured value of 15 MHz. It is concluded that the calculations are consistent with the $(N3N)^+$ model for the W7 EPR centre.

Loubser and Wright noted that for measurements between 77K and room temperature, motional effects became important [75]. They interpreted their data in terms of a reorientation barrier of $0.24 \text{ eV} \pm 0.01 \text{ eV}$. The process of reorientation in the case of $(N3N)^+$ is somewhat more complicated than for N2N, because there are at least three different reorientation reactions which result in a symmetrically equivalent product, as illustrated in Fig. 4.9.

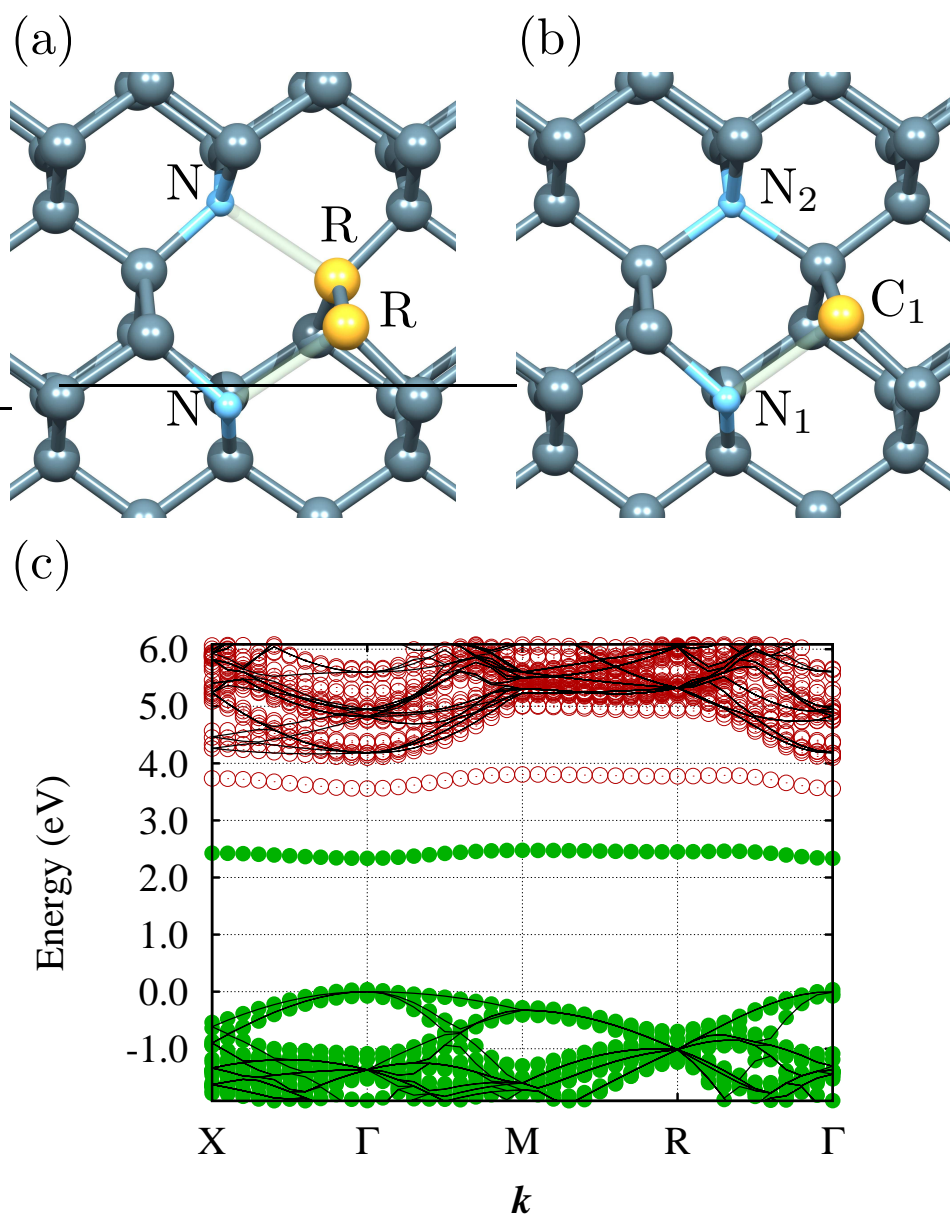


Figure 4.8: Schematics of the N3N complex in diamond in the (a) neutral and (b) positive charge states, with (c) showing the Kohn-Sham band structure in the vicinity of the band-gap for (N3N). Symbols, axes and scales are as indicated in Fig. 4.1 and Fig. 4.2.

Barriers have been calculated in three cases. The lowest energy is path (i), at 0.18 eV, with path (ii) activated by 0.40 eV. Trajectory (iii) is not favoured, with a route made up from path (i)+(ii) or, equivalently, (ii)+(i) energetically preferred. It is therefore predicted

Table 4.5: Calculated hyperfine tensors (MHz) for ^{14}N and ^{13}C , for the sites identified in Fig. 4.8. Experimental data are taken from Ref. [6]. Notation is as in Table 4.3. The motional averages are indicated as dynamic values for A , with the two cases as indicated in the text.

Site	A_1	A_2	A_3
Calculations (static)			
$^{14}\text{N}_1$	116 (125, 134)	77 (89, 45)	77 (35, 136)
$^{14}\text{N}_2$	20 (56, 74)	17 (116, 3)	17 (45, 303)
$^{13}\text{C}_1$	378 (55, 315)	179 (80, 52)	179 (37, 155)
Calculations (dynamic, C_2)			
$^{14}\text{N}_1$	68 (53, 46)	47 (131, 94)	47 (116, 338)
Calculations (dynamic, C_{2h})			
$^{14}\text{N}_1$	60 (90, 45)	55 (2, 135)	47 (92, 135)
Experiment (W7)			
$^{14}\text{N}_1$	121.39 [111]	86.00 \perp [111]	86.00 \perp [111]
$^{14}\text{N}_2$	16.01 (66, 71)	14.00 (123, 358)	13.58 (42, 313)

that reorientation will occur in two stages. The first activation involving path (i) results in an average structure with C_2 symmetry, similar to the structure in Fig. 4.8(a). At higher temperatures, path (ii) becomes accessible and the effective symmetry is raised to C_{2h} . Since the radical site is moving in this case (contrasting with N2N), the impact of quantum tunnelling is likely to be reduced. The barriers proposed are in good agreement with the experimental estimates, lending further support to the model.

Table 4.5 also lists hyperfine tensors where motional averaging is applied. Neither yield values resembling the experimental values for W7, supporting the assignment to a static geometry.

Finally, It is noted that, as with the N2N complex, the band-structure (Fig. 4.8(c)) is suggestive of a donor level in the upper part of the band-gap, and the calculated donor level

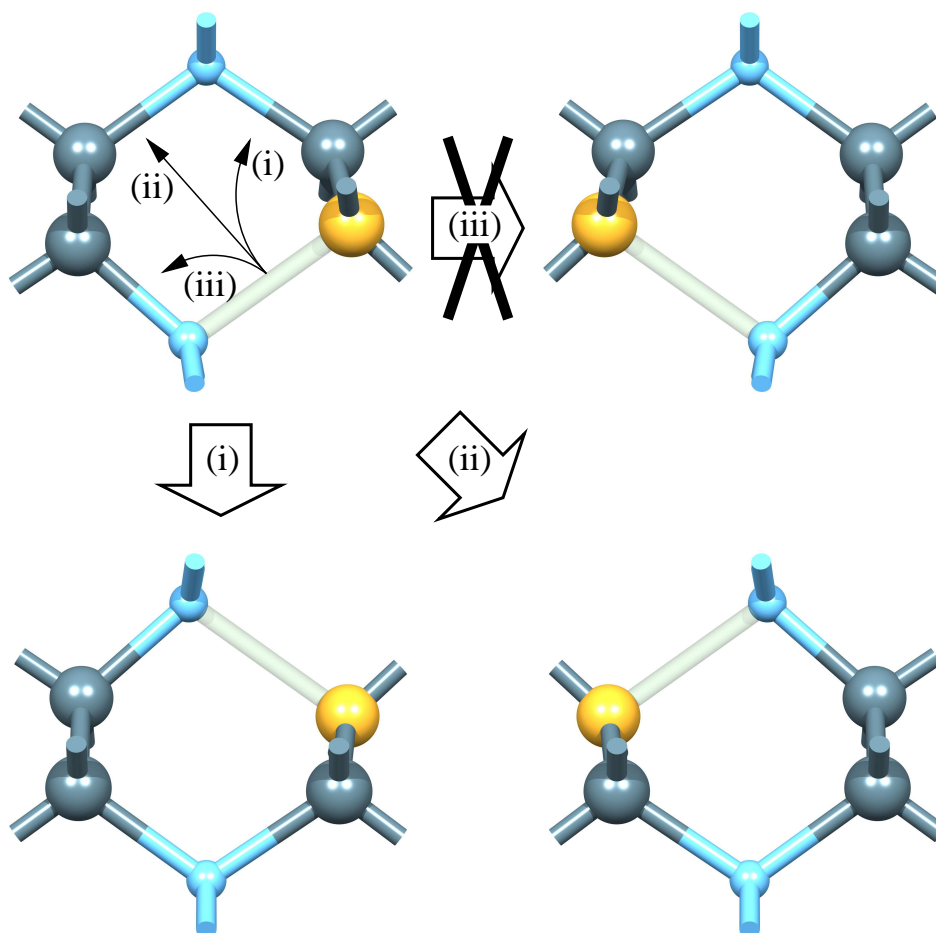


Figure 4.9: Schematic showing three modes for reorientation as discussed in the text for $(\text{N3N})^+$. Colours and orientation as in Fig. 4.1.

for N3N is estimated to lie around $E_c - 2.1$ eV. The increase in ionisation energy can be traced to the stabilisation of the neutral system due to the partial p_π -bonding interaction between dangling bond orbitals.

In conclusion, combining structure, electrical, motional and hyperfine data, the calculations support the assignment of W7 to a static $(\text{N3N})^+$ structure.

4.3.4 Fourth-shell pairs and M2

Fourth shell neighbours lie along the cube directions. Two substitutional nitrogen atoms paired in such a configuration are shown schematically in Fig. 4.10. As with N3N , it is

found that a structure maintaining two C-radicals is most stable. However, in this case there is no single minimum energy structure.

The C_{1h} and C_2 symmetry, $S = 0$ structures shown in Figs. 4.10(a) and (b) are within 50 meV of each other, with the planar structure being the most stable. Structure (c) in an $S = 1$ state is the model for NOC-2, and this is calculated to be 60 meV higher in energy than the diamagnetic form. This centre is discussed further in section 4.4.3. These energy differences are small, and it is not clear which of these structures is the true ground state. However, it can be noted that the case where the radical sites are most distant is higher in energy by 0.6 eV, in line with a general trend for increasing energy with separation of the radical sites.

In the positive charge state, one N–C bond reforms. The non-equivalence of the N-sites yields C_{1h} symmetry, with the lowest energy structure shown in Fig. 4.10(d). The N-centres weakly interact and the calculated donor level is estimated to lie approximately 0.1 eV deeper than that of N_s^0 (Fig. 4.11). This structure has been assigned to the M2 EPR centre [7], and the calculated hyperfine tensors for $(N4N)^+$ are compared to those of M2 in Table 4.6. The agreement between the P1-like N-site hyperfine and experimental values is reasonable, and although the values for the second N-site are somewhat overestimated, the directions are in good agreement.

The reorientation of $(N4N)^+$, transferring the unpaired electron between N sites, is found to be activated by 0.3 eV as shown in Fig. 4.12. As with the $(N3N)^+$ complex, reorientation about a single N site is not preferred energetically (see Fig. 4.9). The calculations suggest that, as the temperature increases, there should be a motional averaging from planar (C_{1h}) symmetry to a tetragonal (D_{2d}) centre with equivalent N sites. The predicted hyperfine tensors for the motionally averaged system are included in Table 4.6, and they do not resemble the values determined for M2, supporting the assignment of the planar, static structure to the experimental spectrum.

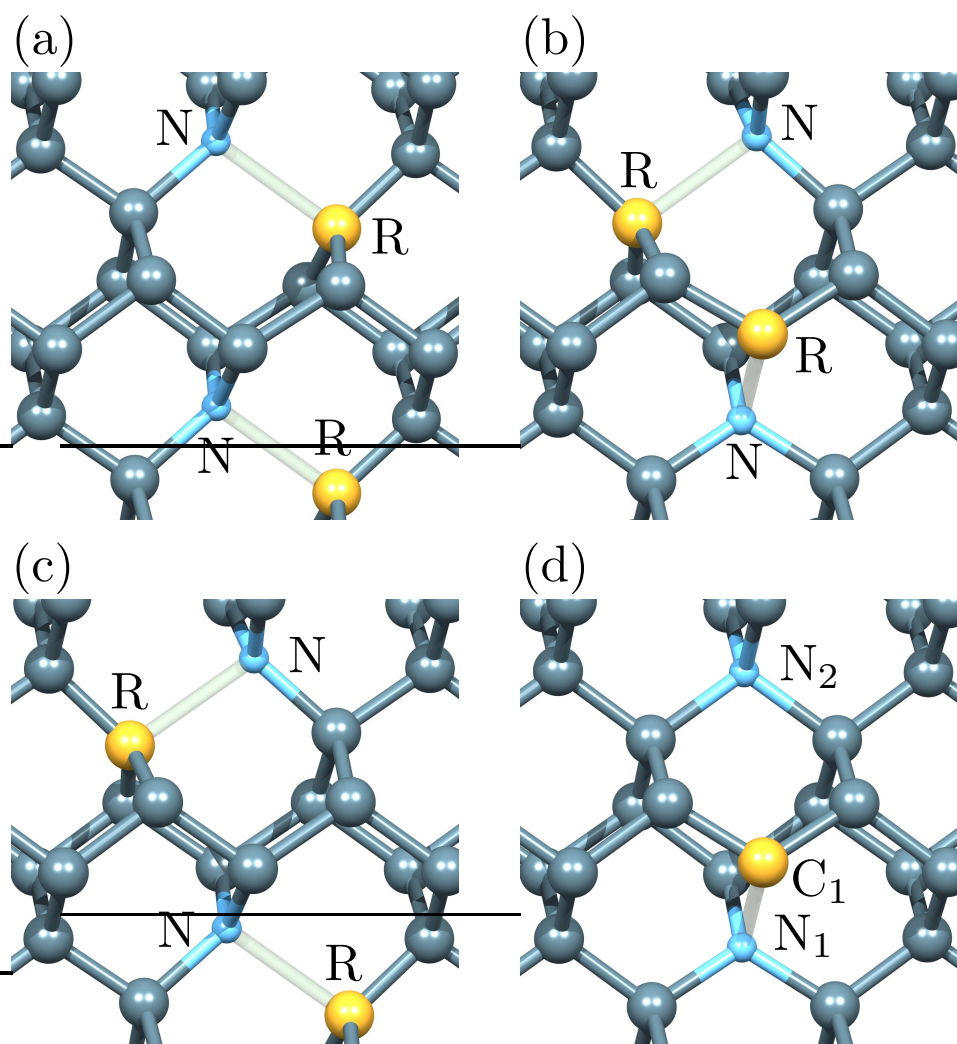


Figure 4.10: Schematics of the N₄N complex in diamond: (a) and (b) show two forms of the neutral, $S = 0$ state; in (c) the $S = 1$ configuration is assigned to NOC-2; and (d) the lowest energy structure is in the positive charge state. Structures are presented as indicated in Fig. 4.1.

4.3.5 Fifth-shell pairs and N₄

N₅N relaxes to a planar defect (C_{2h} symmetry), with the N sites separated by two reconstructed C-sites as shown in Fig. 4.13(a). This is particularly stable since the two C-radicals re-hybridise, forming a double-bond and rendering all atoms fully bonded. The central C–C bond is calculated to be 13% shorter than the diamond C–C bond length, matching the

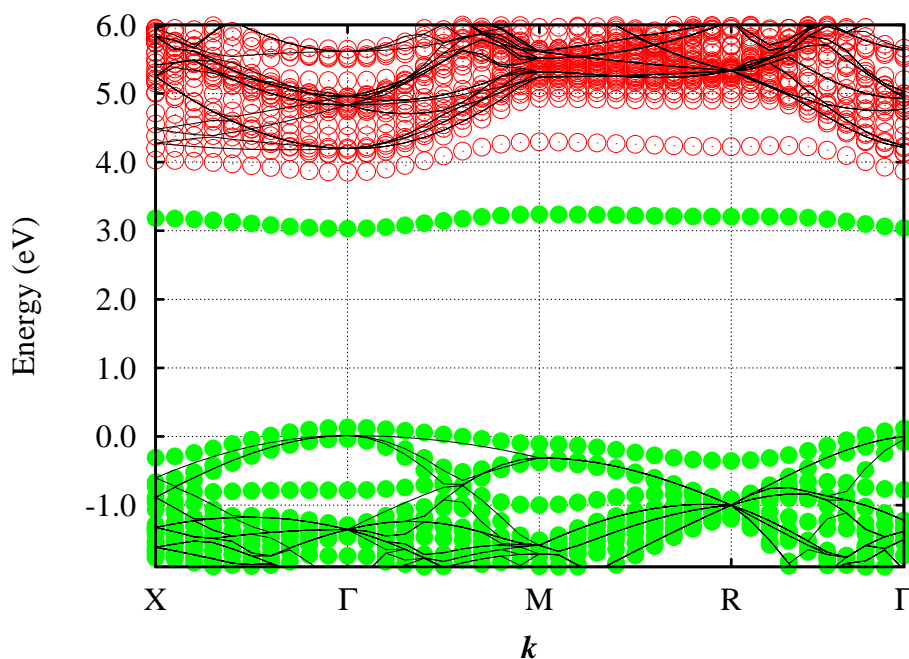


Figure 4.11: The Kohn-Sham band structure in the vicinity of the band-gap for (N4N). Symbols and scales are as indicated in Fig. 4.2.

relative C–C bond-lengths in ethene and ethane. Configurations where the carbon radicals are arranged differently are considerably higher in energy. For example, where both are perpendicular to the plane containing the N atoms, the total energy is 1.4 eV higher; such geometries are therefore discounted.

Ionisation results in a reformed C–N bond, rendering the N-atoms non-equivalent. The calculated donor level is around 0.9 eV below that of N_s^0 , lying deeper in the gap (Fig. 4.14) than for the previous cases due to the significant p_π -bond stabilisation in $(N5N)^0$.

The non-equivalence of the N atoms in $(N5N)^+$ has implications when correlating it with the N4 EPR centre, which is reported as having equivalent N atoms and no motional averaging [5]. However, the calculated reorientation barrier is very low: just 40 meV (Fig. 4.15). Therefore, even at low temperatures, $(N5N)^+$ will rapidly reorient between equivalent structures, and the observed hyperfine interactions indicating equivalent N sites represent a motional average.

This model is borne out by the calculated hyperfine interactions, as listed in Table 4.7.

Table 4.6: Calculated hyperfine tensors (MHz) for ^{14}N and ^{13}C , for the sites identified in Fig. 4.10(d). Experimental data are taken from Ref. [7]. Notation is as in Table 4.3. The orientation of the centre has been chosen to match the experimental data.

Site	A_1	A_2	A_3
Calculations (static)			
$^{14}\text{N}_1$	112 (54, 45)	75 (90, 135)	75 (36, 225)
$^{14}\text{N}_2$	13 (38, 225)	12 (128, 225)	12 (90, 135)
$^{13}\text{C}_1$	374 (55, 45)	171 (35, 225)	171 (90, 315)
Calculations (dynamic)			
^{14}N	56 (90, 45)	50 (0, 90)	44 (90, 135)
Experiment (M2)			
$^{14}\text{N}_1$	117.95 (54.7, 45)	84.48 -	84.48 -
$^{14}\text{N}_2$	7.1 (44, 225)	6.6 (134, 225)	6.6 (90, 135)

Here the A -tensors are presented as calculated for a static saddle-point structure where the N-atoms are equivalent by symmetry, and those obtained from averaging the A -tensors of $(\text{N}_s^0 \dots \text{C}-\text{C}-\text{N}_s^+)$ and $(\text{N}_s^+-\text{C}-\text{C} \dots \text{N}_s^0)$. The A -tensors for the saddle-point structure give a poor fit with experimental values, whereas the motional average is in very good agreement.

From the calculations, it seems clear that motional effects are crucial in the understanding of this centre.

Finally, it is noted that the C–C double bond in $(\text{N5N})^0$ leads to a high-frequency local vibrational mode. This is estimated to lie at 1651 cm^{-1} with A_g symmetry within the C_{2h} point group. Thus it is Raman active and infrared-inactive, but it seems unlikely that the concentration of this centre would be high enough to detect directly via the local mode.

In summary, invoking a dynamic averaging in the ionised form allows for close agreement between the $(\text{N5N})^+$ structure and the N4 EPR-centre.

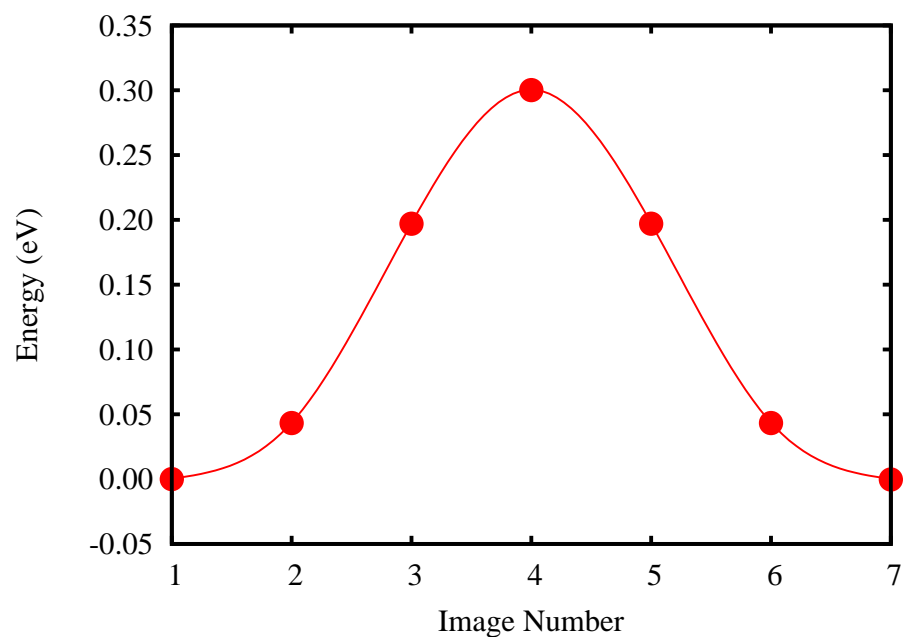


Figure 4.12: The reorientation barrier of $(N4N)^+$ between N sites.

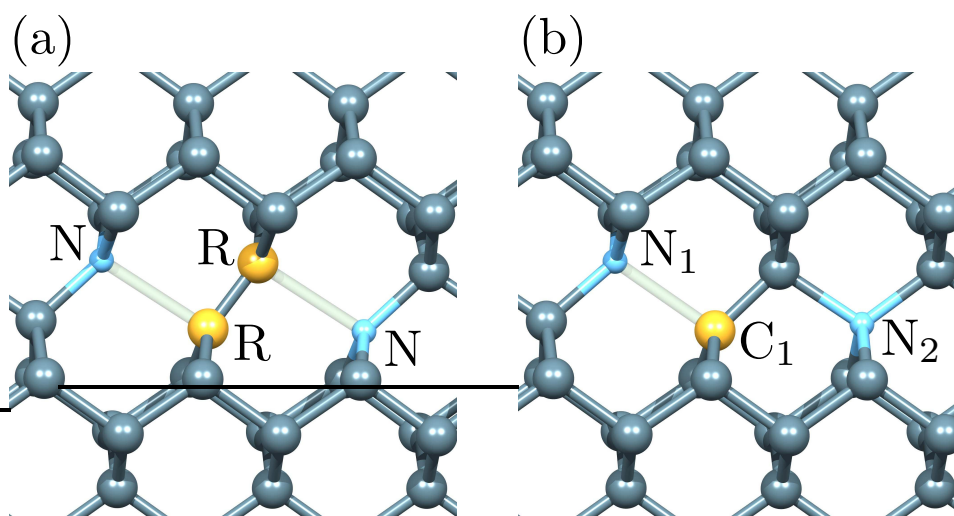


Figure 4.13: Schematics of the N5N complex in diamond in the (a) neutral and (b) positive charge states. Colours and orientation are as indicated in Fig. 4.1.

4.3.6 Sixth-shell pairs and M3

N6N cannot have equivalent N atoms since there are no point group operations that can map the N-atoms onto one-another, so that even under thermal averaging, the N atoms will

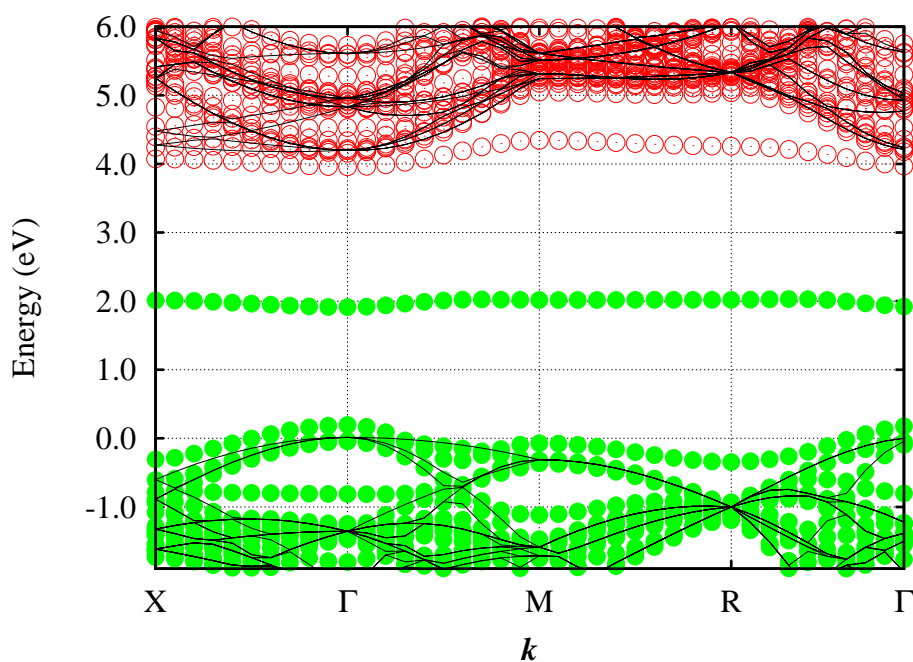


Figure 4.14: The Kohn-Sham band structure in the vicinity of the band-gap for (N5N). Symbols and scales are as indicated in Fig. 4.2.

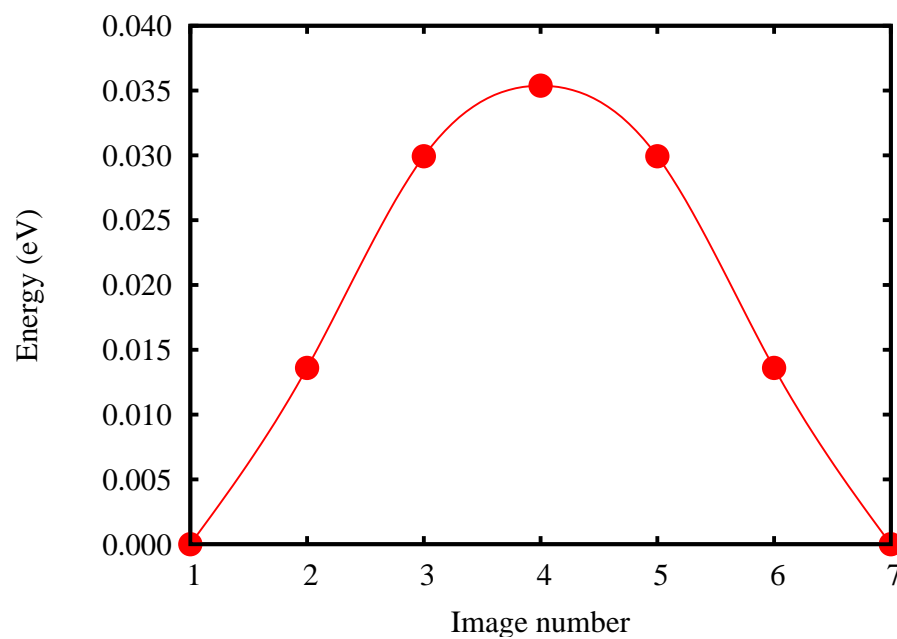


Figure 4.15: The reorientation barrier of (N5N)⁺ between N sites.

Table 4.7: Calculated hyperfine tensors (MHz) for ^{14}N and ^{13}C , for the sites identified in Fig. 4.13. Experimental data taken from Ref. [5]. Notation is as in Table 4.3.

Site	A_1		A_2		A_3	
Calculations (static)						
$^{14}\text{N}_1$	125	(125, 45)	80	(90, 315)	80	(35, 45)
$^{14}\text{N}_2$	59	(51, 225)	48	(90, 315)	48	(39, 35)
$^{13}\text{C}_1$	336	(125, 45)	159	(35, 45)	159	(90, 135)
Calculations (saddle point)						
$^{14}\text{N}_1$	114	(125, 45)	78	(90, 315)	77	(35, 45)
Calculations (dynamic)						
$^{14}\text{N}_1$	92	(54, 225)	64	(90, 315)	64	(36, 45)
$^{13}\text{C}_1$	169	(125, 45)	77	(35, 45)	75	(90, 315)
Experiment (N4)						
^{14}N	91.3	$\parallel [111]$	65.6	$\perp [111]$	65.6	$\perp [111]$

always be nonequivalent. In contrast to the N3N, N4N, and N5N centres, but in common with N2N, (N6N) 0 forms a (N $_s^-$)... (N $_s^+$) charge-transfer complex with a single dilated N–C bond, as shown in Fig. 4.16(a). This structure may be stabilised in such a form because the charge resides predominantly on the under-co-ordinated C site, which is geometrically close to the ionised N site. The preference is marginal, however, with an anti-ferromagnetic combination of N $_s^0(\uparrow)$... N $_s^0(\downarrow)$ being within 0.1 eV of the ground-state. This issue is considered in section 4.4.3.

The calculated donor level (Fig. 4.17) for N6N is just 0.1 eV below that of N $_s^0$, with the lowest energy geometry shown in Fig. 4.16(b). The M3 EPR centre has been shown to correlate [7] with this configuration of (N6N) $^+$, and Table 4.8 lists the calculated hyperfine tensors for comparison.

The barrier for the reorientation of (N6N) $^+$ to transferring the unpaired electron to the second N site (between Figs. 4.16(b) and (c)) is calculated at 0.4 eV, as shown in Fig. 4.18.

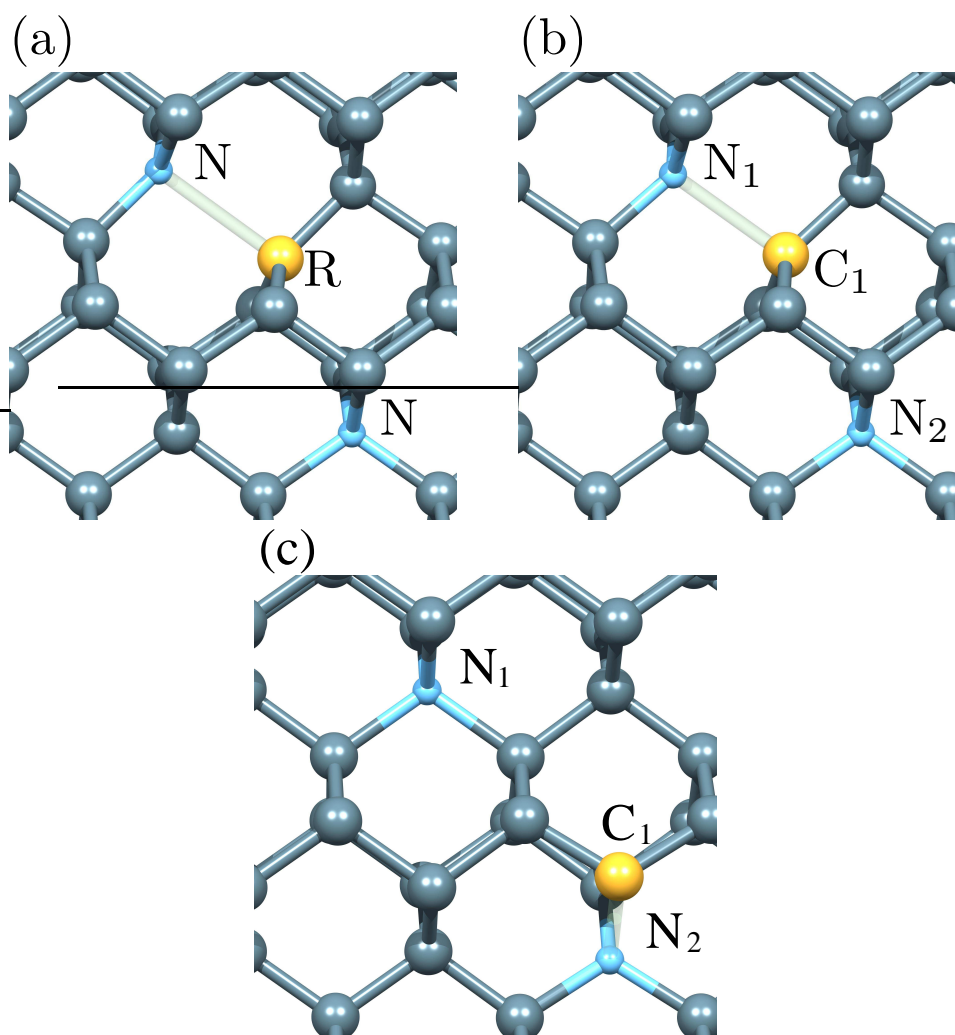


Figure 4.16: Schematics of the N₆N complex in diamond in the (a) neutral charge state; (b) and (c) show two forms of positive charge states. Colours and orientation are as indicated in Fig. 4.1.

All other orientations are found to be 0.10-0.15 eV higher in energy, so at moderate temperatures these alternative orientations would not be significantly populated, and one would expect measured hyperfine tensors to reflect the minimum energy structure.

The overall agreement between M3 and the calculations for (N₆N)⁺ is reasonable, but an assignment could not be ambiguously made based solely upon these calculations. However, it should be noted that of the six distinct structures formed by dilating single N–C bonds, the one shown in Fig. 4.16(b), which therefore has the lowest energy, yields the closest

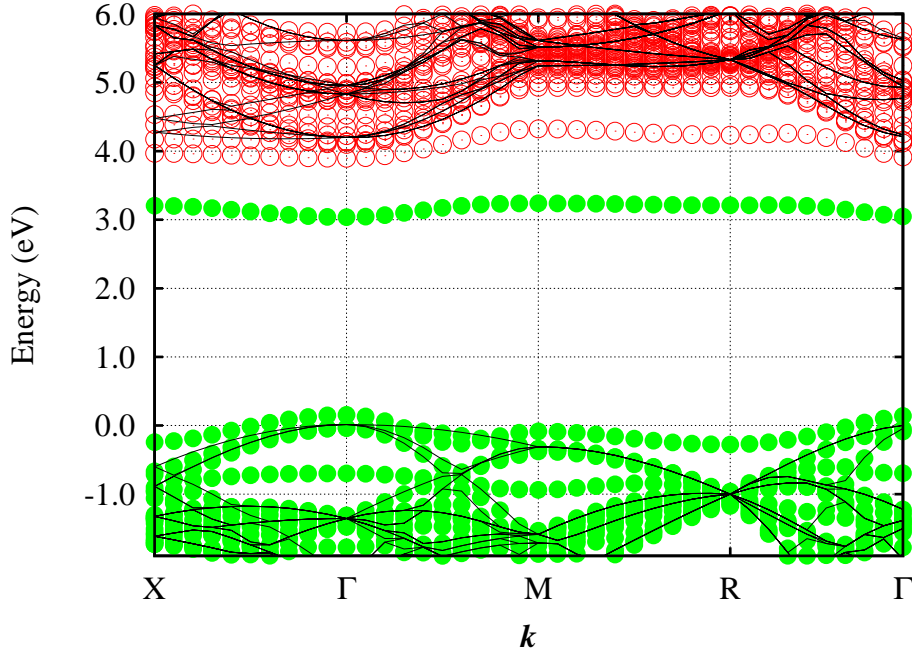


Figure 4.17: The Kohn-Sham band structure in the vicinity of the band-gap for (N6N). Symbols and scales are as indicated in Fig. 4.2.

Table 4.8: Calculated hyperfine tensors (MHz) for ^{14}N and ^{13}C , for the sites identified in Fig. 4.16(b). Experimental data are taken from Ref. [7], notation is as in Table 4.3, and the defect crystallographic orientation has been chosen to facilitate comparison with experimental values.

Site	A_1	A_2	A_3
Calculations			
$^{14}\text{N}_1$	116 (55, 45)	76 (114, 117)	76 (135, 0)
$^{14}\text{N}_2$	9 (45, 180)	10 (132, 153)	10 (76, 75)
$^{13}\text{C}_1$	385 (54, 44)	187 (114, 116)	187 (135, 0)
Experiment (M3)			
$^{14}\text{N}_1$	121.55 (54.7, 45)	85.90	85.90
$^{14}\text{N}_2$	5.1 (45, 180)	5.4 (133, 162)	6.0 (81, 81)

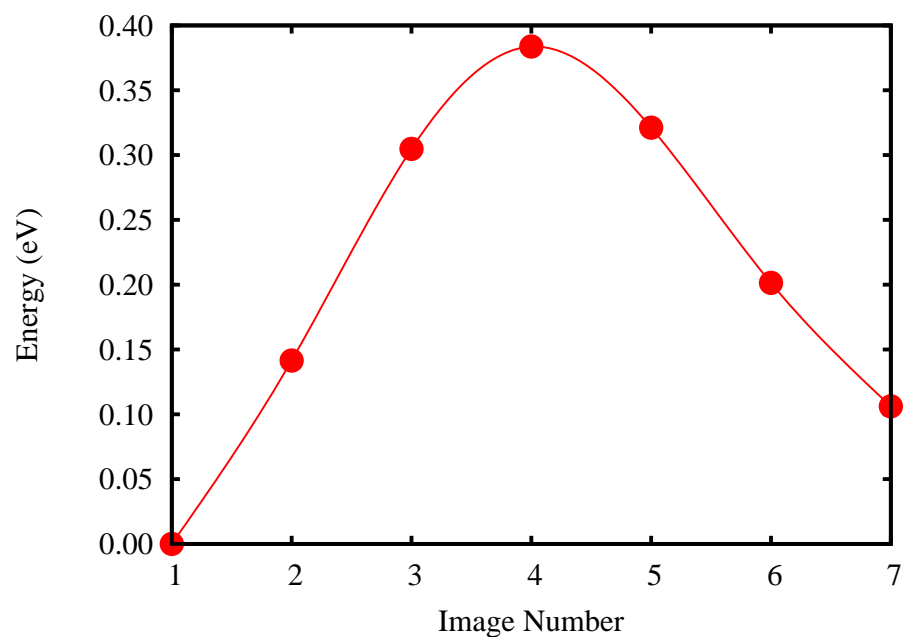


Figure 4.18: The reorientation barrier of $(N6N)^+$ between N sites.

agreement with the M3 EPR parameters. In addition, although the magnitudes calculated for the ionised N component are overestimated, the directions are in good agreement.

To conclude, although the assignment for M3 cannot be definitive, the calculations generally support the model proposed from the interpretation of experiment to a sixth-shell N-pair.

4.3.7 Seventh-shell pairs

There are two types of site in the seventh shell: one set of 4 sites along $\langle 111 \rangle$ directions, and one set of 12 along $\langle 511 \rangle$ directions. The 7a and 7b labelling of Nadolnny *et al.* [1] (Fig. 4.3) are adopted here, and the results for type N7aN are presented first.

Several combinations of P1 centres for $(N7aN)^0$ are indistinguishable within the energy tolerances of the calculations in the present research. The two lowest energy structures are shown in Figs. 4.19(a) and (b), both of which are $S = 0$ and approximately degenerate in total energy. The $S = 1$ configuration of Fig. 4.19(b) is degenerate in energy with the $S = 0$

ground state, and it may therefore be expected that this orientation should be the one seen in experimental work.

According to previous studies [1], the NOC-3 EPR centre may arise from one of two structures, and Fig. 4.19(c) shows their N7aN candidate. However, this geometry and spin state is found to be 0.1 eV above the ground state configuration in this research, and around 35 meV above the $S = 0$ form of this geometry.

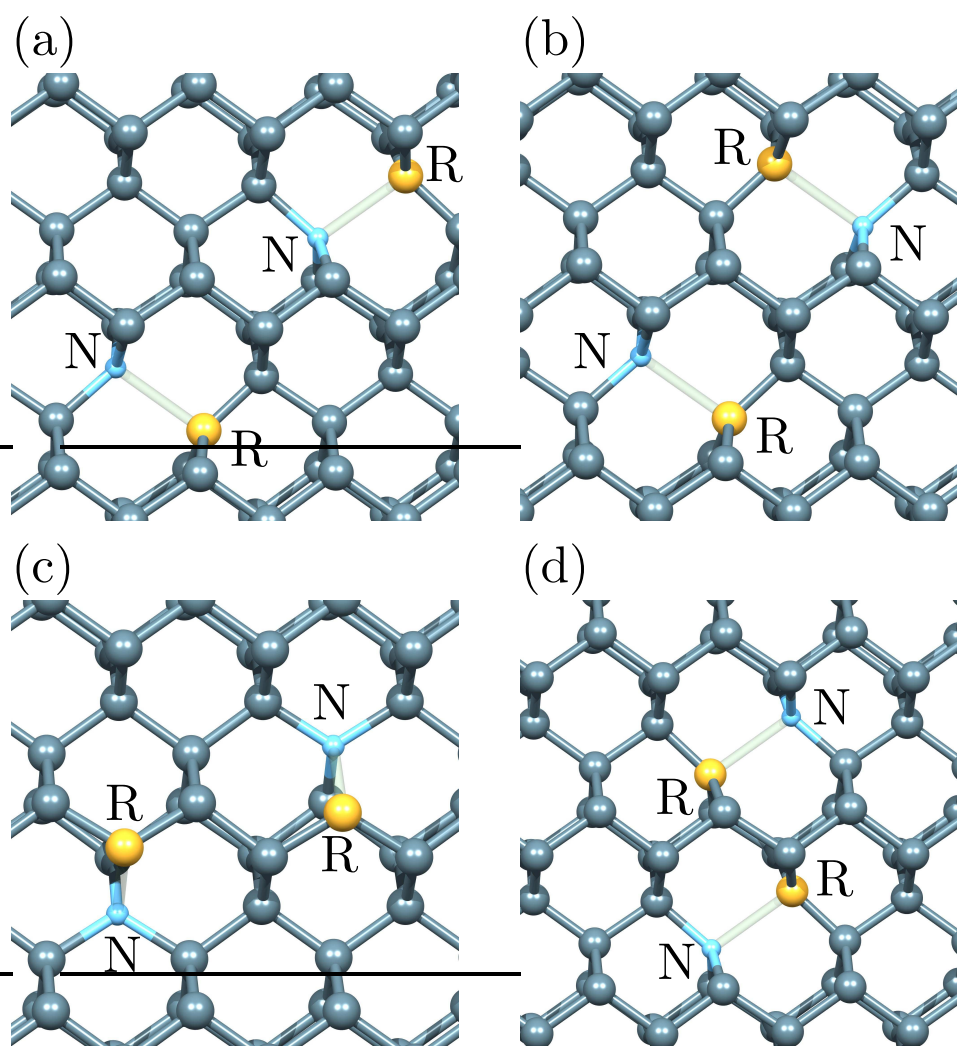


Figure 4.19: Schematics of the N7aN and N7bN complexes in diamond: (a) and (b) show two energetically degenerate forms of N7aN; with (c) being the model structure for NOC-3, and (d) shows the most stable structure for N7bN. Colours and orientation are as indicated in Fig. 4.1.

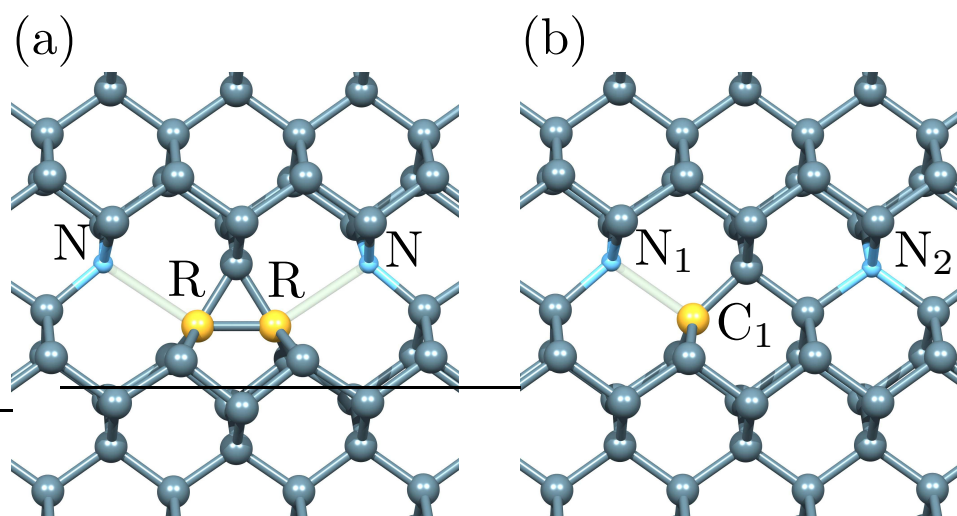


Figure 4.20: Schematics of the N8N complex in diamond in the (a) neutral and (b) positive charge states. Colours and orientation are as indicated in Fig. 4.1.

Turning to the second form of seventh neighbour pairs, the most stable N7bN structure as shown in Fig. 4.19(d) is $S = 0$ which is at least 0.1 eV more stable than any other orientation, in any spin state. The stabilisation of this particular form is most likely due to a weak bonding interaction between the parallel radical orbitals.

Since no ionised centres have been assigned to either seventh shell structure, no hyperfine data is presented for them. However, it should be briefly noted that both forms have ionisation energies close to that of isolated N_s^0 , and that in the ionised form a single broken N–C bond remains.

4.3.8 Eighth-shell pairs

The N-pair defect in the eighth shell, in common with the first and fifth shell pairs, represents a system for which all dangling bonds can be removed in the neutral, $S = 0$ state. The structure is shown schematically in Fig. 4.20(a). The three-member ring is calculated to yield a vibrational mode at around 1480 cm^{-1} , with A_1 symmetry in the C_{2v} point group. This is both infrared and Raman active but, as with N5N, it seems likely that the concentrations would be too low for direct detection of this mode.

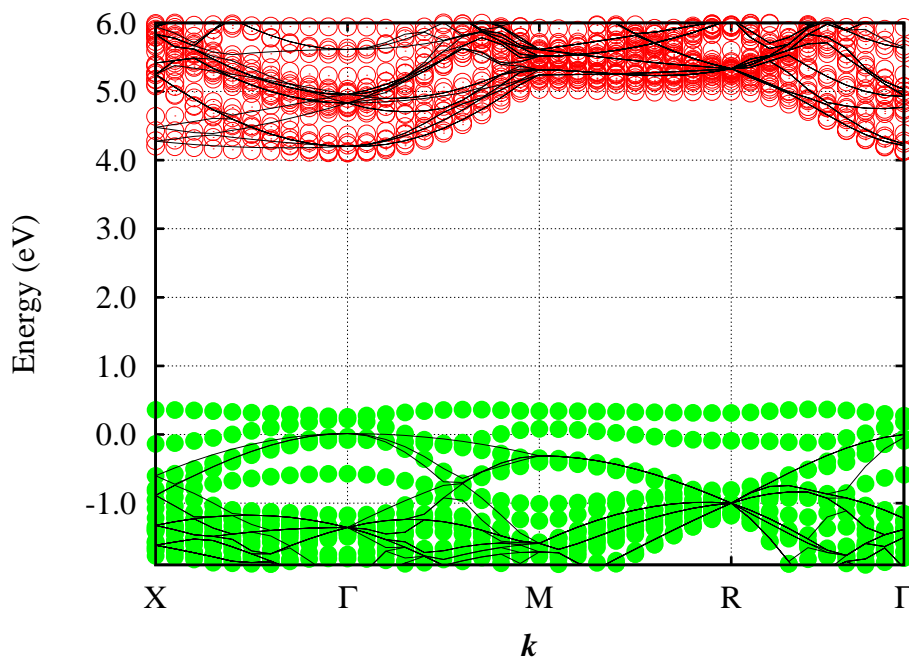


Figure 4.21: The Kohn-Sham band structure in the vicinity of the band-gap for (N8N). Symbols and scales are as indicated in Fig. 4.2.

The formation of the reconstruction yields an electronic structure close to that of the A-centre, with no deep bands in the band-gap, and filled lone-pair orbitals around the valence band top. This renders the ionisation of such a combination rather unlikely; the calculated donor level for N8N (Fig. 4.21) is at 1.3 eV deeper than N_s^0 , and just 0.6 eV higher than that calculated for the A-centre. It would therefore seem likely that, as with the ionisation of the A-centre to form W24 [73], the ionisation of N8N would be favoured only under optical excitation.

Nevertheless, Table 4.9 presents the calculated hyperfine tensors for $(N8N)^+$. The activation energy for the migration of the unpaired electron between N sites calculated using a 216-atom supercell is rather low at 0.1 eV. As such, it is possible that, if observed, this centre would present as a C_{2v} symmetry defect with equivalent N atoms. Table 4.9 also therefore includes the motionally averaged A-tensors for the N atoms and the two C atoms that form the reconstruction in the neutral charge state.

Table 4.9: Calculated hyperfine tensors (MHz) for ^{14}N and ^{13}C , for the sites identified in Fig. 4.20(b). Notation is as in Table 4.3.

Site	A_1		A_2		A_3	
Static						
$^{14}\text{N}_1$	113	(125, 45)	76	(35, 45)	76	(90, 135)
$^{14}\text{N}_2$	28	(55, 45)	25	(90, 315)	24	(35, 225)
$^{13}\text{C}_1$	376	(53, 225)	184	(90, 135)	184	(37, 45)
Dynamic						
$^{14}\text{N}_1$	69	(57, 45)	52	(33, 225)	50	(90, 315)
$^{13}\text{C}_1$	223	(51, 225)	128	(39, 45)	125	(90, 135)

4.3.9 Ninth- and tenth shell pairs: NOC-3 and NOC-1

N9N is a candidate for the NOC-3 EPR centre. Indeed, the lowest energy structure was found to be in accord with the model proposed for the $S = 1$ EPR centre shown in Fig. 4.22(a). This may suggest that the ninth-shell pairing is more favourable as a model than the seventh-shell as a model for NOC-3. However, other configurations and diamagnetic forms are within 20 meV, and it is impossible to be certain which orientation or spin state is the most stable. An assignment for NOC-3 cannot be confirmed purely on this basis.

The energies separating different orientations and spin-states in N10N are also very small, with 30 meV covering all variants examined here. In particular, the model structure proposed for NOC-1, shown in Fig. 4.22(b), is around 10 meV above what was found to be the ground state structure. On the basis of the current simulations it is therefore not possible to confirm or refute the proposition that NOC-1 has the specific form suggested in Ref. [1]. All that may be concluded is that it is plausible that such a structure might result in a paramagnetic defect.

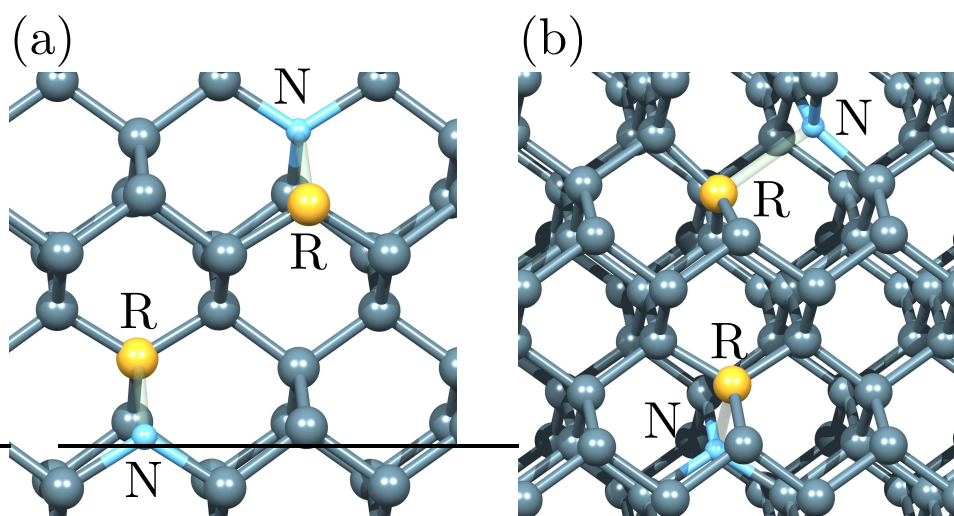


Figure 4.22: Schematics of the N9N and N10N complexes in diamond in the neutral charge state. Colours and orientation are as indicated in Fig. 4.1.

4.4 Discussion

4.4.1 Total energies

The calculated total energies as a function of increasing separation rapidly converge to a value indistinguishable from that of two isolated P1 centres. Where there is a binding energy (the energy of the pair being lower than twice the energy of a P1 centre), this reflects a chemical passivity or the re-bonding alluded to above. In particular, the total energies of N4N, N7aN, N7bN, N9N and N10N all deviate from the sum of two P1 centres by less than 0.1 eV. In line with the formation of additional bonding interactions, N1N, N2N, N3N, N5N, N6N, and N8N are bound by 3.6, 0.3, 0.3, 1.2, 0.1, and 1.4 eV respectively.

For the positively charged cases, N1N, N2N, N5N, and N8N are bound by 1.7, 0.2, 0.3, and 0.2 eV respectively, with all other structures having a binding energy less than 0.1 eV.

Finally, it is noted that, for the 2+ charge state (for which the two N atoms were uniformly found to be on-site), there is a simple Coulomb repulsion which diminishes with increasing distance. No pairs were found to be bound in the 2+ charge state.

4.4.2 Electrical activity: why are the dissociated pairs in the positive charge state?

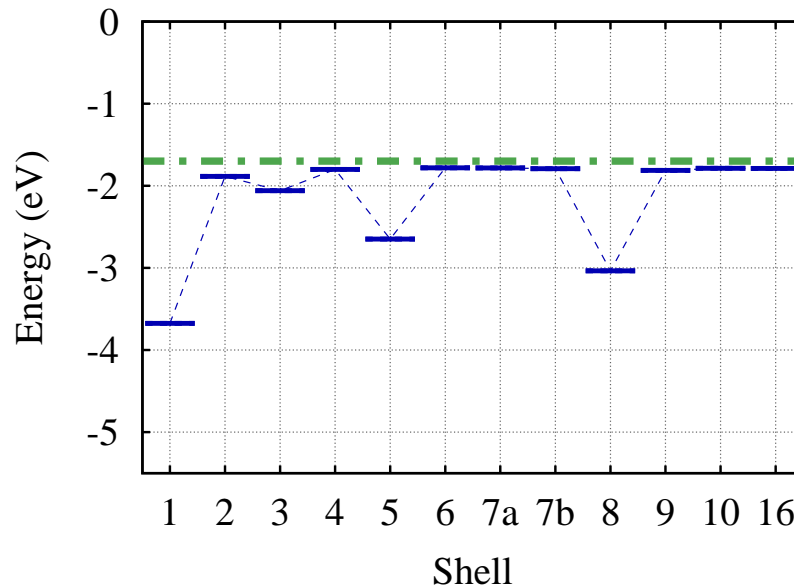


Figure 4.23: Plot of the variation of donor (blue dashed line) with shell-number. The zero of energy is fixed at E_c , and the levels plotted as the ionisation energy relative to this fixed point. The horizontal dot-dashed line at -1.7 eV shows the location of the donor level of isolated N_s^0 .

The N1, W7, N4, M2 and M3 EPR centres assigned to separated nitrogen pairs are seen in an ionised state without the need for optical excitation. This may suggest that a mechanism exists for the transfer of charge to some other site in the lattice. The types of diamond involved are generally plastically deformed, and therefore it is plausible that carbon radical sites associated with point or line defects are in proximity to the nitrogen. It has been previously shown [84] that native defects containing dangling bonds, such as vacancies and self-interstitials, give rise to rather deep acceptor levels which, in particular, are lower in the band-gap than the donor levels of N_s^0 . In addition, vacancy aggregates which have been linked to the brown colouration in this plastically deformed diamond are linked with an acceptor level in the lower half of the band-gap [85].

Fig. 4.23 shows the trend in the location of the donor level as a function of the shell-number for the N-pair using the marker method [81]. The dips in the donor levels correlate closely with the configurations which show the strongest chemical re-bonding effects, as one might expect. Indeed, for those centres where all atoms are fully coordinated in the neutral charge state, the donor levels lie relatively deep in the gap. This applies to N1N and N8N and, to a lesser extent, N3N and N5N. For other separations the donor levels lie in the upper part of the band-gap, close to that of the P1 centre, and are therefore prone to ionisation in the presence of carbon dangling bonds.

It should be noted that the large structural changes in N8N systems mean that the second ionisation level is predicted to lie *above* the first, rendering it thermodynamically unstable in the positive charge state. Thus, even if this structure is present in the material, in equilibrium it would only exist in EPR-inactive forms, but optical excitation may lead to populations of the metastable positive charge state.

4.4.3 Ferro- vs anti-ferromagnetic interactions for neutral pair

For the neutral charge state, pairs of P1-centres might be thought to interact in one of two ways: $N_s^0(\uparrow)\dots N_s^0(\downarrow)$, or $N_s^0(\uparrow)\dots N_s^0(\uparrow)$. Indeed, since diamond often favours a high-spin state, the formation of paramagnetic pairs of P1-centres may be expected to be the norm.

However, observation [1] seem to show the contrary, and the question remains as to why only three specific structures, NOC-1, NOC-2, and NOC-3, are seen in the $S = 1$ spin state.

The calculations in this study give an explanation for the absence of paramagnetic N2N, N3N, N5N, N6N, N7bN and N8N:

- For N3N, N5N and N8N there is a chemical re-bonding which strongly stabilises the $S = 0$ configuration over the $S = 1$.
- For N2N and N6N, charge exchange between the two sites yields $N_s^+ \dots N_s^-$ complexes which naturally favour the $S = 0$ configuration.
- For N7bN an exchange splitting of around 0.1 eV in favour of the $S = 0$ state is obtained, which may be traced to a very weak bonding interaction between the radical

orbitals. This is much weaker than N3N, N5N, and N8N as the sites are around 3Å apart and not on neighbouring C atoms.

This leaves N4N, N7aN, N9N, N10N and more distant combinations, matching the possible structures for the $S = 1$ EPR centres as proposed in Ref. [1]. Of these, N4N is the closest pairing which may yield a low-lying $S = 1$ state. Although it is found here that the model for NOC-2 is around 60 meV above the lowest energy structure and spin state, this is within the margin for error, and the model remains plausible. Indeed, it is worth noting that the R2, $S = 1$ EPR centre corresponding to the [001]-split self-interstitial possesses a diamagnetic ground state around 50 meV below the paramagnetic state observed experimentally [86]. This ordering is also determined using computational methods similar to those employed in this study [87]. Therefore, even if the $S = 1$ spin state is not the lowest energy configuration, it is not clear that this is inconsistent with experimental work.

For the NOC-3 models, experimentation is unable to distinguish between N7aN and N9N structures. The calculations suggest low energy $S = 1$ states for both configurations. For N7aN, the ground state structure is not that proposed for NOC-3, whereas for the N9N model structure for NOC-3 it is; although in both cases the margins of stability over other configurations are small. Therefore the simulations marginally favour a N9N structure for NOC-3, but the confidence level for such an assignment on the basis of these calculations must be low.

Indeed, the energies separating different orientations and spin states of N10N are also too small to draw any conclusions regarding NOC-1.

However, it is perhaps surprising that N7aN and N9N are not seen as separate centres, whereas N10N does seem to be: all three cases are calculated to have more than one low energy $S = 1$ configuration, and it is such a situation [1] that is the model for the average spectra labelled NOC-4.

Despite the lack of specificity in the assignment of the $S = 1$ configurations, through a combination of charge-transfer and chemical re-bonding, the calculations have accounted for the absence of many structures.

4.5 Conclusions

Density functional simulations of nitrogen pairs in diamond have largely confirmed the atomistic models proposed for N-pair defects in diamond, with three important qualifications:

- For W24, it is predicted that the hyperfine interactions on the six equivalent carbon neighbours are opposite in sign from that on the N atoms.
- For N1, a re-assignment is proposed of the hyperfine-interactions for near-by ^{13}C and the corresponding numbers of equivalent sites.
- For N4, in order to render the N-atoms equivalent, a rapid reorientation between two structures must be invoked, so that the low temperature EPR spectra are the result of a thermal, or quantum-tunnelling average of two systems where the N-atoms are nonequivalent.

In addition, values are predicted for the hyperfine-interactions at the carbon sites where the majority of the spin-density is located. Indeed, it is somewhat surprising that at N1, W7, N4, M2, and M3, this radical site has not been seen, even though in the case of N1 many other carbon sites have.

Reasons have also been determined for close-by P1 centres not combining in magnetically paired, $S = 1$ combinations. Several form chemical bonds favouring an $S = 0$ spin state, or undergo charge transfer forming $\text{N}_s^- \dots \text{N}_s^+$ pairs. Of the remaining nearby pairs, generally an anti-ferromagnetic interaction, $\text{N}_s^0(\uparrow) \dots \text{N}_s^0(\downarrow)$ is favoured, or there is a very small estimated exchange-splitting.

Finally, it is also noted that N5N and N8N species introduce high-frequency local modes through the chemical reconstructions possible in the neutral charge state, and although the concentrations may be small, this provides a potential route to the identification of N5N in the neutral analogue of N4 and a second, highly stable form of N-pairing in the N8N complex.

CHAPTER

5

Muonium and Hydrogen in Nitrogen-Aggregate containing diamond: the Mu_X centre

5.1 Introduction

In the past decade, the quality of single-crystal diamond grown from the gas phase has reached levels suitable for use in electronics [88]. However, the incorporation of hydrogen present in the growth gas leads to electrically active defects [51, 63, 89–93], and there is a need to improve the understanding of H-containing point defects in diamond.

Muonium is a pseudo-isotope of hydrogen made up from a positive muon and an electron. Muon-spin-relaxation (μSR) experiments are sensitive probes of structure, and have

been highly successful in determining the properties of H in a wide range of materials [94–98]. For pure diamond, two μ SR centres, labelled normal and anomalous muonium, relate to the tetrahedral interstitial site (Mu_T) and bond centred site (Mu_{BC}) respectively. The former exhibits an entirely isotropic hyperfine interaction (3711 ± 21 MHz), whereas Mu_{BC} is comprised of a combination of a relatively small isotropic term, and an anisotropic term along [111] ($A_s = -205.7$ MHz, $A_p = 186.9$ MHz) [95]. At low temperatures, both Mu_T and Mu_{BC} can be observed, but the relative amplitude of Mu_{BC} increases between 350 and 800 K. This is explained in terms of an activated transition from Mu_T to a thermodynamically more stable Mu_{BC} .

As described in Chapter 1, another impurity common in diamond is nitrogen. Under geological conditions or high-temperature, high-pressure laboratory annealing, nitrogen migrates and forms aggregates. Of these, nearest-neighbour pairs (A-centres) and four N-atoms surrounding a vacant site (B-centres) are particularly stable. Diamond containing aggregated N exhibits the Mu_X centre in μ SR [99], but the structure of this form has not been unambiguously identified. Mu_X exhibits less than axial symmetry, and the large, isotropic hyperfine interaction is indicative of a chemically non-bonded muonium configuration: the μ SR spectra are fitted to hyperfine parameters of $A_s = 4158 \pm 1500$ MHz and $A_p = 248 \pm 13$ MHz. Note here the large error bar for A_s .

Additional experimental studies indicate that muonium interacts with H2/H3 nitrogen-vacancy complexes [100–102] produced under gamma-irradiation of type Ia natural diamond followed by an annealing stage [103]. Theoretically, hydrogen (or muonium) in H3 represents a highly stable structure with the hydrogen atom chemically attaching to one of the two carbon radical sites [91]. In material containing H2/H3, Mu_X is suppressed and the diamagnetic fraction increased, which is interpreted as the H2/H3 centres trapping the muonium [103].

This work presents the results of density functional simulations to assess the interpretation of the experimental data in the formation of Mu_X as a complex of muonium with either an A-centre or a B-centre. Comments are also made about the interaction of muonium with H2/H3, and some alternative structures potentially significant in the identification of Mu_X

are examined.

5.2 Methodology

As was the case in Chapter 4, all calculations were carried out using AIMPRO as described in Chapter 2. The wave functions are expanded in atom-centred Gaussian basis functions with 22, 40 and 16 functions for C, N and H atoms respectively, and the charge-density fitted to plane-waves up to 300 Ha. The optimised structures for point defects are obtained by relaxing all atoms in supercells comprised from 216 host sites (simple-cubic lattice with lattice vectors of length $3a_0$). For platelet structures, supercells made up from 256 host sites in an orthorhombic configuration corresponding to lattice vectors $[220]a_0$, $[2\bar{2}0]a_0$ and $[004]a_0$, with the addition of 16 self-interstitials in the Humble form [66, 104]. To obtain total energies, the Brillouin-zone is sampled using the Monkhorst-Pack scheme [56] with a uniform mesh of $2 \times 2 \times 2$ special \mathbf{k} -points. Electrical levels are obtained by reference to a marker system [84].

5.3 Computation results

To confirm the accuracy of the computational scheme firstly the properties of muonium in the Mu_T and Mu_{BC} configurations have been analysed.

5.3.1 Muonium in diamond

It was found that the T-site is 1.25 eV higher in energy than the bond-centred site, and that the reaction $T \rightarrow BC$ is activated by 0.6 eV as shown in Fig. 5.2. These values are consistent with previous theory and experiment [95, 105].

The calculated hyperfine tensors for the two sites are listed in Table 5.1. Previous studies have suggested that vibrational motion of Mu_{BC} is important [106–108], and its impact have also been estimated. The zero-point motion average was performed by evaluation the probability of muon wave function at chosen positions when the muon is moved between

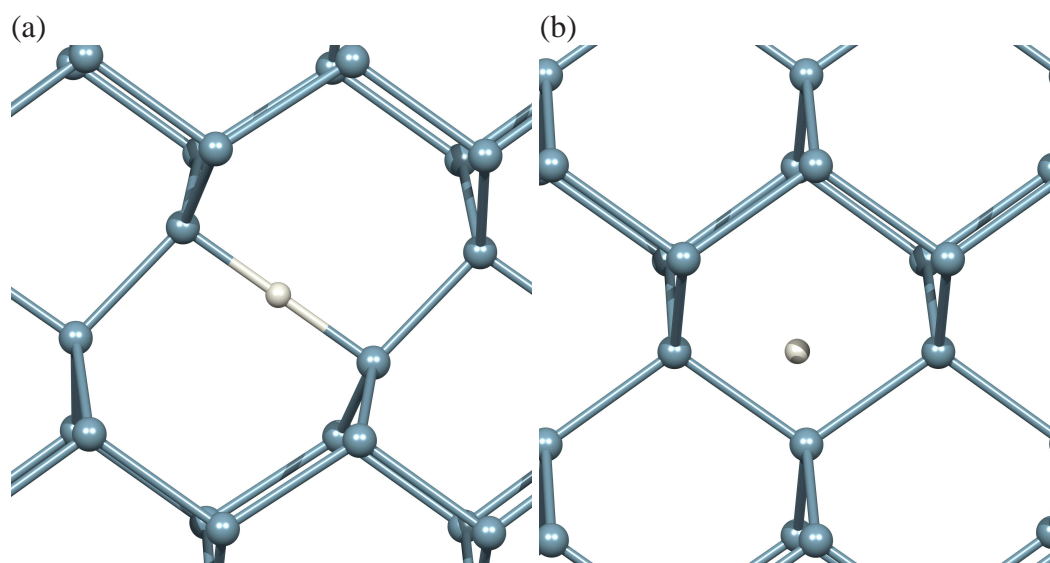


Figure 5.1: Schematics of (a) the Muonium in bond-centre (Mu_{BC}) and (b) the Muonium in tetrahedral site (Mu_{T}). Vertical and horizontal directions are approximately $[001]$ and $[110]$ respectively. Grey and white atoms are C and H/muonium, respectively.

the C-C bond and then add up the hyperfine interaction according to that. The probability was calculated by using the trapezium method. Table 5.1 shows calculated hyperfine with and without zero point motion. The resulting average reduces A_s by around 5% and the anisotropic term by less than 1%. There is an 8% overestimate in the value of A_s for Mu_{T} . However, this is somewhat mitigated if the value is considered relative to the calculated value for free muonium, which is also overestimated. If the calculated value of A_s for Mu_{T} is referred to the *calculated* value for muonium in a vacuum, rather than the experimental case, a value of $f = 0.86$ is derived, which is in closer agreement with the experiment.

Most importantly in the context of the current study, there is a clear qualitative difference between Mu_{T} , where the muonium is non-bonded, and Mu_{BC} which chemically interacts with a nearby atom. The errors between the modelling and the experiment reported in Table 5.1 are typical of hyperfine calculations [105], and the analysis of the A -tensors for Mu_{T} and Mu_{BC} is viewed as validating the present method.

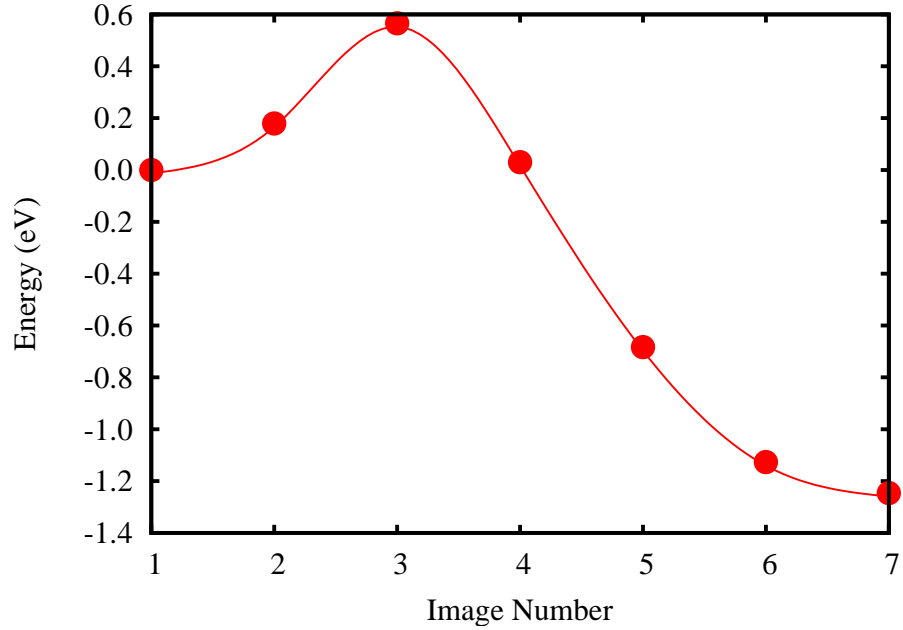


Figure 5.2: The barrier of energy between tetrahedral and bond-centred sites.

Table 5.1: Calculated hyperfine tensors of Mu_T and Mu_{BC} (MHz). f is the ratio of the isotropic hyperfine interaction for the defect to that for muonium in vacuum (4463 MHz).

	Mu_T		Mu_{BC}	
	A_s	f	A_s	A_p
This study	4000	0.90	-276	232
Zero-point motion average of this study	-	-	-260	231
Experiment [95]	3711	0.831	-205.7	186.9

5.3.2 Muonium N-aggregate complexes

Two model systems [99] for Mu_X have been simulated for complexes of muonium with an A-centre or a B-centre. The resulting optimised structures are shown schematically in Fig. 5.3. It should be noted that both A- and B-configurations are particularly stable because all atoms are chemically satisfied. The addition of muonium (or hydrogen) may therefore

be expected to result in the chemical passivity being interrupted.

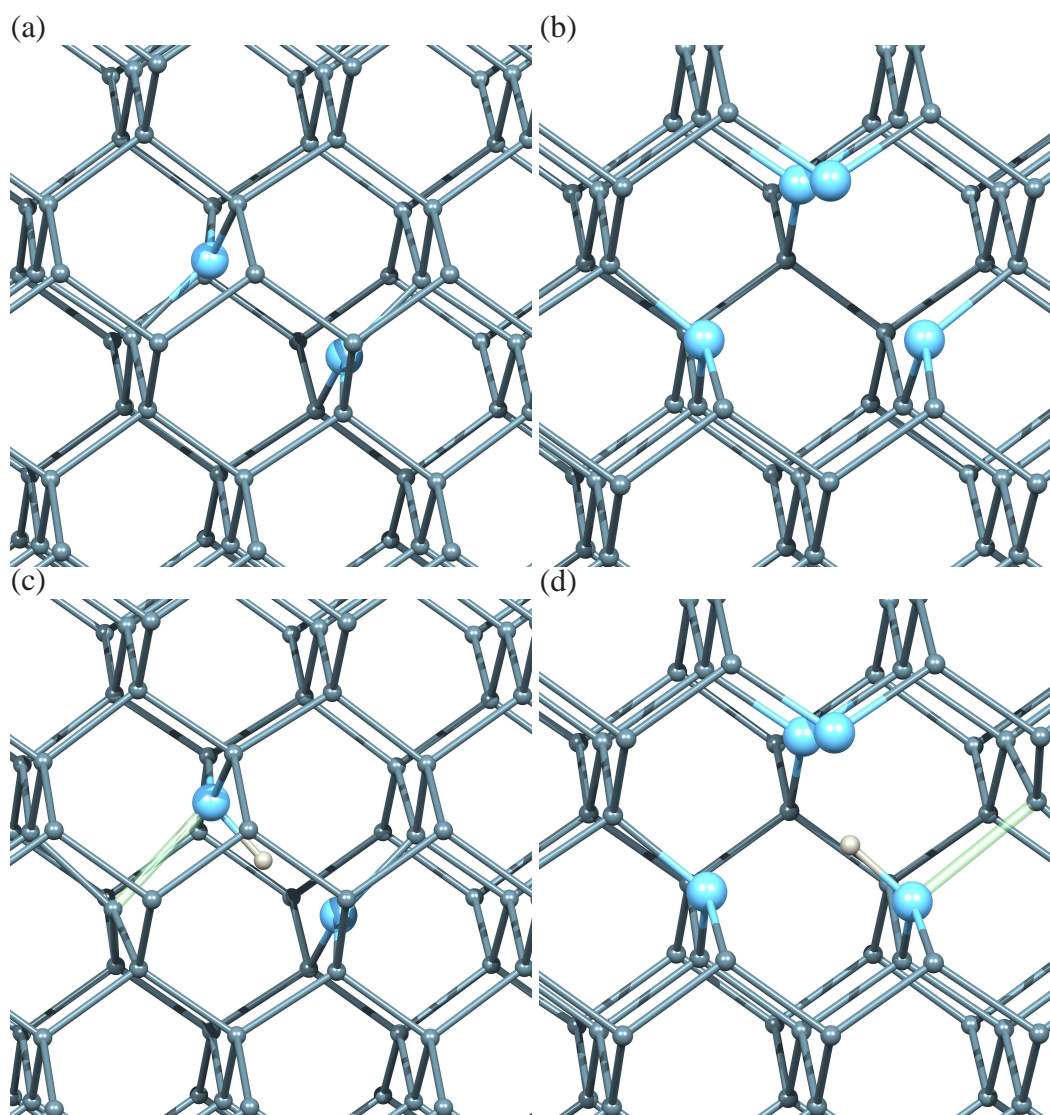


Figure 5.3: Schematics of (a) the A-centre, (b) the B-centre, (c) the A-centre–muonium complex, and (d) the B-centre–muonium complex in diamond. Vertical and horizontal directions are approximately $[001]$ and $[110]$ respectively. Small grey, large blue and white atoms are C, N and H/muonium, respectively. The transparent cylinders in (c) and (d) represent broken bonds relative to (a) and (b).

Experiments show that Mu_X has a large isotropic hyperfine interaction of the same order of magnitude as Mu_T and free muonium, accompanied by a small anisotropic term not aligned to a crystal axis. Therefore, if a complex of an A-centre or B-centre with muonium

Table 5.2: Calculated hyperfine tensors of muonium-complexes with A- and B-centres (MHz). The directions are indicate in spherical polar coordinates, θ degrees from the z - axis, and ϕ from the x -axis toward y in the xy -plane.

System	$ A_1 $	θ	ϕ	$ A_2 $	θ	ϕ	$ A_3 $	θ	ϕ
A-centre- μ	-25	90	-45	3	20	45	95	110	45
B-centre- μ	-92	90	135	-56	24	45	24	114	45

is a candidate for Mu_X , it must not have axial symmetry, and most probably will not involve a covalent bond between the muonium and any other atom.

However, this is not what was found here. In both cases, even where the muonium is initially placed in a non-bonding site in the environment of the N-aggregates, there is a *spontaneous chemical reaction* resulting in the production of a carbon radical some distance from the muon. The equilibrium structures for A-muonium and B-muonium complexes are shown in Figs. 5.3(c) and (d) respectively. Consistent with a chemical reaction, zero-temperature binding energies relative to dissociation into the N-aggregate and interstitial hydrogen/muonium are found for these complexes of 1.2 and 2.2 eV, which is also in line with the notion of N-aggregates acting as deep muonium traps in N-containing diamond [99].

The spin-density is strongly localised in the vicinity of the carbon-radical sites, leading to small, highly anisotropic hyperfine-tensors for the muon, as listed in Table 5.2. They are therefore completely inconsistent with Mu_X . To illustrate the origin of the small hyperfine interaction at the muon, a plot shows the localisation of the unpaired electron for the B-centre-muonium complex in comparison to the well known P1 EPR centre which is chemically analogous (Fig. 5.4). In the case of the P1 EPR centre, the amount of spin density on the N site is relatively small [67], and therefore the small values for the hyperfine interactions for muonium can be readily understood.

Noting that Mu_T is a metastable configuration, it is possible that muonium may locate at a metastable site within or close to an A- or B-centre. Therefore the hyperfine inter-

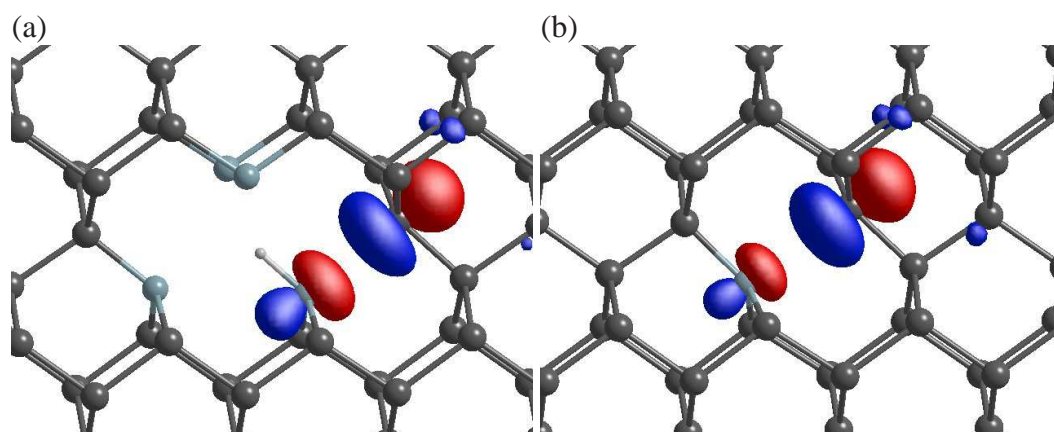


Figure 5.4: Unpaired electron Kohn-Sham functions for (a) B-centre–muonium complex and (b) neutral substitutional nitrogen (P1 EPR centre). Orientation is as in Fig. 5.3.

actions for a muonium–B-centre complex have also been obtained where the muonium is constrained to not chemically react with the lattice. In one case, the muonium is fixed by symmetry to lie at the centre of the B-centre, and in the second approximately at a T-site neighbouring the N-aggregate. Where muonium is centred in the core of the B-centre and a T_d symmetry constraint applied, there is a repulsive electrostatic interaction between the high electron density associated with the lone-pairs and that in the muonium. Consequentially the orbital containing the unpaired spin is driven up in energy relative to the case of Mu_T where there is a much lower electron-repulsion. In the present simulations the unpaired electron becomes delocalised (effectively the centre auto-ionises and the electron lies in the conduction band), resulting in a small entirely isotropic hyperfine interaction of just 86 MHz.

In contrast, for a non-bonded muonium in an interstitial cage neighbouring the B-centre, the electronic structure and localisation is practically indistinguishable from Mu_T , resulting in a calculated value of $A_s = 3962$ MHz. Similar results are obtained for muonium in the vicinity of an A-centre.

Substitutional nitrogen in diamond has a deep donor level at $E_c - 1.7$ eV [16], whereas A-centres have a donor level close to the valence band [71] and B-centres are thought to be

electrically inactive [84]. It was found that the addition of hydrogen/muonium in the A- and B-centres (in their equilibrium configurations, Fig. 5.3) produces deep donor levels. Using the donor level of substitutional N as a marker [81], the donor levels are $E_c - 0.9$ eV and $E_c - 1.1$ eV respectively for A-centre–muonium and B-centre–muonium. Note that the structural relaxation found for the A-centre–muonium centre leads to a *deep* level rather than the shallow level previously proposed [109]. However, in the previous study, the shallow level corresponded to an on-axis structure which is found here to be only meta-stable.

5.3.3 Muonium in nitrogen-vacancy complexes

The H2/H3 centre is made up from an A-centre trapping a lattice vacancy. H2 and H3 are labels for optical transitions, which are associated with the negative and neutral charge states respectively as shown schematically in Figs. 5.5 (a) and (b). The stability of hydrogen in the H3 centre has been studied theoretically [84], and recent μ SR suggests a strong muonium interaction with these centres [103]. The calculations yield a single clear minimum energy structure where hydrogen/muonium is bonded to one carbon atom to tie off a dangling bond. In the neutral charge state the unpaired spin is strongly localised on the remaining carbon radical site in the vacancy (Fig. 5.5 (c)), and as a consequence of the localisation the hyperfine tensor on the H/muon site is small: -62 MHz along $[1\bar{1}0]$, -49 MHz at 8° from $[001]$ and 90 MHz at 8° from $[110]$. In the negative charge state N_2VH (Fig. 5.5 (d)) is EPR-inactive. In agreement with the interpretation of the experiment, an H2/H3 centre would be expected to be a deep trap for muonium or hydrogen with a zero-temperature binding energy of around 6 eV for both neutral and negative charge states.

5.3.4 Muonium in other sites

Simulations of N-aggregates and muonium have all resulted in exothermic chemical reactions, leading to carbon radical sites and small, highly anisotropic hyperfine interactions with the muons.

There remains the possibility that the Mu_X centre is not associated with the N-aggregates

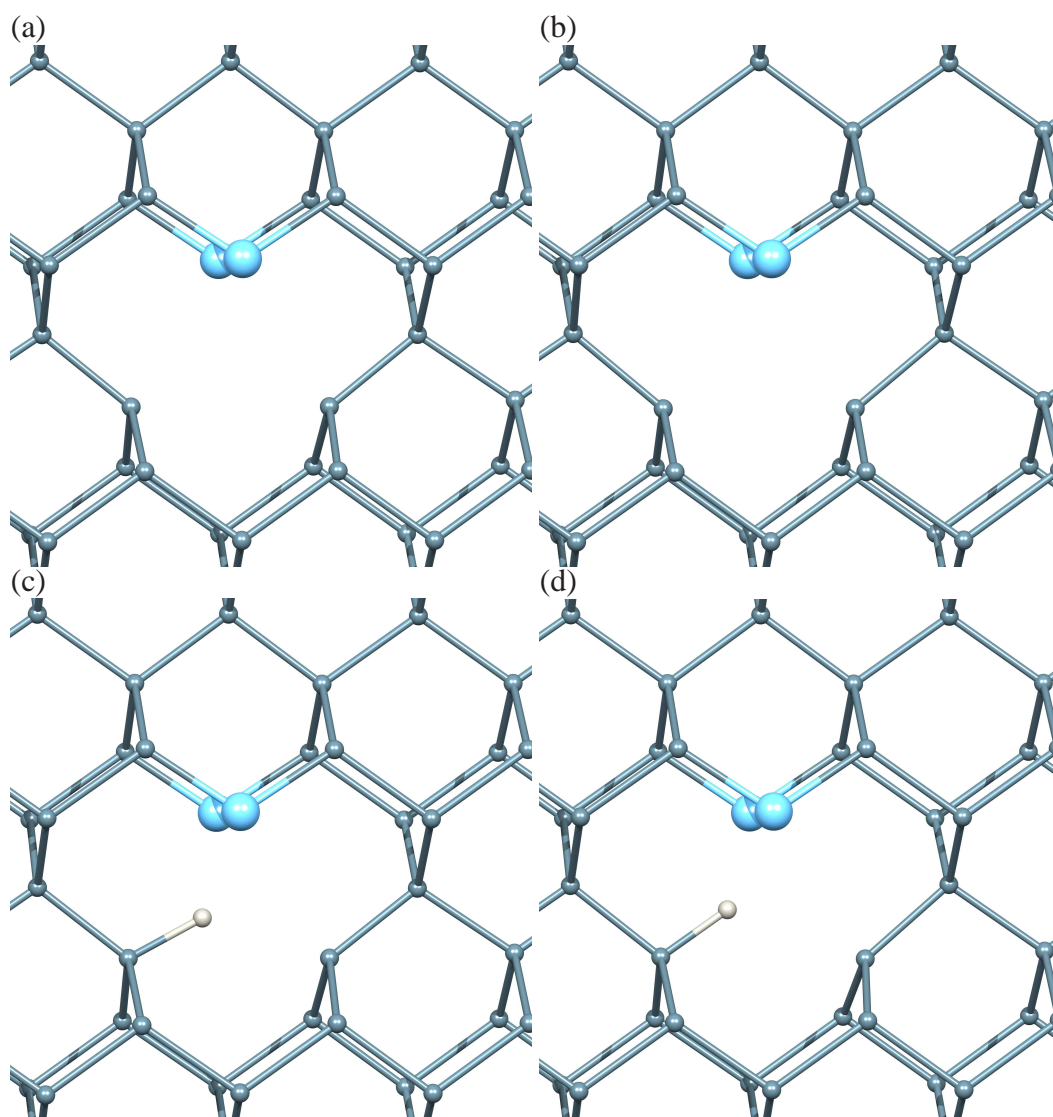


Figure 5.5: Schematics of (a) the H2-centre, (b) the H3-centre ((b) is chemically identical to (a) the only different is extra electron on (a)), (c) the H2-centre–muonium complex, and (d) the H3-centre–muonium complex in diamond. Orientation is as in Fig. 5.3.

directly. In type Ia material there are other candidate structures. In particular, such diamonds also contain nano-cavities (aggregates of lattice vacancies) and platelets thought to be made up from planar self-interstitial aggregates [66, 104, 110]. Both have open regions that may trap the mobile muonium, and this would result in large isotropic components to the hyperfine-interaction, consistent with the measured values for Mu_X .

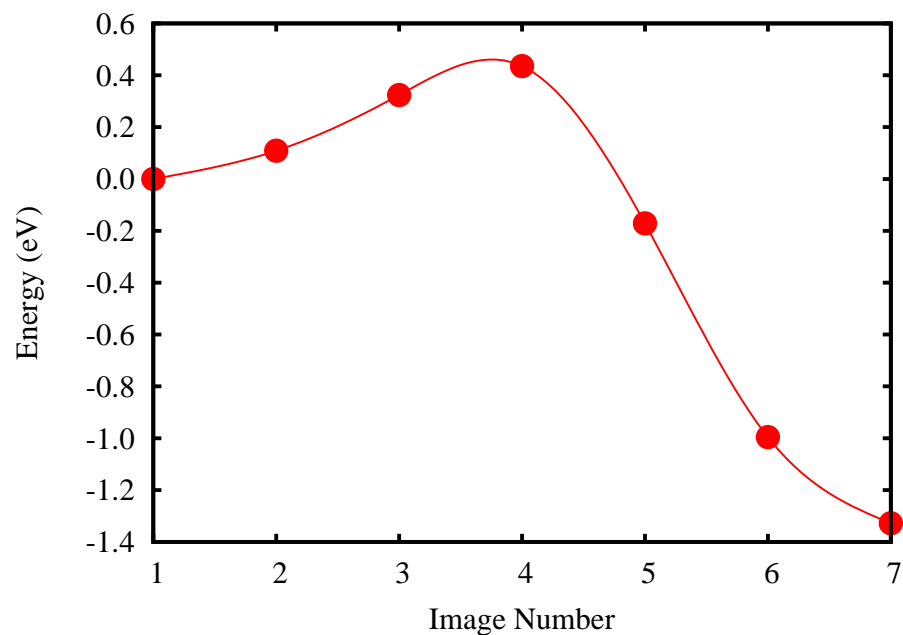


Figure 5.6: The barrier of energy for chemical reaction between the muonium and the lattice in a V_2N_6 cavity.

To simulate nano-cavities one, two, five and eight carbon atoms in symmetric arrangements were removed. The remaining under-coordinated carbon sites are replaced by nitrogen to produce a chemically passive void in the diamond lattice. The question specifically addressed here is not whether or not these specific voids are responsible for Mu_X , but to assess how large a cavity might need to be to achieve an isotropic component of the hyperfine-tensor on the muonium as large as that observed in experiment. The values for the hyperfine-tensors where the muonium is fixed at the centre of the voids are listed in Table 5.3. It should be noted that the theoretical ratio, of isotropic terms, f' , for a di-vacancy gives the best agreement with the experimental ratio, f , for Mu_X , and larger voids result in muonium indistinguishable, at least in the present calculations, from free muonium.

The stability of these non-bonded structures requires some discussion. Hydrogen/muonium in a V_2N_6 cavity has many metastable configurations, including the non-bonded case, and several chemically reacted forms have similar structures to that seen for the B-centre (Figs. 5.3(d) and 5.4(a)). It was noted above that the reactions of hydrogen/muonium with the A- and

B-centres are spontaneous; that is, there is no barrier. In the case of the larger N-terminated cavities the situation is closer to that for Mu_T , and a barrier exists for a chemical reaction between the muonium and the lattice (Fig. 5.6). For V_2N_6 this activation energy is calculated to be 0.4 eV, and the reaction is exothermic by 1.2 eV. The chemically reacted forms all have hyperfine interactions at the muonium site which are small and highly anisotropic.

Table 5.3: Calculated hyperfine tensors for muonium in a range of model cavities (MHz). f and f' are ratios of A_s to the experimental and calculated values for free muonium respectively. The experimental values for Mu_X are shown for comparison.

Model cavity	A_s	f	f'	A_p
V_1N_4	86	0.02	0.02	0
V_2N_6	4388	0.98	0.94	-12
V_5N_{12}	4650	1.04	1.00	0
V_8N_{18}	4695	1.05	1.01	1
Mu_X	4158	0.93	-	248

Perhaps a more favourable option for the site of Mu_X would be the self-interstitial platelet, as this has a reasonably regular structure that may be expected to yield a non-axial tensor. Fig. 5.7 shows four characteristic structures, where the combinations of five, six and eight member rings are generated by the planar agglomeration of tetra-interstitials [66, 104]. The lowest energy is found where muonium forms a three-centre bond between two carbon atoms that make up a next-neighbour reconstruction in the pure carbon platelet (Fig. 5.7(a)). The unpaired electron is highly localised and yields a muon hyperfine tensor more characteristic of Mu_{BC} than of Mu_X (see Table 5.4).

However, in a form reminiscent of Mu_T there is a metastable configuration where muonium resides in the open channel produced by the platelet, as shown in Fig. 5.7(b). The hyperfine tensor for this structure is much closer in nature to Mu_X . However, the stability of this site is marginal, and it tends to react with neighbouring carbon to form an anti-bonding

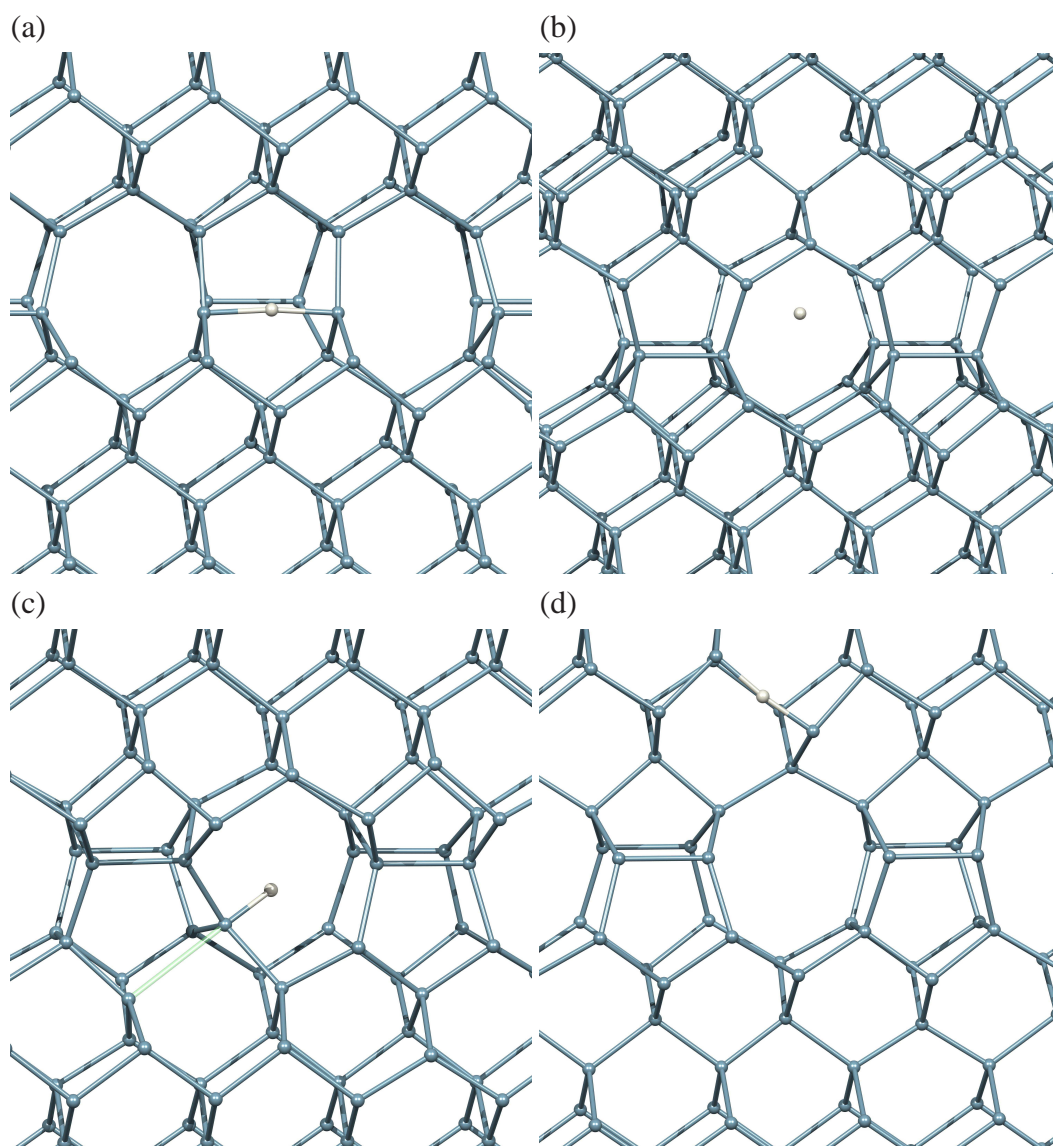


Figure 5.7: Schematics showing selected structures of muonium in the platelet defect. The grey and white atoms are carbon and muonium, respectively. Vertical and horizontal directions are approximately $[001]$ and $[110]$ respectively.

configuration close in energy, shown in Fig. 5.7(c), which does not yield agreement with the hyperfine interactions of Mu_X .

However, the zero-point motion of a muonium species in the channel is expected to be appreciably large. The difference in zero-point energy between chemically bonded and non-bonded muonium in diamond has been estimated to be of the order of 0.2-0.3 eV, com-

Table 5.4: Calculated hyperfine tensors for muonium in a model platelet, (MHz), for the structures presented in Fig. 5.7.

Structure	A_s	A_p	Principal direction
(a)	-289	157	[110]
(b)	4594	1	[001]
(c)	367	5	[111]
(d)	-278	230	[11 $\bar{1}$]

parable to the energy difference between configurations (b) and (c). If, when vibrational terms are included, the non-bonded form is more stable than (c), then it is possible that the Mu_X centre is associated with non-bonded muonium in platelets. In real diamonds, platelet structures are disordered, with nitrogen incorporated, and the amount of relaxation is affected by the platelet size [111–114]. This variability in sites within the platelet may relate to the uncertainty in the isotropic component of the hyperfine interaction reported for Mu_X .

Finally, it is noted that there are many other metastable structures for muonium chemically incorporated into the platelet. All of these structures introduce deep electrical levels similar to bond-centred hydrogen, and hyperfine tensors close to Mu_{BC} . In addition, the energy for the case where the muonium is sited just outside of the platelet core (Fig. 5.7(d)) is 2.3 eV higher than the lowest energy state found here within the structure, showing how the platelets represent trapping sites for hydrogen or muonium.

5.4 Discussion and conclusions

The small, anisotropic hyperfine-tensors for the ground-state configurations of complexes of muonium with A- and B-centres mean that these centres are most probably not responsible for Mu_X . However, this interpretation must be viewed in the context of a number of issues.

First it has been suggested that some of the error in the estimate of the hyperfine-tensor for anomalous muonium arises from the zero-point motion of the very light muon along the

axis of the C–C bond [106–108]. Could zero-point motion for either of the complexes result in agreement with the Mu_X parameters? This may be viewed as unlikely, since even in the case of Mu_{BC} the effect of including motional averaging is a small perturbation, whereas for either the A-centre–muonium or B-centre–muonium complexes the isotropic term must increase by two orders of magnitude to match the measured values of Mu_X .

A second possibility is that Mu_X results from muonium in a region not directly within the N-aggregates, but in an approximately tetrahedral cage in the immediate vicinity of them. However, as indicated in section 5.3, the perturbation to the hyperfine-tensors of Mu_T even in the T-sites immediately adjacent to the A- and B-centres is very small. Coupled with the small binding energies in these chemically unreacted sites and barrier-less reactions to form carbon radicals, it is not clear how near-by structures might be responsible for Mu_X . However, this remains a possibility given the large uncertainty in the experimental parameters.

A final possibility is that muonium is tunnelling rapidly between sites around the N-aggregates. Indeed, such effects are thought to be present in the case of muonium in Zn-doped GaAs [115], but if this were the case in N-containing diamond, it is not obvious why the resulting hyperfine-tensor would be non-axial given the high symmetry of the two nitrogen aggregates involved.

If Mu_X is not associated directly with A- or B-centres, then a possible explanation is that Mu_X relates to different centres also present in type Ia diamond. Small voids yield hyperfine-tensors close to muonium in vacuum, and possess barriers to chemical reactions. However, it is unclear how the anisotropic component in such a model can be explained, and there is relatively little evidence for small, chemically passive voids. In contrast, the evidence for the presence and structure of platelets in Ia diamond containing B-centres is quite clear. Based upon the present calculations, a possible configuration for muonium within the open channels of the platelets also has some merit, but again the identification of the anisotropic term may be problematic.

In summary, although none of the models examined for Mu_X is a particularly good fit, the calculations show that a simple configuration made up from an A-centre–muonium or

B-centre–muonium complex is unlikely to be responsible. To further investigate a potential role for the platelet, it would be beneficial to explore the presence of Mu_X in material containing only A-centres. If a direct interaction is taking place between muonium and A- and/or B-centres, a centre with a small, isotropic hyperfine interaction with the muon, would be expected to see.

CHAPTER

6

Nitrogen-Oxygen Pairs in Diamond: the N3 and OK1 EPR Centres

6.1 Introduction

In isolated substitutional form, nitrogen is a deep donor [16] due to a strong chemical re-bonding effect resulting in a dilated N–C ‘bond’, and it is possibly also an acceptor [84, 116]. N_3^+ forms a tetrahedral structure with four equivalent carbon neighbours [117]. N_3^0 is associated with an unpaired electron, and this centre is responsible for the well known P1 electron paramagnetic resonance (EPR) centre [67]. Although nitrogen doped diamond is of little value as an electrical conductor, it is of considerable interest for quantum-computing [18].

Although combustion may indicate high levels of oxygen in natural diamond [118],

there is little evidence for oxygen dispersed in the diamond lattice. A small number of optical centres may be related to oxygen [119, 120], and there is speculation regarding oxygen defects from EPR [121]. Unlike with nitrogen, the naturally abundant isotopes of oxygen have no nuclear spin, and therefore are difficult to identify directly. ^{17}O , which has a natural abundance of around 0.04%, *does* have a nuclear spin and ion implantation of this isotope into diamond films has been performed [122]. However, the centres observed after implantation are dominated by lattice damage where the oxygen may be trapped, and these do not represent likely structures for oxygen in equilibrium. Of the EPR centres described in this implantation study, a thermally stable centre labelled KUL12 is thought to exhibit ^{17}O hyperfine interactions at an axially symmetric centre with $A_{\parallel} = -362$ MHz and $A_{\perp} = -315$ MHz.

The most detailed data for oxygen defects comes from atomistic simulations. On-site substitutional oxygen (O_s) yields two defect-related energy gap-states: an a_1 -state lying in the mid-band-gap and a t_2 -state close to the conduction band [123, 124]. An on-site structure is metastable [124], with reconstructions to either divalent or trivalent oxygen being favoured. For example, O_s ($S = 1$) and O_s^- favour just two C-O bonds [124]. O_s is theoretically electrically active, with donor and acceptor levels at $E_c - 2.8$ eV and $E_c - 1.9$ eV, respectively [124]. Since the acceptor level lies below the donor level of N_s , in material containing both types of centre one would expect charge transfer to occur.

Amongst the many tentative assignments for EPR centres to oxygen containing defects [121], the two centres labelled N3 (not to be confused with the optical centre labelled N3 [125]) and OK1 have been suggested to contain O_s in association with N_s , with clear evidence for nitrogen from the hyperfine interactions with ^{14}N [126, 127], and possible correlation with oxygen content [128]. At low temperatures both are planar (C_s symmetry), but N3 is trigonal at 550 °C, which is interpreted in terms of motional averaging between three symmetrically equivalent planar geometries.

One model for N3 is a nearest neighbour N_s - O_s pair [8]. However, at least two other models have been proposed: nitrogen neighbouring a di-vacancy [121], and N_s neighbouring substitutional titanium [11]. OK1 has been assigned [9, 126, 129] to the atomic arrange-

ment N–C–O (*i.e.* where substitutional N and substitutional O are separated by a single host site), to substitutional nitrogen next to a lattice vacancy [127], a N–V–O complex [9, 121] or to substitutional N bordering a Ti-vacancy complex [11].

Previously it has been shown [130] that N–O pairs favour a nearest neighbour configuration, being bound by 3.9 eV with respect to separated substitutional centres. Nearest neighbour N–O pairs were also analysed by Lowther [131], but in that study the structure seems to be axially symmetric and no analysis was provided for the assignment to the N3 EPR centre. It has also previously been found that the second-neighbour pair is around 3 eV less stable than when the N and O impurities are adjacent, possibly casting doubt on the assignment of such a configuration to OK1. In this chapter the results of density functional simulations are presented for the two N–O pair models for EPR centres in diamond, and their hyperfine tensors in comparison to the alternatives suggested in the literature for the N3 and OK1 centres are critically assessed.

6.2 Methodology

All calculations were carried out as described in chapter 2. The charge-density was fitted to plane-waves up to 300 Ha. C, O, N and Ti are treated using fixed linear-combinations of *s*- and *p*-orbitals of four widths. One (four) set(s) of *d*-Gaussians are included for C and O (N and Ti) to accommodate polarisation. Generally 216-atom, simple-cubic supercells of side length $3a_0$ are used, except for the calculation of reorientation barriers using climbing nudged elastic bands [59, 60], where cubic unit cells of side length $2a_0$ are used due to computational cost. Electrical levels are estimated by calculating the formation energies of different charge states and determining the critical values of the electron chemical potential [81].

6.3 Computation results

The analysis of the models for the N3 EPR centre are first presented, followed in section 6.3.2 by those for OK1.

6.3.1 The N3 EPR centre

N3 is an $S = 1/2$ EPR centre [8, 127, 132] commonly observed with other N-containing centres. It has C_s symmetry at room temperature and C_{3v} at 550°C. A small nitrogen hyperfine interaction suggests that the spin density is localised mostly some distance from the N atom, and in particular is much smaller than that of N_s^0 [132]. An absence of any other resolved hyperfine interactions points to other impurities involved, if any, possessing zero nuclear spin. Thus, an N_s-O_s model has several points in its favour. First, the minute natural abundance of ^{17}O , the only radio-stable isotope with a non-zero nuclear spin, is consistent with the absence of resolved hyperfine interactions at this site. Secondly, divalent oxygen is consistent with a planar symmetry; and thirdly the location of oxygen could motionally average to axial at elevated temperatures [8].

The proposed C_s -symmetry structure is shown in Fig. 6.1(a). When the N and O are constrained to lie on a common $\langle 111 \rangle$ axis (C_{3v} symmetry) the energy is 0.5 eV higher. This is consistent with the low temperature symmetry and motional averaging observed. It is noted that the bond-lengths of the *constrained* structure are in good agreement with the published data [131], suggesting that the analysis presented in that study may relate to this high energy structure.

The electronic structure of the complex is a simple combination of the constituent parts. The band structure for the planar geometry shows an occupied band close to the valence band top, chiefly made up from the N_s lone-pair, and a partially filled band around mid-gap, mainly associated with the single carbon radical site. The states deep in the gap render the N_s-O_s both an acceptor and donor; the $(-/0)$ and $(0/+)$ levels are placed at $E_v + 3.7$ eV and $E_v + 1.5$ eV respectively. Critically, the acceptor level lies close to but *above* the donor level of N_s , consistent with such a centre being in the paramagnetic, neutral charge state in

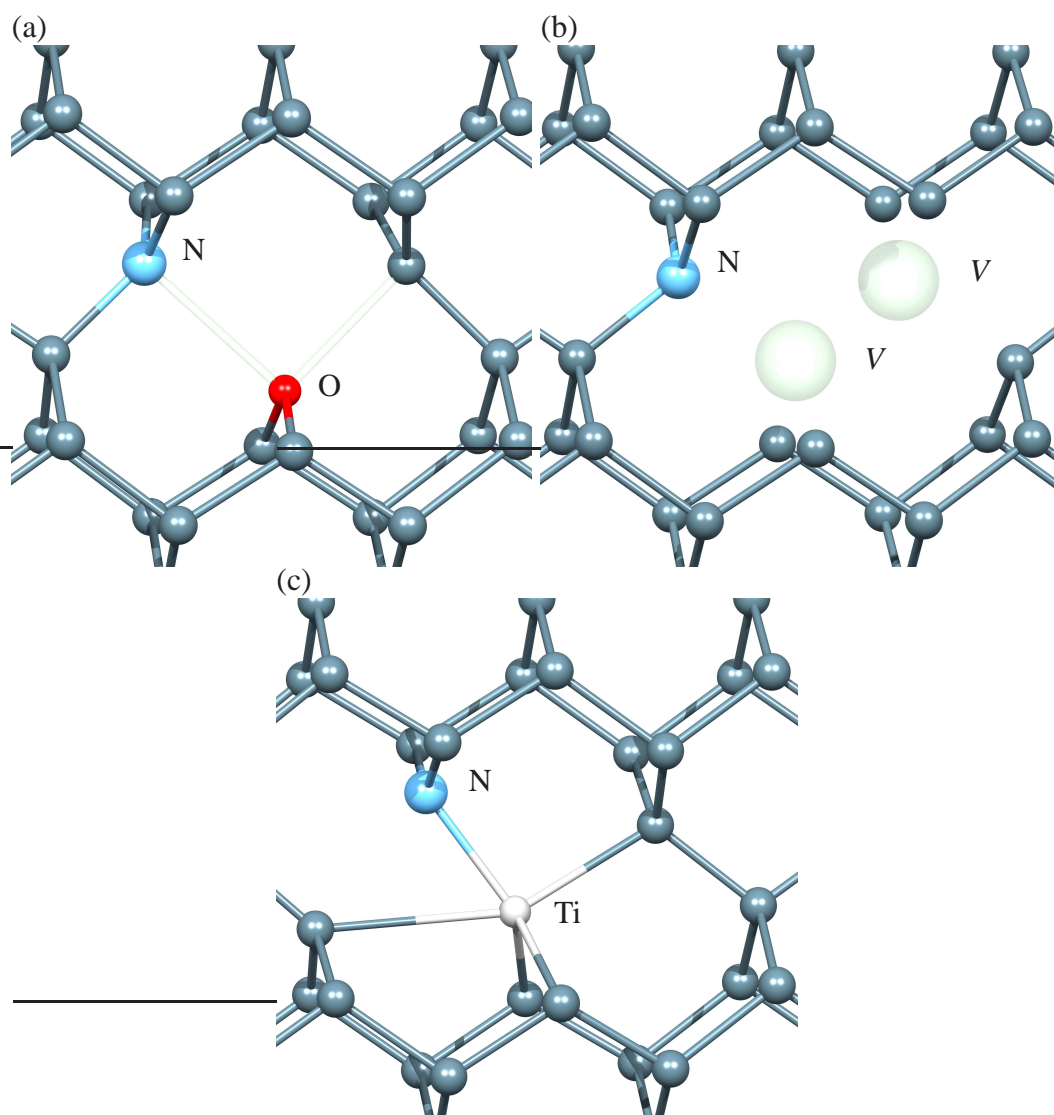


Figure 6.1: Schematics of three structures proposed for the N3 EPR centre in diamond: (a) N_s-O_s , (b) NV_2 and (c) N_s-Ti_s . Vertical and horizontal directions are approximately $[001]$ and $[110]$ respectively. Impurities are as labelled with V indicating vacant sites.

material containing N_s donors.

The calculated hyperfine tensors are also in reasonable agreement with experimental values (Table 6.1): the calculated value of 27° from $\langle 110 \rangle$ agrees with the experimental value within the quoted error bars for the measured value. The hyperfine interactions for ^{17}O are also reported, although to-date there is no experimental data with which to compare

them.

The next question concerns the motional averaging at 550 °C. The barrier to reorientation of 0.45 eV was obtained, via a slightly off-axis route. Classical reorientation rates, ν , are governed by three key parameters: temperature, T , activation energy, E^a , and attempt frequency, ν_0 , such that:

$$\nu = \nu_0 \exp(-E^a/k_B T).$$

At 550 °C, the exponential term is 2×10^{-3} , so for reasonable values of ν_0 [61] one would expect axial symmetry at this temperature, consistent with observation. At room temperature, N3 has planar symmetry. However, the exponential term in the reorientation rate at 300 K is 3×10^{-8} , so based upon the Vineyard theory of attempt frequency, one might still expect a trigonal symmetry, and so some doubt is raised regarding this assignment. However, combining the energetics from previous studies [130] with the hyperfine and reorientation data, it is concluded here that the calculations are broadly consistent with the assignment of N3 to an N_s-O_s pair, subject to the uncertainty in the temperature at which motionally averaged axial symmetry should occur.

Given the qualified agreement between the N_s-O_s model and experiment, the alternative structures proposed for N3 must now be considered. Since N-hyperfine is observed, any model must contain nitrogen. One model, as shown in Fig. 6.1(b), is a nitrogen–divacancy complex (NV_2) [121]. Here an electronic structure was found which much more complex than N_s-O_s , with the five carbon-radicals combining to produce several occupied and unoccupied bands in the lower half of the band-gap. By examining various charge states, an acceptor level is found at $E_v + 1.8$ eV, with $(NV_2)^-$ having a spin-triplet ground state, 0.4 eV below the spin-singlet. The acceptor level in the lower half of the band-gap means that it is likely to be negatively charged in material containing N-donors.

A possibility remains that NV_2 is in the -2 charge state, which is predicted to be $S = 1/2$ in line with the N3 centre, although the spin-quartet configuration lies just 0.1 eV higher in energy. The second acceptor level is predicted to lie around $E_v + 2.4$ eV, so in N_s containing material this charge state is plausible. Although a $(NV_2)^{2-}$ may have the correct effective spin for N3, a decisive objection to this model is that there is no obvious mechanism for the

Table 6.1: Hyperfine tensors for ^{14}N , ^{17}O and ^{47}Ti based upon the models for the N3 centre depicted in Fig. 6.1. In each case the magnitude (MHz) precedes the spherical-polar angles θ and ϕ in parentheses, where θ is relative to [001], and ϕ is measured from [100] toward [010] in the xy -plane. θ' is the magnitude of the angle A makes with $\langle 110 \rangle$ within the mirror plane. Experimental values are taken from Ref. [8]. (s) and (d) indicate the values for static and dynamically reorientating geometries respectively, as described in the text.

Site	A_1	A_2	A_3	θ'
N _s -O _s , Fig. 6.1(a)				
N (s)	5.0 (117,45)	3.5 (90,135)	3.6 (153,225)	27°
O (s)	-233.2 (127,225)	-185.9 (143,45)	-185.2 (90,315)	
N (d)	5.0 (125,45)	3.5 (90,135)	3.5 (35,45)	35°
O (d)	-190.6 (125,45)	-207.8 (90,135)	-207.8 (35,45)	
(NV ₂) ⁰ , $S = 1/2$, Fig. 6.1(b)				
N	-1.0 (67,45)	-1.4 (92,315)	-1.5 (157,45)	23°
(NV ₂) ¹⁻ , $S = 1$ Fig. 6.1(b)				
N	0.0 (90,315)	0.1 (31,45)	0.8 (121,45)	31°
(NV ₂) ²⁻ , $S = 1/2$ Fig. 6.1(b)				
N	3.8 (90,315)	4.1 (10,45)	5.1 (100,45)	10°
(NV ₂) ²⁻ , $S = 3/2$, Fig. 6.1(b)				
N	-0.5 (90,135)	-0.5 (145,226)	0.3 (125,45)	35°
Ti _s -N _s , $S = 1/2$ Fig. 6.1(c)				
N (s)	134.2 (49,45)	81.2 (41,225)	80.9 (90,315)	41°
Ti (s)	-4.9 (59,45)	-0.6 (31,225)	2.9 (90,135)	
N (d)	84.0 (125,45)	106.3 (35,45)	106.3 (90,135)	35°
Ti (d)	1.3 (55,225)	-0.7 (35,45)	-0.7 (90,135)	
N3 (Experimental data)				
N (s)	4.28	3.12	3.12	26° ± 3°
N (d)	4.4	3.8	3.8	35.2°

conversion from planar to axial symmetry at 550 °C.

Nevertheless, given the structural similarity between this model for N3 and a later one for OK1, the calculated hyperfine tensors for NV₂ complex are presented in Table 6.1. They are in very poor agreement with N3, and exclude it as a viable model on both symmetry and hyperfine tensor grounds.

Finally, a recent proposal is that N3 is a nearest neighbour substitutional Ti (Ti_s) and N_s pair [11, 12], as shown schematically in Fig. 6.1(c). The evidence for the presence of Ti comes mainly from x-ray phase analysis which shows that diamonds exhibiting N3 are correlated with the presence of TiO₂ [11, 12]. In order for the Ti_s-N_s model to proceed, it is first necessary for the ground state structure to have planar symmetry, which is what is found here; the relaxed structure is three-fold co-ordinated N_s⁰ neighbouring on-site Ti_s. The reorientation, which would lead to axial symmetry at sufficiently high temperatures, is found to be activated by 0.9 eV, broadly consistent with the planar symmetry at room temperature, and the axial symmetry at 550 °C of N3. However, the calculated hyperfine tensors (Table 6.1), reflect the localisation of the spin-density close to the N-site and magnitudes closer to P1 than N3. The agreement between the Ti_s-N_s model and experimental values is very poor.

In summary, of the models proposed in the literature for the N3 EPR centre, only N_s-O_s is consistent with experiment, and even in this case the reorientation barrier may be viewed as being rather low for a convincing assignment. Regrettably, a definitive model is not possible with the currently available experimental data.

6.3.2 The OK1 EPR centre

OK1 is commonly seen along with N3 [8], and there are at least four proposed models. One closely resembles the N_s-O_s model for N3, but where the N and O are separated by a host site (N_s-C-O_s). Several *metastable* structures are found here, based upon the relative positions of dilated N-C and O-C bonds, of which one structure proposed [9, 126, 129] for OK1 is shown in Fig. 6.2(b). This has the required planar symmetry, and as the N atom is on-site it can be viewed as being ionised (N_s⁺). The oxygen is in a divalent co-ordination

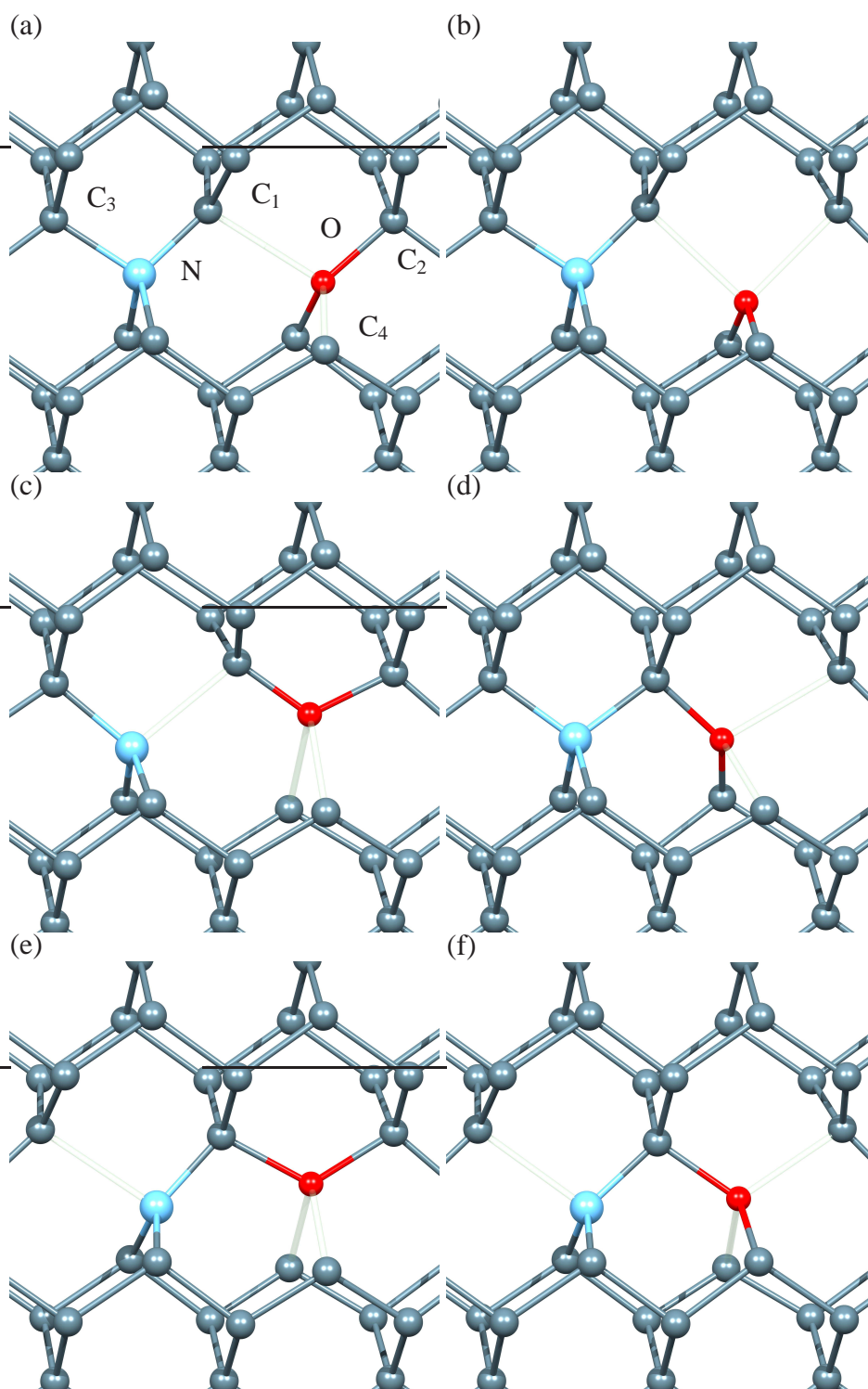


Figure 6.2: Schematic of N_s-C-O_s complexes. Vertical and horizontal directions are approximately $[001]$ and $[110]$ respectively. In each case the impurity on the left is N and that on the right is O. The inter-nuclear interactions best described as broken bonds are shown as transparent sticks, and covalent bonds as solid sticks.

with two carbon neighbours, leaving two carbon sites unsaturated.

However, structure (b) is not the lowest in energy, albeit by a small margin. Structure (a) is a different orientation chemically equivalent to structure (b) and is more stable by around 70 meV. A third analogous structure, shown in Fig. 6.2(d), is 0.55 eV higher in energy than the ground state. In principle another planar configuration with oxygen bonded to C-atoms in the plane containing the two impurities could also be formed. However, it is found that under these bonding conditions the substitutional N is in the neutral charge state, generating a dilated N–C bond, as shown in Figs. 6.2(c) and (e), being 0.28 and 0.70 eV higher in energy respectively than the ground state structure.

As with the nearest-neighbour pairing, the N-C-O complex is found to be both a donor and acceptor with levels located at $E_v + 1.7$ eV and $E_v + 3.8$ eV respectively, so the most probable charge state in N-containing diamond is neutral.

The hyperfine parameters and relative energies for the N-C-O structural configurations are listed in Table 6.2, but none of the static structures is a good fit to the observed ^{14}N hyperfine interactions for OK1.

No motional averaging has been Experimentally observed up to at least 600 °C [9], so another criterion that a model for OK1 must satisfy is that motional averaging must not change the symmetry from planar up to such temperatures.

For the N-C-O structure, the reorientation found between (a) and the symmetrically equivalent structure obtained by reflection in the $(1\bar{1}0)$ plane is activated by just 0.4 eV, as is the reorientation between structures (a) and (b). Although averaging between these three geometries would result in a planar defect consistent with OK1, the simulated hyperfine interactions averaged over (a) and (b) are not in agreement with OK1 (see Table 6.2). Indeed, to obtain a ^{14}N hyperfine of sufficient magnitude it is necessary to mix in configurations such as (c), where the N site is effectively in the neutral charge state (Table 6.2, average over (a)–(c)). Including such structures is contrary to their relative total energies, and therefore it is concluded unlikely that a motional averaging of low-energy N-C-O structures is responsible for OK1.

Based upon ^{13}C hyperfine data, Hill *et al.* [10] offered a revised structure for OK1 with

Table 6.2: Calculated relative energies (E^{rel} , eV) of ^{14}N hyperfine tensors (MHz) for structures in Fig. 6.2. In each case, θ and ϕ are given as indicated in Table 6.1, θ' indicates the directions of A_{\parallel} with $\langle 110 \rangle$ for axially symmetric tensors. Experimental parameters for ^{14}N in OK1 are taken from ref. [9]. Where a range of structures is indicated, the corresponding hyperfine tensors represent an average over these geometries. For averages involving (a), both the form shown and its symmetric equivalent reflected in the $(1\bar{1}0)$ plane are included.

	E^{rel}	A_1	A_2	A_3	θ'
(a)	0.00	-1.2 (86,21)	-1.6 (84,111)	-1.7 (173,79)	-
(b)	0.07	-2.0 (121,225)	-2.5 (90,315)	-2.6 (149,45)	-
(c)	0.28	-89.8 (126,225)	-63.1 (90,315)	-62.9 (144,45)	36°
(d)	0.55	8.6 (116,184)	8.3 (85,96)	08.1 (153,16)	-
(e)	0.70	76.7 (123,45)	45.8 (90,315)	45.7 (33,45)	33°
(f)	0.70	86.9 (122,45)	56.4 (104,305)	56.1 (36,15)	32°
----- Motional averages -----					
(a)–(a)	-1.3	(94,225)	-1.5 (90,135)	-1.7 (4,225)	-
(a)–(b)	-1.5	(75,45)	-1.9 (90,135)	-2.0 (165,45)	-
(a)–(c)	-23.6	(127,225)	-17.2 (90,135)	-17.2 (127,225)	37°
Experiment	21.66		15.48	15.19	25°

the under-co-ordinated oxygen atoms out of the mirror plane along the lines of Fig. 6.2(e). The calculated A -tensors for these sites are listed in Table 6.3. Again, no single structure yields quantitative agreement with the observed values of OK1. Averaging the low-energy structures, (a) and (b), yields superficial agreement, but since the corresponding values for ^{14}N are very poor, it is concluded that the balance of evidence is that the N-C-O model for OK1 is probably incorrect. Nevertheless, noting that the ^{17}O hyperfine interactions in N-C-O complexes are rather large, the A -tensors for the structures in Fig. 6.2 are listed in

Table 6.3: Calculated hyperfine tensors of ^{13}C in N-C-O complexes as shown in Fig. 6.2 (MHz). θ and ϕ are given as indicated in Table 6.1, θ' indicates the directions of A_{\parallel} with [001] for axially symmetric tensors. Experimental values are from Ref. [10].

	Site	A_1	A_2	A_3
(a)	C_1	65.1 (127,43)	34.4 (103,304)	34.1 (40,18)
(a)	C_4	383.7 (125,314)	167.4 (94,46)	167.4 (35,322)
(b)	C_1	60.7 (127,45)	31.7 (37,45)	31.5 (90,315)
(b)	C_2	386.1 (126,225)	168.1 (144,45)	168.1 (90,135)
(c)	C_1	-362.8 (137,225)	-189.4 (90,135)	-182.0 (47,225)
(c)	C_4	383.1 (126,136)	171.0 (143,305)	170.2 (85,222)
(e)	C_4	8.1 (117,113)	5.2 (97,20)	4.9 (153,276)
(e)	C_3	399.8 (125,45)	183.9 (90,315)	183.7 (35,45)
(a)–(a)	C_4	193.5 (125,314)	83.7 (37,334)	83.4 (100,50)
(a)–(b)	C_4	128.6 (125,314)	56.4 (38,342)	55.1 (104,53)
(a)–(c)	C_4	192.3 (125,314)	85.1 (38,338)	84.0 (102,52)
Experiment				
	Ref. [10]	127 (129,141)	74 (139,306)	74 (97,45)
	Ref. [11]	122.87 -	73.37 -	73.37 -

Table 6.4 in order to allow future comparison with experimental data, should ^{17}O enriched doping be achieved.

Alternative models for OK1 must now be considered. One such model is the nitrogen–vacancy [127]. However this model can be easily discounted on the simple grounds that this structure is identified with other experimental spectra, as pointed out previously [11].

The next OK1-model to be examined is made up of a Ti–vacancy complex decorated by a nitrogen atom [11], as shown schematically in Fig. 6.3(a). One advantage of this model is the rather simple way in which the structure agrees with the observed symmetry, since

Table 6.4: Calculated ^{17}O hyperfine tensors (MHz) for structures in Fig. 6.2, as specified in Table 6.2.

	A_1		A_2		A_3	
(a)	-139.7	(130,326)	-90.7	(73,251)	-87.0	(45,359)
(b)	-137.7	(114,225)	-87.3	(156,45)	-83.6	(90,315)
(c)	-295.0	(90,135)	-274.1	(178,210)	-239.1	(92,45)
(d)	9.0	(45,87)	44.6	(90,177)	54.3	(45,267)
(e)	-4.9	(34,225)	0.2	(56,45)	0.9	(86,315)
(f)	3.3	(122,127)	46.0	(135,359)	81.9	(61,57)
(a)–(a)	-91.0	(74,45)	-112.3	(17,225)	-119.4	(92,315)
(a)–(b)	-102.7	(50,225)	-107.5	(84,135)	-107.8	(41,45)
(a)–(c)	-154.4	(89,135)	-148.3	(168,225)	-138.0	(102,45)

the N atom is locked in a substitutional location and any reorientation of the defect cannot easily be allowed.

However, the calculated hyperfine interactions for this centre are in very poor agreement with the observations (Table 6.5) for all three chemical species. The reason for the small interaction on the N site, and the relatively large magnitude on the Ti, is rather simple. The unpaired electron density is mostly distributed over the Ti and its five carbon neighbours. The trivalent nitrogen atom is fully bonded, and the only source of spin density at this site is due to polarisation of the valence states by the nearby unpaired electron, as seen in the ^{14}N hyperfine tensors in the NV_2 centre (see Table 6.1).

Based upon the calculated hyperfine values, it is concluded that the Ti–V–N model is probably not correct for OK1. Perhaps more problematic than the hyperfine tensors is a predicted acceptor level at $E_v + 1.6$ eV, which means that Ti–V–N would be expected to be in the EPR inactive $(\text{Ti-V-N})^-$, $S = 0$ state in material containing N-donors.

If the assignment to Ti is correct, then there are many other configurations containing both Ti and N that would be consistent with OK1, at least at the level of structural symme-

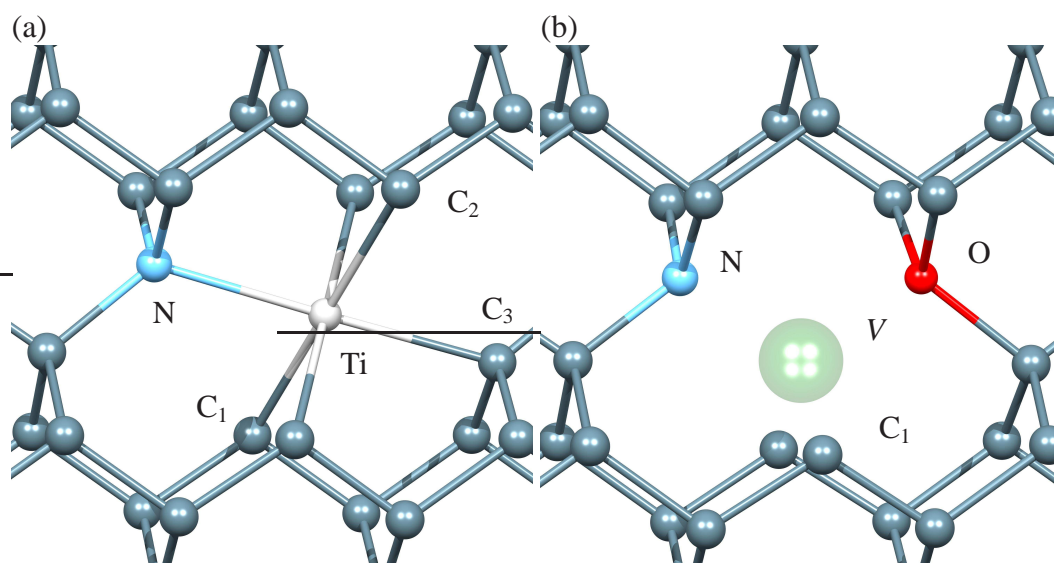


Figure 6.3: Schematics of models proposed for OK1: (a) the $\text{Ti}_s\text{-V-N}_s$ and (b) $\text{N}_s\text{-V-O}_s$ complex. Vertical and horizontal directions are approximately $[001]$ and $[110]$ respectively.

try. The structure and hyperfine interactions for Ti, C and N in $\text{Ti}_s\text{-C-N}_s$ (second-neighbour substitutional pair) and complexes made up from interstitial Ti in the vicinity of substitutional N have all been analysed. However, in all the structures examined, the spin density generates hyperfine interactions at the Ti site that are too high.

The final model [9] studied here is an N-V-O complex. The ground state structure found is shown in Fig. 6.3(b). The oxygen and nitrogen both adopt three-fold co-ordinated sites, suggesting that the oxygen is ionised. Indeed, this is the structure found for the simple oxygen-vacancy complex [124]. Therefore the carbon sp^3 dangling bonds are occupied by three electrons.

As was the case for the Ti-V-N complex, this leads to a small hyperfine interaction at the N-site in comparison with OK1, as listed in Table 6.5. The possibility of a charged NVO complex was also examined. The carbon radical sites render the complex both a donor and acceptor, with the calculated donor and acceptor levels at $E_v + 1.1$ eV and $E_v + 2.4$ eV respectively. In material containing nitrogen donors, it is likely that N-V-O would occur in the negative charge state, and therefore it would not be in the correct spin-state for OK1.

Table 6.5: Hyperfine tensors for the Ti-V-N and NVO complexes (MHz). θ and ϕ are as indicated in Table 6.1, θ' is the angle A_{\parallel} makes with $\langle 110 \rangle$ within the mirror plane for axially symmetric tensors. Experimental values are taken from Refs. [8, 11, 12]

Site	A_1		A_2		A_3		θ'
Ti-V-N, Fig. 6.3(a)							
N	-0.4	(150,225)	-0.2	(90,135)	0.2	(120,45)	60°
Ti	26.8	(116,225)	10.1	(90,315)	9.5	(26,225)	-
C ₁	46.7	(119,316)	17.0	(124,204)	16.7	(132,77)	119°
C ₂	64.5	(120,317)	24.3	(150,127)	24.1	(86,44)	120°
C ₃	25.9	(128,45)	8.9	(90,315)	7.9	(142,225)	128°
(NVO) ⁰ , $S = 1/2$, Fig. 6.3(b)							
N	-2.6	(128,225)	-2.3	(90,315)	-1.9	(142,45)	38°
C ₁	320.6	(123,315)	192.4	(85,42)	192.1	(34,305)	123°
O	45.4	(139,225)	48.4	(90,135)	49.3	(131,45)	-
(NVO) ¹⁺ , $S = 1$							
N	25.1	(51,225)	16.0	(90,135)	16.0	(39,45)	39°
C ₁	218.6	(125,315)	106.5	(35,311)	106.1	(88,44)	125°
O	-11.2	(42,45)	-7.8	(90,135)	-7.6	(132,45)	48°
(NVO) ¹⁻ , $S = 1$							
N	-1.6	(50,00)	-1.5	(120,298)	-1.3	(125,52)	-
C ₁	168.6	(124,315)	100.4	(34,304)	100.6	(85,41)	124°
O	-100.0	(129,306)	-66.1	(115,194)	-65.0	(49,260)	-
Experiment							
N	21.66	-	15.48	-	15.19	-	25°
C	Ref. [10]	127	(129,141)	74	(139,306)	74	(97,45)
C	Ref. [11]	122.87	-	73.37	-	73.37	-
Ti	A=1.55						-

In the negative charge state the oxygen atom becomes two-fold coordinated, and an additional carbon radical is formed. The spin-triplet configuration is more stable than the spin-singlet by around 0.4 eV, but the magnitude of the hyperfine on the N atom is very small, at variance with the OK1 centre. In the positive charge state a spin-triplet configuration is around 0.3 eV higher in energy than the spin singlet configuration, and although there is superficial agreement with experiment (see Table 6.5), the location of the donor level close to the valence band makes this charge and spin configuration unlikely.

It is therefore concluded that none of the current models for OK1 is a strong candidate.

6.4 Conclusions

The results of density functional simulations of candidate structures for the N3 and OK1 EPR centres in diamond have been presented.

Of the configurations investigated, the most suitable candidate structure for N3 is N_s-O_s . The spin density is mostly associated with a carbon site relatively distant from the N atom, consistent with the small hyperfine interactions calculated and observed. Additional support for the model comes from the motional averaging from the planar to axial symmetry activated by 0.45 eV, which is broadly consistent with an axial hyperfine interaction measured at 550 °C. The lack of any direct observation of oxygen remains a significant problem, and a definitive assignment cannot be made at this time. However, the calculations allow a more definitive rejection of other models such as Ti_s-N_s .

For OK1, *none* of the proposed models yield hyperfine tensors in agreement with experimental values. For N_s-C-O_s , although a contrived combination of structural configurations can yield a passing resemblance to experiment, this structure is 3 eV higher in energy than the nearest-neighbour pair, and the evidence for the presence of oxygen is very weak. The Ti-V-N and N-V-O complexes are similarly poor fits with experiment, and are also rejected these as candidates for OK1. It is concluded that a plausible model for the OK1 EPR centre in diamond remains to be found.

Finally, none of the calculated ^{17}O hyperfine interactions are in close agreement with

the only known values from experiment, taken from the nearly isotropic KUL12 EPR centre [122]. Indeed, of the centres analysed for this study, the closest in magnitude to KUL12 is the model structure for OK1, shown in Fig. 6.2(c), which does not have the correct axial symmetry. Since KUL12 is seen in ostensibly nitrogen-free diamond which has been irradiated and annealed, it seems likely that KUL12 is a simple defect, possibly involving one or more native defects, which are the topic of a future study.

CHAPTER

7

Calculated Hyperfine Interaction Parameters for P-Containing Point Defects in Diamond

7.1 Introduction

As described in chapter 1, A challenge in the effort to produce diamond for electronics lies in overcoming the difficulty in production of low resistivity n-type material. Nitrogen undergoes a significant chemical structural relaxation rendering it a very deep donor at around $E_c - 1.7$ eV [16], whereas phosphorus undergoes a more modest Jahn-Teller distortion. However, with a donor level at around $E_c - 0.6$ eV [17], P also has a low ionisation fraction at room temperature.

Electron paramagnetic resonance (EPR) is a powerful experimental tool in the identification of the microscopic structure for systems with unpaired electrons. Since phosphorus naturally occurs with 100% abundance with a nuclear spin of $I = 1/2$, hyperfine interactions between unpaired electrons and P-nuclei provide a direct probe to the local symmetry and localisation of spin density at the P site. Several EPR centres involving P have been reported, including an assignment to substitutional P [133–136]. At temperatures below around 30 K, EPR data suggest that P_s has D_{2d} symmetry [135, 136], corresponding to a Jahn-Teller distortion found from first-principles modelling [13, 137].

The evidence for *complexes* involving phosphorus is much less clear. The assignment [14] of an EPR centre to a complex of P with N is based upon similarities to the N1 EPR centre for which there is convincing evidence that the structure is a second-neighbour pair of nitrogen atoms [3–5, 117]. Another complex likely to be formed in consists of a P-vacancy pair (P–V). Theory predicts [124, 138] that P–V adopts the split semi-vacancy structure with the P atom lying at the centre of a di-vacancy. The acceptor level of P–V lies below the donor level of P_s , so one would expect them to be in the EPR-inactive, negative charge state. This might explain the current absence of any evidence from EPR for these complexes, which is in contrast to experimental observation split-vacancy complexes involving sulphur [139] and silicon [63, 84, 124, 140].

B impurity partners are also likely to produce EPR inactive complexes. However, P complexing with itself, forming nearest or next-nearest neighbour pairs might be a candidate since theoretically such centres are energetically bound, and have donor levels above the acceptor levels of P–V complexes [79, 130].

This chapter presents the calculated properties of P-containing centres in diamond, placing particular focus upon the hyperfine interactions at P-sites and, where possible, compare the calculated values with experimental observation.

7.2 Methodology

All calculations were carried out as described in chapter 2. C, O, N and P are treated using fixed linear-combinations of *s*- and *p*-orbitals of four widths. One (four) set(s) of *d*-Gaussians are included for C and O (N and P) to accommodate polarisation. Generally 216-atom, simple-cubic supercells of side length $3a_0$ are used, except for the calculation of reorientation barriers. Electrical levels are estimated by calculating the formation energies of different charge states and determining the critical values of the electron chemical potential [81].

7.3 Substitutional P

Although experimentally P_s is assigned to the tetragonal NIMS-1 centre at low temperature (10s of K) [135], theoretically it is metastable under several types of Jahn-Teller distortion [13, 137].

For the on-site, tetrahedral defect there is a single electron in a triply degenerate (t_2) state, predominantly localised on the P atom and its immediate neighbours. A distortion to trigonal (C_{3v}) or tetragonal (D_{2d}) splits the triplet into a_1 and e , and b_2 and e respectively. In a previous study [13] using methods similar to those employed here, three distinct structures were identified in the largest supercells examined (PC_{511}). The lowest energy tetragonal form found previously is shown schematically in Fig. 7.1 with the wave function of the unpaired electron. The total energies of C_{2v} , D_{2d} and C_{3v} structures were found to lie within 2 meV of each other and around 20 meV lower than the on-site version.

Geometrically, the distortions are extremely subtle, with the C–P bonds being the same length in the D_{2d} and T_d forms, and second-neighbour distances differing by just 0.02Å. The simulated hyperfine tensors for different symmetries are listed in Table 7.1. Starting with a comparison of the higher temperature, isotropic hyperfine interactions. Comparison of the on-site values with the room-temperature assignment to an isotropic centre [133, 134] is tolerable, and calculating the motional average of the three orientations of the $D_{2d}(2)$ structure yields an isotropic interaction only very slightly greater, at 101 MHz. The magnitudes

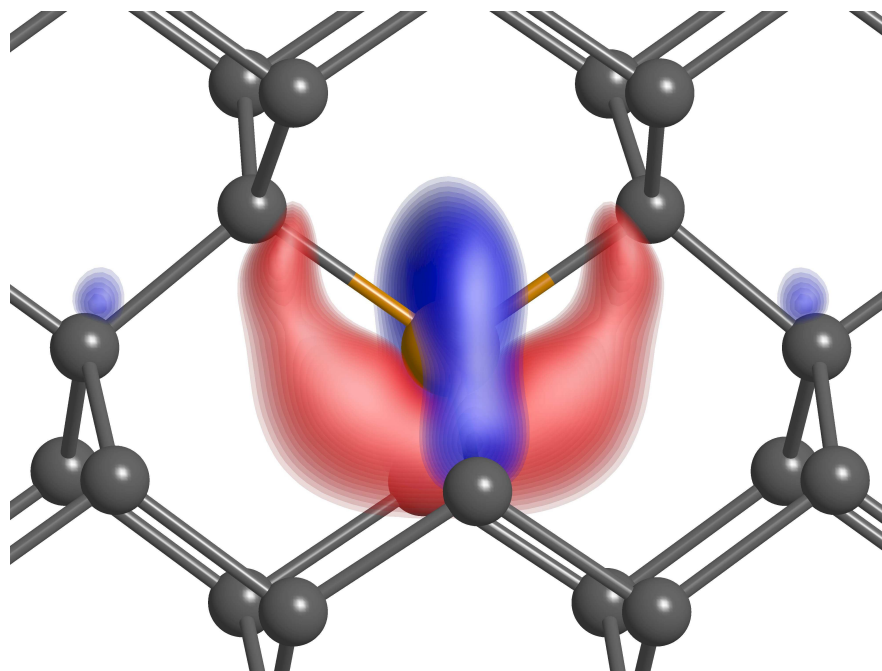


Figure 7.1: Kohn-Sham iso-surface for the highest occupied orbital of the $D_{2d}(2)$, Jahn-Teller distorted configuration of substitutional P in diamond.

for the low energy tetragonal structures are in reasonable agreement with the low temperature hyperfine interactions, and in particular, the lower energy $D_{2d}(2)$ structure yields much better agreement than the alternative $D_{2d}(1)$ symmetry.

It seems therefore plausible based upon the accumulated data including structural distortions and hyperfine interactions that the NIMS-1 EPR centre is the phosphorus donor, undergoing a Jahn-Teller distortion at low temperature to the particular D_{2d} structure identified previously from density functional simulations [13].

Finally, neighbouring ^{13}C are also expected to yield information to specify the structure of the phosphorus donor in EPR. For the experimentally relevant on-site and D_{2d} structures, the nearest carbon neighbours are equivalent and yield approximately isotropic hyperfine interactions between 40 and 44 MHz.

Table 7.1: Hyperfine tensor magnitudes (MHz) and directions in spherical polar angles for ^{31}P in substitutional P in diamond for different distortions. Symmetries follow the labelling in Ref. [13].

Calculation			Experiment		
Symmetry	A_{\parallel}	A_{\perp}	Symmetry	A_{\parallel}	A_{\perp}
C_{3v}	246	057	Isotropic [133]	119	119
$D_{2d}(1)$	57	115	Isotropic [134]	114	114
$D_{2d}(2)$	198	53	D_{2d} [135]	241	48
T_d	99	99	D_{2d} [136]	246	51

7.4 Phosphorus–nitrogen pairs

Experimentally, the only other assignment is the monoclinic-I, $S = 1/2$ NIRIM-8 centre to a charged P–N complex [14]. $\text{P}_s\text{--N}_s$ pairs at nearest and second nearest neighbour sites have simulated. The neutral charge state is EPR inactive, forming $\text{P}_s^+\text{--N}_s^-$, donor-acceptor pairs, and both structures distort as shown schematically in Fig. 7.2, consistent with the predicted [116] structure if N_s^- . (Possible structures with the C–N dilation in different directions have been examined, and those shown are the lowest in energy by around 0.2 eV.) The donor level for the nearest and the next-nearest neighbour pairs are estimated at 0.3 eV and 0.5 eV lower than N_s , *i.e.* $E_c - 2.0$ eV and $E_c - 2.2$ eV. In the overall positive charge state, the phosphorus donor is ionised and most of the spin-density is associated with the C-neighbour of neutral substitutional N. The calculated hyperfine tensors are listed in Table 7.2. The agreement with NIRIM-8 is poor, but consistent with the calculated localisation of the unpaired electron in the vicinity of the carbon radical site. Indeed, the hyperfine interactions for these centres are very similar to the P1-EPR centre arising from isolated N_s^0 .

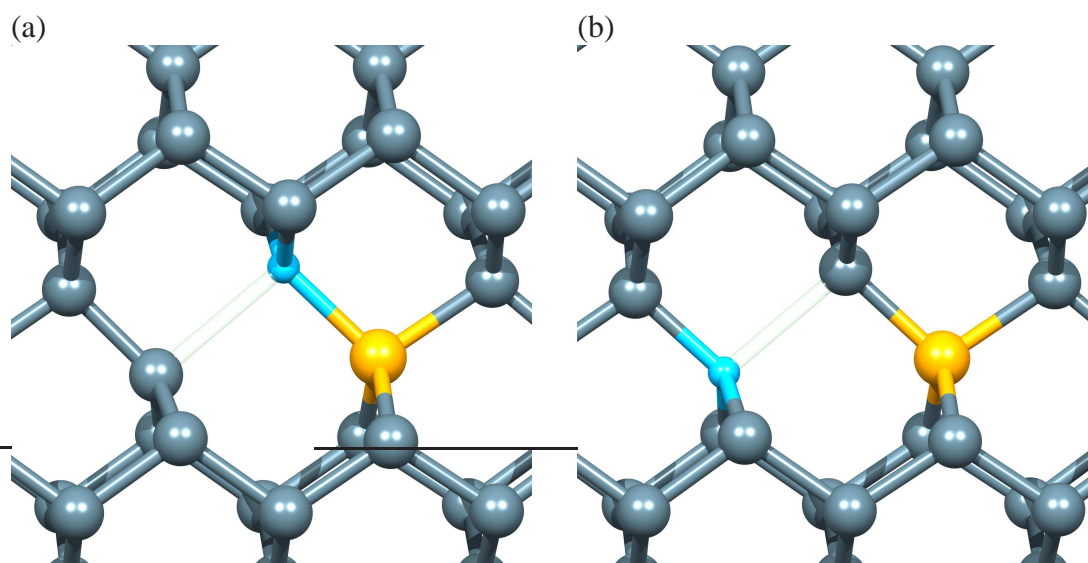


Figure 7.2: Schematics of phosphorus-nitrogen complexes in diamond: (a) $(\text{P–N})^+$ and (b) $(\text{P–C–N})^+$. In both cases the structures may be viewed as $\text{P}_s^+–\text{N}_s^0$ pairs, leading to the approximate axial symmetry for the dilated N–C bond. Horizontal and vertical directions are $[110]$ and $[001]$ respectively.

Table 7.2: Calculated isotropic (A_s) and anisotropic (A_p) hyperfine interactions (MHz) of ^{31}P , the under-co-ordinated ^{13}C and ^{14}N in $(\text{P–N})^+$ and $(\text{P–C–N})^+$ complexes in diamond. These should be compared with the experimental [14] values for the monoclinic-I NIRIM-8 EPR centre, with $A_s = 98$ MHz, and $A_p = 85$ MHz.

	$(\text{P–N})^+$				$(\text{P–C–N})^+$			
	A_s	A_p	A_{\parallel}	A_{\perp}	A_s	A_p	A_{\parallel}	A_{\perp}
^{31}P	4	2	-	-	-39	4	-	-
^{13}C	230	74	378	156	235	54	343	181
^{14}N	75	9	94	66	98	18	134	80

7.5 Phosphorus–boron pairs

P–B pairs have also been examined. In contrast to P–N, these donor–acceptor complexes have *no gap states* and it is difficult to see how P–B pairs would be thermally ionised to

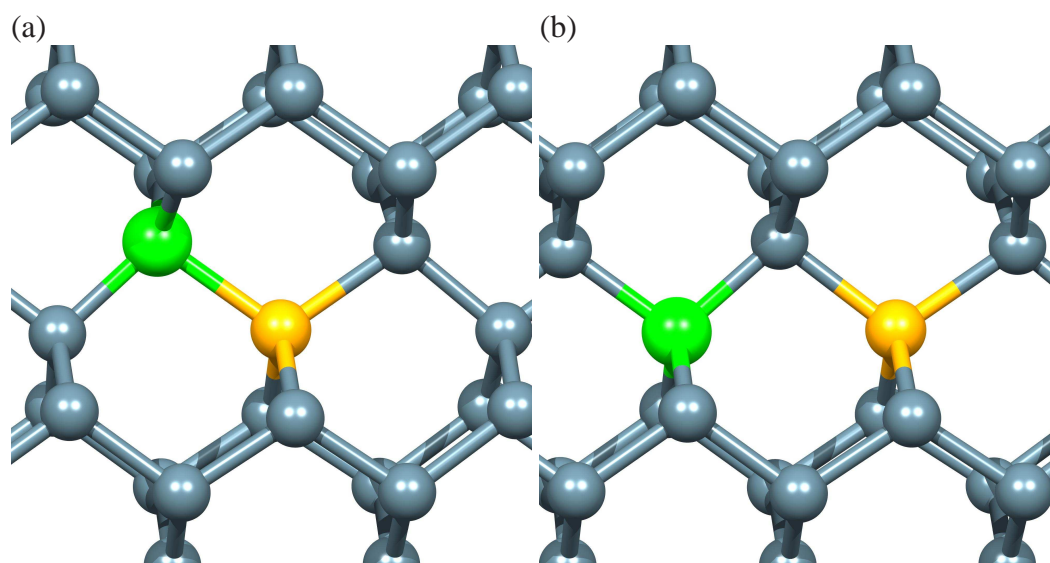


Figure 7.3: Schematics of phosphorus-boron complexes (a) The ionised $(\text{P-B})^+$ and (b) The ionised $(\text{P-C-B})^+$.

form an EPR active centre. However, in principle it should be possible to generate non-equilibrium EPR active structures made up from $\text{P}_s^+ - \text{B}_s^0$ or $\text{P}_s^0 - \text{B}_s^-$, perhaps under optical excitation.

Perhaps surprisingly, it is found that P–B pairs are more stable at second neighbour sites than nearest neighbours. The energy difference between nearest and next-nearest neighbour configurations is just 0.15 eV, and in contrast to what will be shown for phosphorus–pairs in section 7.8, there is no evidence in the calculations for direct bonding interaction in the lower energy, second neighbour form. The marginal stability of P–C–B over P–B is only weakly dependent upon charge state, with both positive and negative charge states favouring second neighbour pairs by 0.19 eV and 0.31 eV, respectively.

The hyperfine interaction in the thermodynamically metastable charge states are listed in Table 7.3. For the nearest neighbour pair in the overall positive charge state, the electron spin is distributed over both impurity sites, whereas in the next-neighbour configuration the spin is more associated with the boron site, as one might expect for $\text{P}_s^+ - \text{B}_s^0$.

For the overall negative charge state the system resembles P_s^0 both in terms of the magnitude and directions of the hyperfine interactions at the phosphorus-site.

Table 7.3: Calculated hyperfine interactions for ^{31}P – ^{11}B complexes in diamond (MHz). For axially symmetric $(\text{P–B})^q$ centres, A_{\parallel} lies along [111]. For $(\text{P–C–B})^q$ complexes in diamond both magnitude and direction (θ, ϕ) are in terms of the inclination, θ , with respect to [001] and azimuthal angle, ϕ , measured from [100] towards [010] (degrees).

	q	$(\text{P–B})^q$		$(\text{P–C–B})^q$					
		A_{\parallel}	A_{\perp}	A_1	A_2	A_3	A_4	A_5	A_6
^{31}P	+1	58	21	13	(45,50)	1	(315,90)	0	(45,140)
^{31}P	–1	25	58	171	(45,90)	39	(0,0)	30	(135,90)
^{11}B	+1	–68	–73	–117	(225,34)	–115	(135,90)	–110	(45,57)
^{11}B	–1	41	40	0	(45,93)	0	(135,90)	–1	(45,3)

7.6 Phosphorus–oxygen pairs

The structure of P–O pairs have also been examined. As with the P–B pairs, the neutral and negatively charged P–O complexes favour a second-neighbour structure with low symmetry, as shown schematically in Fig. 7.4(b). In the neutral charge state, the nearest neighbour form shown in Fig. 7.4(a) is favoured. Since there is likely to be an appreciable barrier to conversion between first and second neighbour structures, the calculated donor and acceptor levels are required for both types of defect. The donor and acceptor levels are calculated to be at 2.8 eV and 3.7 eV from the valence band top in the nearest-neighbour pairing, and at 1.9 eV and 3.7 eV in the second-neighbour case. Therefore in P-containing material, the most probable charge state is negative, and as such is EPR inactive.

In the neutral charge state, the complexes may be considered to be $\text{P}^+–\text{O}^-$, and one would then expect most of the spin density to reside in the vicinity of the oxygen site. As shown in Fig. 7.4, substitutional oxygen has neighbouring under-coordinated carbon sites, and it is here that the electrical activity originates. The calculated hyperfine interactions are listed in Table 7.4.

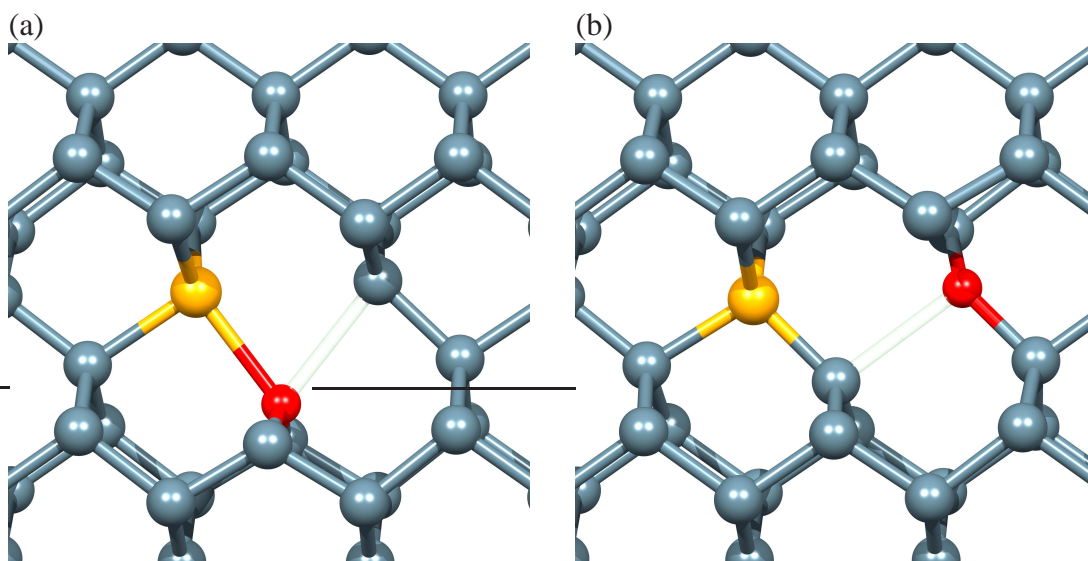


Figure 7.4: Schematics of phosphorus-oxygen complexes in diamond: (a) P–O and (b) P–C–O. In both cases the structures may be viewed as $P_s^+ - O_s^-$ pairs in the overall neutral charge state. Horizontal and vertical directions are [110] and [001] respectively.

Table 7.4: Calculated isotropic (A_s) and anisotropic (A_p) hyperfine interactions (MHz) of ^{31}P , the under-co-ordinated ^{13}C and ^{17}O in $(\text{P-O})^0$ and $(\text{P-C-O})^0$ complexes in diamond.

	$(\text{P-O})^0$		$(\text{P-C-O})^0$	
	A_s	A_p	A_s	A_p
^{31}P	1770	109	-7	1
^{13}C	223	45	29	5
^{17}O	-62	20	-150	16

7.7 Phosphorus–vacancy complexes

Theoretically P can be readily incorporated into diamond as a complex with a lattice vacancy [124, 138], where P lies between two semi-vacancies. P–V is predicted to be a deep

acceptor, and thus a strong candidate for phosphorus-related self-compensation. In the negative charge state P–V complexes are EPR inactive. However, under illumination the complex might be photo-ionised to produce the EPR-active, neutral charge state, and in anticipation of such an experiment the hyperfine tensors have been calculated for this D_{3d} symmetry structure.

Since the centre has axial symmetry, there are two independent values, which are found to be -119 MHz for the axial component, and -126 MHz for the two perpendicular components, with the direction depicted in Fig. 7.5. The axial component on the P atom is directed at 35° from $[110]$.

Thus, it is predicted here that the A -tensor for ^{31}P in a neutral P–V complex is nearly completely isotropic. The six neighbouring carbon sites are found to have almost axial A -tensors with $A_{\parallel} = 56$ MHz and $A_{\perp} = 26$ MHz, the axes being around 3° from $[111]$.

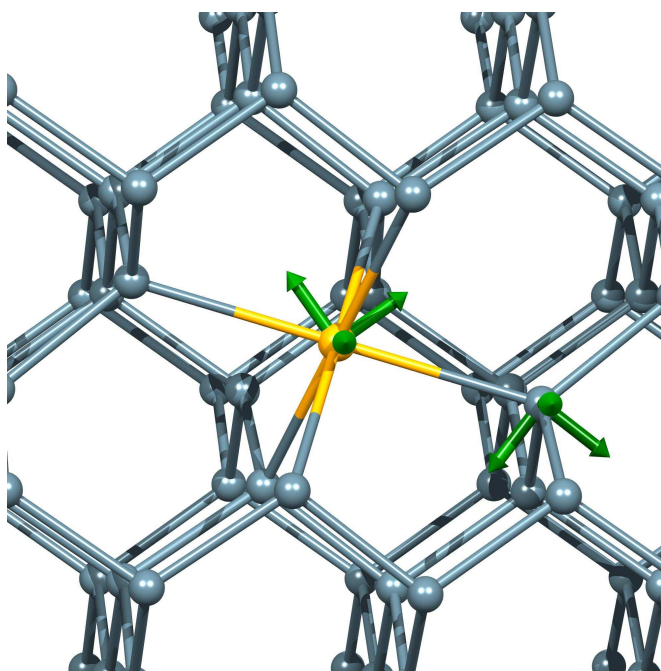


Figure 7.5: Schematic showing the P–V structure and the directions of the three components of the hyperfine interactions at P and a neighbouring C site.

7.8 Phosphorus pair

Previously it has been shown that P-impurities may be stabilised by the formation of second-nearest-neighbour pairs [79]. The stabilisation may be viewed as arising from the formation of an additional bonding combination of electrons in a fifth covalent bond between the P-atoms in addition to those with the four neighbouring carbon atoms. In heavily P-doped material, P-pairs may form, since the binding energy is intermediate between that of N- and B-pairs [141], for which the binding is either sufficient or insufficient to overcome the entropic and other temperature dependent terms in the free-energy, respectively.

The stabilisation of the centre and the formation of a bond between the P-atoms moves the donor level of the pair deep into the band-gap. In the neutral charge state the complex would be EPR inactive, but in the presence of deep acceptors (for example, those associated with carbon dangling bonds in vacancy-related centres), the pairs would be expected to become positively charged. Additionally, such deep centres can be photo-ionised to produce EPR-active states, such as is the case in N-pairs and the W24 centre [71–73].

In the positive charge state the formation of a P–P interaction is weakened and the spin density is distributed over the P-atoms and their carbon neighbours. The calculated hyperfine interactions are listed in Table 7.5.

Table 7.5: Hyperfine interactions (MHz) of ^{31}P and ^{13}C for the sites indicated in Fig. 7.6. The directions in parentheses are indicated in spherical-polar co-ordinates with θ measured from [001] and ϕ from [100] towards [010].

	A ₁		A ₂		A ₃	
^{31}P	12	(90,315)	14	(30,225)	159	(120,225)
$^{13}\text{C}_1$	107	(90,45)	109	(90,315)	141	(180,00)
$^{13}\text{C}_2$	68	(90,315)	68	(33,45)	86	(123,45)
$^{13}\text{C}_3$	25	(38,346)	27	(118,33)	35	(114,290)
$^{13}\text{C}_4$	-1	(90,45)	-1	(9,135)	4	(81,315)

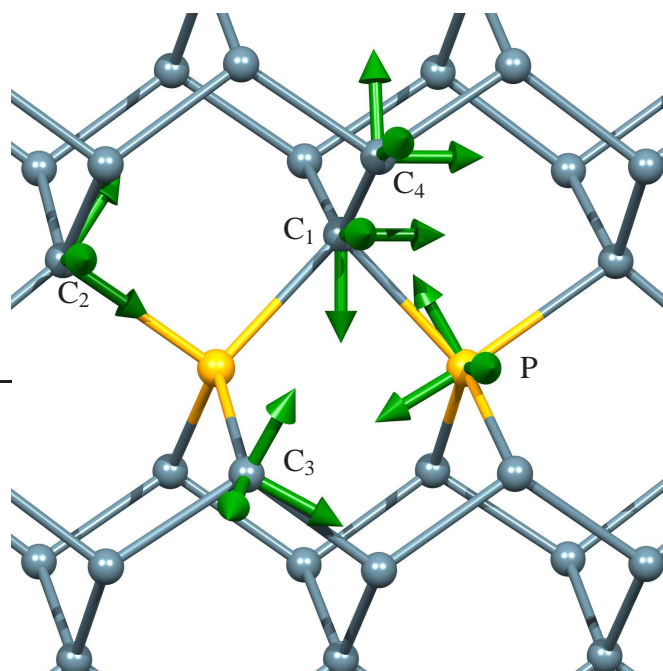


Figure 7.6: Schematic showing the P-N-P structure and the directions of the three components of the hyperfine interactions at P and a neighbouring C sites.

7.9 Conclusions

Calculated hyperfine interactions for substitutional P with D_{2d} and T_d symmetries yield reasonable quantitative agreement with experimental values, and allow for increased confidence in the sense of the Jahn-Teller distortion at these centres. P-N and P-C-N complexes are predicted to have very deep donor levels, and this raises questions as to whether or not one would expect the EPR active positive charge state to be present in n-type diamond. The assignment of the NIRIM-8 centre to the P-C-N complex is doubtful, given the localisation of the unpaired electron and the small hyperfine interactions predicted for this centre. The lack of a thermodynamically stable, EPR active charge state for P-B complexes means that these will be difficult to detect even if present in the material. Finally, the hyperfine interactions for P in P-V complexes have been calculated, and it is found that the hyperfine interactions will be dominated by the isotropic contribution, similar to the S-V complex assigned to the W31 EPR centre [139].

Part III

Conclusions

CHAPTER

8

Summary

8.1 Summary

In this thesis the results was carried out using ab initio modelling code to determine some of important properties of diamond such as hyperfine interaction, stability, electrical and electronic structure. Conclusion has been drawn at the end of each application's chapter. In this chapter the important areas are reviewed.

Density functional simulations of nitrogen pairs in diamond have largely confirmed the atomistic models proposed for N-pair defects in diamond, with two qualifications. (i) for N1, it is proposed a re-assignment of the hyperfine-interactions for near-by ^{13}C and the corresponding numbers of equivalent sites. (ii) for N4, in order to render the N-atoms equivalent a rapid reorientation between two structures must be invoked, so that the low temperature EPR spectra are the result of a thermal, or quantum-tunnelling average of two systems

where the N-atoms are nonequivalent. Values are predicted for the hyperfine-interactions at the carbon sites where the majority of the spin-density is located. Indeed, it is somewhat surprising that N1, W7, N4, M2 and M3 this radical site has not been seen, yet in the case of N1 many other carbon sites have.

The hyperfine-tensors for complexes of muonium with A- and B-centres mean that these centres are most probably not responsible for Mu_X . However, there are a number of ways that the calculation must be viewed. First is that the calculations relate to a static structure, whereas the experiment involves the motion of the constituents. Indeed, it has been suggested that some of the error in the estimate of the hyperfine-tensors for anomalous muonium in pure diamond arise from the zero-point motion of the very light muon along the axis of the C–C bond [106–108]. It might be asked the question as to if motional effects for either of the complexes can result in agreement with the Mu_X parameters. It seems unlikely since even in the case of Mu_{BC} the effect of including motional averaging is a perturbation, whereas for either of the two N-containing complexes with muonium, the isotropic term must increase by two orders of magnitude to match the measured values of Mu_X .

A second possibility, given the large uncertainty in the experimental parameters, is that μSR is resolving the muonium annihilation events in a region not directly within the N-aggregates, but in an approximately tetrahedral cage in the immediate vicinity of them. However, the perturbation to the hyperfine-tensors of Mu_{T} even in the T-sites adjacent to the A- and B-centres is very small, and the binding energies in these chemically unreacted sites are also very small, so this interpretation seems unlikely to be correct. A final possibility that it will be discussed is that muonium is tunnelling rapidly between sites around the N-aggregates. Indeed, such effects are thought to be present in the case of muonium in Zn-doped GaAs [115], but if this were the case in N-containing diamond, it is not obvious why the resulting hyperfine-tensor would be non-axial given the high symmetry of the two nitrogen aggregates involved.

There remains the possibility that the Mu_X centre is not associated with the N-aggregates directly. In fact there are two good candidates for sites in material containing aggregated N. In such diamond there is evidence for nano-cavities and planar self-interstitial aggregates,

both of which have open regions to trap the mobile muonium, that would result in isotropic components to the hyperfine-interaction, consistent with the measured values for Mu_X . Of these, perhaps the more favourable option would be the self-interstitial precipitate, as this has a reasonably regular structure that would yield a non-axial tensor. both of which have favourable properties but also are imperfect fits to the experimental data.

Of the first row elements, it is perhaps most surprising that relatively little evidence exists for the presence of oxygen in the form of distributed point-defects. The paramagnetic centres labelled N3 and OK1 have been assigned to structures made up from two structural arrangements of pairs of substitutional nitrogen and oxygen, but there is no direct evidence for the involvement of the oxygen. The most plausible candidate structure for N3 is $\text{N}_s\text{-O}_s$. The small hyperfine interactions calculated consistent with observed. This show that the spin density is mostly associated with a carbon site. Which could be interpreted as the unpaired electron is further away than the nearest neighbour. The proposed model nitrogen with di-vacancy for N3 centre is contrast with motional average that observed at temperature more than 550 °C. The relatively accurate result for N–O nearest neighbour is agreed with the experimental where with barrier about 0.45 eV there is possibility to get motional average at temperature less than 550 °C. However, the calculations allow a more definitive rejection of other models such as $\text{Ti}_s\text{-N}_s$. For OK1, the $\text{N}_s\text{-C-O}_s$, Ti-V-N and N-V-O complexes are similarly poor fits with experiment, and it is also rejected these as candidates for OK1. It is concluded that a plausible model for the OK1 EPR centre in diamond remains to be found.

Substitutional P with C_{3v} gives quite a good fit compared to the experimental values favouring the lower energy in D_{2d} model for the Jahn-Teller system. The EPR centre called NIRIM-8 is believed to be substitutional nitrogen at the next neighbour to P^+ , as it resembles the N1 centre which is neutral nitrogen next to an N^+ neighbour. P–N and P–C–N with very deep donor levels have a small chance to be positively charged (and hence EPR active), and combined with the hyperfine tensor values it cannot be confirmed that NIRIM-8 centre is one of them. The same situation is found for P–B, P–C–B with no donor levels in the band gap. P–V, however, with deep acceptor level, is expected to occur the EPR inactive negative

charge state. However, under illumination the complex might be photo-ionised to produce an EPR-active form, for which characteristic A-tensor have been calculated.

It can be concluded that the ab initio modelling techniques have been successful as a quantitative tool, and have proven to be given a good fit for several experimental result assignments. This provides confidence in values obtained for cases where experimentally based atomistic models yield hyperfine tensors in poor agreement with observation.

Bibliography

- [1] V. A. Nadolinny, A. P. Yelisseyev, J. M. Baker, D. J. Twitchen, M. E. Newton, A. Hofstaetter, and B. Feigelson, “EPR spectra of separated pairs of substitutional nitrogen atoms in diamond with a high concentration of nitrogen,” *Phys. Rev. B* **60**, pp. 5392–5403, August 1999.
- [2] C. A. J. Ammerlaan, *Semiconductors, Impurities and Defects in Group IV Elements and III-V Compounds*, vol. III22B of *Landolt-Börnstein, New Series*. Springer, Berlin, 1990.
- [3] A. Cox, M. E. Newton, and J. M. Baker, “ENDOR studies of the N1 di-nitrogen centre in diamond,” *J. Phys. Cond. Matter* **4**, pp. 8119–8130, 1992.
- [4] M. Y. Shcherbakova, E. V. Sobolev, N. D. Samsonenko, and V. K. Aksenov, “Electron paramagnetic resonance of ionized nitrogen pairs in diamond,” *Sov. Phys. Solid State* **11**(5), pp. 1104–1106, 1969.
- [5] M. E. Newton and J. M. Baker, “Models for the di-nitrogen centres found in brown diamond,” *J. Phys. Cond. Matter* **3**, pp. 3605–3616, 1991.

- [6] M. E. Newton and J. M. Baker, "ENDOR studies on the W7 di-nitrogen centre in brown diamond," *J. Phys. Cond. Matter* **3**, pp. 3591–3603, 1991.
- [7] R. M. Mineeva and A. V. Speransky, "EPR studies on the di-nitrogen centers with nonequivalent atoms in a reddish-brown plastically deformed diamond," *Appl. Magn. Reson.* **28**(3-4), pp. 355–364, 2005.
- [8] J. A. van Wyk, J. H. N. Loubser, M. E. Newton, and J. M. Baker, "ENDOR and high-temperature EPR of the N3-center in natural type-Ib diamonds," *J. Phys. Cond. Matter* **4**, pp. 2651–2662, MAR 9 1992.
- [9] M. E. Newton and J. M. Baker, "¹⁴N ENDOR of the OK1 centre in natural type Ib diamond," *J. Phys. Cond. Matter* **1**(51), pp. 10549–10561, 1989.
- [10] G. J. Hill, A. VanWyk, and M. J. R. Hoch, "EPR of oxygen centres in natural diamond," *Radiation Effects and Defects in Solids* **156**, pp. 221–225, 2000.
- [11] V. A. Nadolinny, O. P. Yuryeva, V. S. Shatsky, A. S. Stepanov, V. V. Golushko, M. I. Rakhmanova, I. N. Kupriyanov, A. A. Kalinin, Y. N. Palyanov, and D. Zedgenizov, "New data on the nature of the EPR OK1 and N3 centers in diamond," *Appl. Magn. Reson.* **36**, pp. 97–108, 2009.
- [12] V. A. Nadolinny, O. P. Yuryeva, and V. S. Chepurov, A. and Shatsky, "Titanium ions in the diamond structure: Model and experimental evidence," *Appl. Magn. Reson.* **36**, pp. 109–113, 2009.
- [13] R. J. Eyre, J. P. Goss, P. R. Briddon, and J. P. Hagon, "Theory of Jahn-Teller distortions of the P donor in diamond," *J. Phys. Cond. Matter* **17**, pp. 5831–5837, 2005.
- [14] J. Isoya, H. Kanda, M. Akaishi, Y. Morita, and T. Ohshima, "ESR studies of incorporation of phosphorus into high-pressure synthetic diamond," *Diamond Relat. Mater.* **6**(2-4), pp. 356–360, 1997.
- [15] E. Gheeraert, S. Koizumi, T. Teraji, H. Kanda, and M. Nesládek, "Electronic states of boron and phosphorus in diamond," *Phys. Status Solidi A* **174**(1), pp. 39–51, 1999.

- [16] R. Farrer, "On the substitutional nitrogen donor in diamond," *Solid State Commun.* **7**, p. 685, 1969.
- [17] E. Gheeraert, S. Koizumi, T. Teraji, and H. Kanda, "Electronic transitions of electrons bound to phosphorus donors in diamond," *Solid State Commun.* **113**, pp. 577–580, 2000.
- [18] A. M. Stoneham, A. H. Harker, and G. W. Morley, "Could one make a diamond-based quantum computer?," *J. Phys. Cond. Matter* **21**(36), p. 364222, 2009.
- [19] V. Blank, M. Popov, N. Lvova, K. Gogolinsky, and V. Reshetov, "Nano-sclerometry measurements of superhard materials and diamond hardness using scanning force microscope with the ultrahard fullerite C-60 tip," *J. Mater. Res.* **12**, pp. 3109–3114, 1997.
- [20] S. M. Sze, *Physics of Semiconductor Devices*, Wiley-Interscience, New York, 2nd ed., 1981.
- [21] D. R. Lide, ed., *CRC handbook of chemistry and physics*, CRC Press, London, 75 ed., 1995.
- [22] Y. Yamamoto, T. Imai, K. Tanabe, T. Tsuno, Y. Kumazawa, and F. N., "The measurement of thermal properties of diamond," *Diamond Relat. Mater.* **6**, p. 1057, 1997.
- [23] S. Barman and G. P. Srivastava, "Quantitative estimate of phonon scattering rates in different forms of diamond," *prb* **73**(7), p. 073301, 2006.
- [24] A. T. Collins, H. Kanda, and H. Kitawaki, "Colour changes produced in natural brown diamonds by high-pressure, high-temperature treatment," *Diamond Relat. Mater.* **9**(2), pp. 113–122, 2000.
- [25] P. M. Martineau, S. C. Lawson, A. J. Lawson, S. J. Quinn, J. F. Evans, and M. J. Crowder *Gems Gemol.* **40**, p. 2, 2004.

- [26] D. Fisher and R. A. Spits, "Spectroscopic evidence of geophysical-treated natural diamonds," *Gems Gemol.* **36**, p. 42, 2000.
- [27] J. Walker, "Optical-absorption and luminescence in diamond," *Rep. Prog. Phys.* **42**, p. 1605, 1979.
- [28] G. Davies, *properties and growth of diamond*, Institution of electrical engineers, London, 1994.
- [29] D. J. Poferl, N. C. Gardner, and J. C. Angus, "Growth of boron-doped diamond seed crystals by vapor-deposition," *J. Appl. Phys.* **44**, pp. 1428–1434, 1973.
- [30] R. M. Shrenko, H. M. Strong, and R. E. Tuft *Phil. Mag.* **11**, p. 313, 1965.
- [31] J. E. Butler and D. G. Goodwin, "Cvd growth of diamond," in *Properties, growth and applications of diamond*, M. H. Nazaré and A. J. Neves, eds., *EMIS Datareviews Series(26)*, ch. B1.3, pp. 262–272, INSPEC, Institute of Electrical Engineers, London, 2001.
- [32] H. Windischmann, "CVD diamond for thermal management," in *Properties, growth and applications of diamond*, M. H. Nazaré and A. J. Neves, eds., *EMIS Datareviews Series(26)*, ch. C2.2, pp. 410–415, INSPEC, Institute of Electrical Engineers, London, 2001.
- [33] E. Vittone and C. Manfredotti, "Diamond x-ray dosimeters," in *Properties, growth and applications of diamond*, M. H. Nazaré and A. J. Neves, eds., *EMIS Datareviews Series(26)*, ch. C1.5, pp. 386–392, INSPEC, Institute of Electrical Engineers, London, 2000.
- [34] C. Wild and P. Koidl, "Optical properties of diamond and applications as radiation windows," in *Properties, growth and applications of diamond*, M. H. Nazaré and A. J. Neves, eds., *EMIS Datareviews Series(26)*, ch. C1.1, pp. 351–355, INSPEC, Institute of Electrical Engineers, London, 2000.

- [35] F. T. Charnock and T. A. Kennedy, “Combined optical and microwave approach for performing quantum spin operations on the nitrogen-vacancy center in diamond,” *Phys. Rev. B* **64**, p. 041201, Jun 2001.
- [36] R. Jones and P. R. Briddon, *The ab initio cluster method and the dynamics of defects in semiconductors*, vol. 51A of *Semiconductors and Semimetals*, ch. 6. Academic Press, Boston, 1998.
- [37] P. R. Briddon and R. Jones, “LDA calculations using a basis of Gaussian orbitals,” *Phys. Status Solidi B* **217**(1), pp. 131–171, 2000.
- [38] M. J. Rayson and P. R. Briddon, “Rapid iterative method for electronic-structure eigenproblems using localised basis functions,” *Computer Phys. Comm.* **178**, pp. 128–134, Feb. 2008.
- [39] M. Born and J. R. Oppenheimer, “,” *Ann. Phys.* **84**, p. 457, 1927.
- [40] D. R. Hartree, “The wave mechanics of an atom with a non-Coulomb central field. Part 1. Theory and methods.,” *Proc. Cambridge Philosophical Soc.* **24**, p. 89, 1927.
- [41] V. Fock, “Näherungsmethode zur Lösung des quantenmechanischen Mehrkörperproblems,” *Z. Phys.* **61**, p. 126, 1930.
- [42] L. H. Thomas, “The calculation of atomic fields,” *Proc. Cambridge Philosophical Soc.* **23**, pp. 542–548, 1927.
- [43] E. Fermi, “Un metodo statistico per la determinazione di alcune proprietà dell’atomo,” *Rendiconti Accademia dei Lincei* **6**, pp. 602–627, 1927.
- [44] P. Hohenberg and W. Kohn, “Inhomogeneous electron gas,” *Phys. Rev.* **136**(3B), pp. 864–871, 1964.
- [45] W. Kohn and L. J. Sham, “Self-consistent equations including exchange and correlation effects,” *Phys. Rev.* **140**(4A), pp. A1133–A1138, 1965.

- [46] W. Kohn and L. J. Sham, “Quantum density oscillation in an inhomogeneous electron gas,” *Phys. Rev.* **137**(6), pp. A1697–A1705, 1965.
- [47] U. von Barth and L. Hedin, “A local exchange-correlation potential for the spin polarized case,” *J. Phys. C* **5**, pp. 1629–1642, July 1972.
- [48] J. P. Perdew and A. Zunger, “2 theorems on the self-interaction in density functional theory,” *Bull. Am. Phys. Soc.* **26**(3), p. 470, 1981.
- [49] J. P. Perdew, K. Burke, and Y. Wang, “Generalized gradient approximation for the exchange-correlation hole of a many-electron system,” *Phys. Rev. B* **54**(23), pp. 16533–16539, 1996.
- [50] J. P. Perdew, K. Burke, and M. Ernzerhof, “Generalised gradient approximation made simple,” *Phys. Rev. Lett.* **77**, p. 3865, 1996.
- [51] M. J. Shaw, P. R. Briddon, J. P. Goss, M. J. Rayson, A. Kerridge, A. H. Harker, and A. M. Stoneham, “Importance of quantum tunneling in vacancy-hydrogen complexes in diamond,” *Phys. Rev. Lett.* **95**, p. 205502, 2005.
- [52] P. E. Blöchl, “Projector augmented-wave method,” *Phys. Rev. B* **50**(4), pp. 17953–17979, 1994.
- [53] C. Hartwigsen, S. Goedecker, and J. Hutter, “Relativistic separable dual-space gaussian pseudopotentials from H to Rn,” *Phys. Rev. B* **58**(7), pp. 3641–3662, 1998.
- [54] A. Baldereschi, “Mean-value point in the brillouin zone,” *Phys. Rev. B* **7**, pp. 5212–5215, Jun 1973.
- [55] D. J. Chadi and M. L. Cohen, “Special points in the brillouin zone,” *Phys. Rev. B* **8**, pp. 5747–5753, Dec 1973.
- [56] H. J. Monkhorst and J. D. Pack, “Special points for Brillouin-zone integrations,” *Phys. Rev. B* **13**(12), pp. 5188–5192, 1976.

- [57] E. Polak, *Computational methods in optimisation: a unified approach*, Academic Press, Berkley, California, USA, 1971.
- [58] W. Press, *Numerical Methods in Fortran 77*, Cambridge University Press, Cambridge, UK, 1996.
- [59] G. Henkelman, B. P. Uberuaga, and H. Jónsson, “A climbing image nudged elastic band method for finding saddle points and minimum energy paths,” *J. Chem. Phys.* **113**(22), pp. 9901–9904, 2000.
- [60] G. Henkelman and H. Jónsson, “Improved tangent estimate in the nudged elastic band method for finding minimum energy paths and saddle points,” *J. Chem. Phys.* **113**(22), pp. 9978–9985, 2000.
- [61] G. H. Vineyar, “Frequency factors and isotope effects in solid state rate processes,” *J. Phys. Chem. Solids* **3**, pp. 121–127, 1957.
- [62] G. D. Watkins and J. W. Corbett, “Defects in irradiated silicon. I. Electron spin resonance of the Si-A centre,” *Phys. Rev.* **121**(4), pp. 1001–1014, 1961.
- [63] A. M. Edmonds, M. E. Newton, P. M. Martineau, D. J. Twitchen, and S. D. Williams, “Electron paramagnetic resonance studies of silicon-related defects in diamond,” *Phys. Rev. B* **77**(24), p. 245205, 2008.
- [64] B. Hetényi, F. De Angelis, P. Giannozzi, and R. Car, “Reconstruction of frozen-core all-electron orbitals from pseudo-orbitals,” *J. Chem. Phys.* **115**, pp. 5791–5795, Oct. 2001.
- [65] R. Robertson, J. J. Fox, and A. E. Martin, “Two types of diamond,” *Phil. Trans. R. Soc. A* **232**, pp. 463–535, 1934.
- [66] J. P. Goss, B. J. Coomer, R. Jones, C. J. Fall, P. R. Briddon, and S. Öberg, “Extended defects in diamond: the interstitial platelet,” *Phys. Rev. B* **67**, p. 165208, April 2003.

- [67] W. V. Smith, P. P. Sorokin, I. L. Gelles, and G. J. Lasher, "Electron-spin resonance of nitrogen donors in diamond," *Phys. Rev.* **115**, pp. 1546–1553, September 1959.
- [68] A. T. Collins, M. Stanley, and G. S. Woods, "Nitrogen isotope effects in synthetic diamonds," *J. Phys. D* **20**, pp. 969–974, 1987.
- [69] S. C. Lawson, D. Fisher, D. C. Hunt, and M. E. Newton, "On the existence of positively charged single-substitutional nitrogen in diamond," *J. Phys. Cond. Matter* **10**, pp. 6171–6180, July 1998.
- [70] G. Davies, "Decomposing the IR absorption spectra of diamonds," *Nature* **290**, pp. 40–41, 1981.
- [71] G. Davies, "A-nitrogen aggregate in diamond - its symmetry and possible structure," *J. Phys. C* **9**, pp. L537–L542, 1976.
- [72] J. A. van Wyk and J. H. N. Loubser, "Electron-spin resonance of a di-nitrogen center in cape yellow type-Ia diamonds," *J. Phys. C* **16**(8), pp. 1501–1506, 1983.
- [73] O. D. Tucker, M. E. Newton, and J. M. Baker, "ESR and ^{14}N electron-nuclear double-resonance measurements on the ionized nearest-neighbor dinitrogen center in diamond," *Phys. Rev. B* **50**, pp. 15586–15596, December 1994.
- [74] M. Y. Shcherbakova, E. V. Sobolev, and V. A. Nadolinny, "Electronic paramagnetic resonance of low-symmetry impurities centers in diamond," *Sov. Phys. Dokl.* **204**(6), p. 851, 1972.
- [75] J. H. N. Loubser and A. C. J. Wright, "Singly ionized N-C-N center in diamond," *J. Phys. D* **6**(9), pp. 1129–1141, 1973.
- [76] R. M. Mineeva, A. V. Speransky, S. V. Titkov, and N. G. Zudin, "The ordered creation of paramagnetic defects at plastic deformation of natural diamonds," *Phys. and Chem. Minerals* **34**, pp. 53–58, 2007.

- [77] M. Y. Shcherbakova, E. V. Sobolev, V. A. Nadolinnyi, and V. K. Aksenov, “Defects in plastically-deformed diamonds, as identified by optical and ESR spectra,” *Sov. Phys. Dokl.* **20**(11), pp. 725–728, 1975.
- [78] C. M. Welbourn, “EPR studies of a two-nitrogen-atom centre in natural, plastically-deformed diamond,” *Solid State Commun.* **26**, pp. 255–260, 1978.
- [79] J. P. Goss, R. J. Eyre, and P. R. Briddon, “Bound substitutional impurity pairs in diamond: a density functional study,” *J. Phys. Cond. Matter* **20**, p. 085217, Feb. 2008.
- [80] D. A. Liberman, “Slater transition-state band-structure calculations,” *Phys. Rev. B* **62**(11), pp. 6851–6853, 2000.
- [81] J. P. Goss, M. J. Shaw, and P. R. Briddon, “Marker-method calculations for electrical levels using gaussian-orbital basis sets,” in *Theory of Defects in Semiconductors*, D. A. Drabold and S. K. Estreicher, eds., *Topics in Applied Physics* **104**, pp. 69–94, Springer, Berlin/Heidelberg, 2007.
- [82] S. Dannefaer, A. Pu, and D. Kerr, “Positron annihilation study of vacancies in type IIa diamonds illuminated with monochromatic light,” *Diamond Relat. Mater.* **10**, pp. 2113–2117, 2001.
- [83] J. H. N. Loubser and J. A. van Wyk, “,” *MRS Symp. Proc.* **46**, p. 587, 1985.
- [84] J. P. Goss, P. R. Briddon, S. J. Sque, and R. Jones, “Donor and acceptor states in diamond,” *Diamond Relat. Mater.* **13**(4–8), pp. 684–690, 2004.
- [85] L. S. Hounscome, R. Jones, P. M. Martineau, D. Fisher, M. J. Shaw, P. R. Briddon, and S. Öberg, “Origin of brown coloration in diamond,” *Phys. Rev. B* **73**(12), p. 125203, 2006.
- [86] D. C. Hunt, D. J. Twitchen, M. E. Newton, J. M. Baker, T. R. Anthony, W. F. Banholzer, and S. S. Vagarali, “Identification of the neutral carbon [100]-split interstitial in diamond,” *Phys. Rev. B* **61**(6), pp. 3863–3876, 2000.

- [87] J. P. Goss, B. J. Coomer, R. Jones, T. D. Shaw, P. R. Briddon, M. Rayson, and S. Öberg, “Self-interstitial aggregation in diamond,” *Phys. Rev. B* **63**(19), p. 195208, 2001.
- [88] J. Isberg, J. Hammersberg, E. Johansson, T. Wikström, D. J. Twitchen, A. J. Whitehead, S. E. Coe, and G. A. Scarsbrook, “High carrier mobility in single-crystal plasma-deposited diamond,” *Science* **297**, p. 1670, 2002.
- [89] C. Glover, M. E. Newton, P. Martineau, D. J. Twitchen, and J. M. Baker, “Hydrogen incorporation in diamond: The nitrogen-vacancy-hydrogen complex,” *Phys. Rev. Lett.* **90**, p. 185507, 2003.
- [90] C. Glover, M. E. Newton, P. M. Martineau, S. Quinn, and D. J. Twitchen, “Hydrogen incorporation in diamond: the vacancy-hydrogen complex,” *Phys. Rev. Lett.* **92**, p. 135502, 2004.
- [91] J. P. Goss, P. R. Briddon, R. Jones, and S. Sque, “The vacancy-nitrogen-hydrogen complex in diamond: a potential deep centre in chemical vapour deposited material,” *J. Phys. Cond. Matter* **15**, p. R2903, 2003.
- [92] A. Kerridge, A. H. Harker, and A. M. Stoneham, “Quantum behaviour of hydrogen and muonium in vacancy-containing complexes in diamond,” *J. Phys. Cond. Matter* **16**, p. 8743, 2004.
- [93] K. Iakoubovskii, A. Stesmans, K. Suzuki, A. Sawabe, and T. Yamada, “Symmetry of the hydrogen-vacancy-like defect H1 in diamond,” *Phys. Rev. B* **66**(11), p. 113203, 2002.
- [94] S. F. J. Cox and R. L. Lichti, “Muonium states and dynamics as a model for hydrogen in semiconductors,” *J. Alloys and Compounds* **253**, pp. 414–419, 1997.
- [95] E. Holzschuh, W. Kündig, P. F. Meier, B. D. Patterson, J. P. F. Sellschop, M. C. Stemmet, and H. Appel, “Muonium in diamond,” *Phys. Rev. A* **25**(3), pp. 1272–1286, 1982.

- [96] R. L. Lichti, S. F. J. Cox, K. H. Chow, E. A. Davis, T. L. Estle, B. Hitti, E. Mytilineou, and C. Schwab, "Charge-state transitions of muonium in germanium," *Phys. Rev. B* **60**(3), pp. 1734–1745, 1999.
- [97] S. F. J. Cox and M. C. R. Symons, "Molecular radical models for the muonium centers in solids," *Chem. Phys. Lett.* **126**(6), pp. 516–525, 1986.
- [98] S. F. J. Cox, "The shallow-to-deep instability of hydrogen and muonium in II-VI and III-V semiconductors," *J. Phys. Cond. Matter* **15**, pp. R1727–1780, 2003.
- [99] I. Z. Machi, S. H. Connell, M. Baker, J. P. F. Sellschop, K. Bharuth-Ram, C. G. Fischer, R. W. Nilen, S. F. J. Cox, and J. E. Butler, "A new muonium trap in nitrogen-rich diamond discovered by μ SR," *Physica B* **289–290**(1), pp. 507–510, 2000.
- [100] Y. Mita, Y. Nisida, K. Suito, A. Onodera, and S. Yazu, "Photochromism of H₂ and H₃ centres in synthetic type Ib diamonds," *J. Phys. Cond. Matter* **2**(43), pp. 8567–8574, 1990.
- [101] S. C. Lawson, G. Davies, A. T. Collins, and A. Mainwood, "The 'H₂' optical-transition in diamond: the effects of uniaxial stress perturbations, temperature and isotopic substitution," *J. Phys. Cond. Matter* **4**, pp. 3439–3452, Mar. 1992.
- [102] R. Jones, V. J. B. Torres, P. R. Briddon, and S. Öberg, "Theory of nitrogen aggregates in diamond: the H₃ and H₄ defects," *Mater. Sci. Forum* **143-147**(1), pp. 45–50, 1994.
- [103] I. Z. Machi, S. H. Connell, J. P. F. Sellschop, and K. Bharuth-Ram, "Interaction of muons with H₂/H₃-centres in diamond," *Hyperfine Interactions* **136–137**, pp. 727–730, 2001.
- [104] P. Humble, "The structure and mechanism of formation of platelets in natural type Ia diamond," *Proc. R. Soc. London, Ser. A* **381**, pp. 65–81, 1982.
- [105] J. P. Goss, "Theory of hydrogen in diamond," *J. Phys. Cond. Matter* **15**, p. R551, 2003.

- [106] S. Chawla and R. P. Messmer, “Hyperfine properties of bond-center muonium and hydrogen in diamond,” *Appl. Phys. Lett.* **69**, pp. 3251–3253, November 1996.
- [107] G. L. Bendazzoli and O. Donzelli, “UHF calculations of hyperfine coupling constants of anomalous muonium in C, Si and Ge,” *J. Phys. Cond. Matter* **1**, pp. 8227–8234, 1989.
- [108] N. Paschedag, H. U. Suter, Dj. M. Maric, and P. F. Meier, “Configuration interaction calculation of hyperfine properties for bond-centered muonium in diamond,” *Phys. Rev. Lett.* **70**, pp. 154–157, January 1993.
- [109] T. Miyazaki, H. Okushi, and T. Uda, “Shallow donor state due to nitrogen-hydrogen complex in diamond,” *Phys. Rev. Lett.* **88**(6), p. 066402, 2002.
- [110] J. P. Goss, P. R. Briddon, R. Jones, and M. I. Heggie, “Platelets and the $\langle 110 \rangle_{a_0/4}$ {001} stacking fault in diamond,” *Phys. Rev. B* **73**(11), p. 115204, 2006.
- [111] S. D. Berger and S. J. Pennycook, “Detection of nitrogen at {100} platelets in diamond,” *Nature* **298**, pp. 635–637, 1982.
- [112] P. J. Fallon, L. M. Brown, J. C. Barry, and J. Bruley, “Nitrogen determination and characterization in natural diamond platelets,” *Phil. Mag. A* **72**(1), pp. 21–37, 1995.
- [113] J. Bruley, “Detection of nitrogen at {100} platelets in a type IaA/B diamond,” *Phil. Mag. Lett.* **66**(1), pp. 47–56, 1992.
- [114] S. G. Clackson, M. Moore, J. C. Walmsley, and G. S. Woods, “The relationship between platelet size and the frequency of the B’ infrared absorption peak in type Ia diamond,” *Phil. Mag. B* **62**(2), pp. 115–128, 1990.
- [115] K. H. Chow, B. Hitti, R. F. Keifl, R. L. Lichti, and T. L. Estel, “Muonium analog of hydrogen passivation: Observation of the $\text{Mu}^+ \text{-Zn}^-$ reaction in GaAs,” *Phys. Rev. Lett.* **87**(21), p. 216403, 2001.

- [116] R. Jones, J. P. Goss, and P. R. Briddon, “Acceptor level of nitrogen in diamond and the 270-nm absorption band,” *Phys. Rev. B* **80**(3), p. 033205, 2009.
- [117] K. M. Etmimi, M. E. Ahmed, P. R. Briddon, J. P. Goss, and A. M. Gsiea, “Nitrogen-pair paramagnetic defects in diamond: A density functional study,” *Phys. Rev. B* **79**(20), p. 205207, 2009.
- [118] C. E. Melton, “Experimental evidence that oxygen is the principal impurity in diamond,” *Nature* **263**, pp. 309–310, 1976.
- [119] J. Ruan, W. J. Choyke, and K. Kobashi, “Oxygen-related centers in chemical vapor deposition diamond,” *Appl. Phys. Lett.* **60**(12), pp. 1379–1381, 1993.
- [120] Y. Mori, N. Eimori, H. Kozuka, Y. Yokota, H. Moon, J. S. Ma, T. Ito, and A. Hiraki, “Oxygen diffusion into diamond induced by hydrogen microwave plasma,” *Appl. Phys. Lett.* **60**(1), pp. 47–49, 1992.
- [121] C. A. J. Ammerlaan, *Semiconductors*, vol. III22b of *Landolt-Börnstein, New Series*. Springer, Berlin, 1998.
- [122] K. Iakoubovskii and A. Stesmans, “Dominant paramagnetic centers in ^{17}O -implanted diamond,” *Phys. Rev. B* **66**(4), p. 045406, 2002.
- [123] A. Gali, J. E. Lowther, and P. Deák, “Defect states of substitutional oxygen in diamond,” *J. Phys. Cond. Matter* **13**, pp. 11607–11613, 2001.
- [124] J. P. Goss, P. R. Briddon, M. J. Rayson, S. J. Sque, and R. Jones, “Vacancy-impurity complexes and limitations for implantation doping of diamond,” *Phys. Rev. B* **72**(3), p. 035214, 2005.
- [125] C. D. Clark, R. W. Ditchburn, and H. B. Byer, “The absorption spectra of natural and irradiated diamonds,” **237**, pp. 75–89, 1956.
- [126] P. E. Klingsporn, M. D. Bell, and W. J. Leivo, “Analysis of an electron spin resonance spectrum in natural diamonds,” *J. Appl. Phys.* **41**(7), pp. 2977–2980, 1970.

- [127] M. Y. Shcherbakova, E. V. Sobolev, and V. A. Nadolinny, “Electronic paramagnetic resonance of low-symmetry impurities centers in diamond,” *Dokl. Akad. Nauk SSSR [Sov. Phys. Dokl.]* **17**(6), pp. 513–516, 1972.
- [128] C. C. P. Madiba, J. P. F. Sellschop, J. A. Van Wyk, and H. J. Annegarn, “Light volatiles in synthetic diamond analyzed by ion probes,” *Nucl. Instrum. Methods B* **35**, pp. 442–445, DEC 1988.
- [129] D. A. C. Mcneil and M. C. R. Symons, “Electron spin resonance spectra of two naturally occurring paramagnetic centres in diamond,” *J. Phys. Chem. Solids* **38**, p. 397, 1977.
- [130] R. J. Eyre, J. P. Goss, P. R. Briddon, and M. G. Wardle, “Multi-impurity complexes for n-type diamond: a computational study,” *Phys. Status Solidi A* **204**(9), pp. 2971–2977, 2007.
- [131] J. E. Lowther, “Substitutional oxygen-nitrogen pair in diamond,” *Phys. Rev. B* **67**, p. 115206, 2003.
- [132] J. M. Baker and M. E. Newton, “Nitrogen in diamond studied by magnetic resonance,” *Appl. Magn. Reson.* **8**, pp. 207–228, 1995.
- [133] N. Casanova, E. Gheeraert, C. Deneuville, A. and Uzan-Saguy, and R. Kalish, “ESR study of phosphorus implanted type IIa diamond,” *Phys. Status Solidi A* **181**, pp. 5–10, 2000.
- [134] M. E. Zvanut, W. E. Carlos, J. A. Freitas, Jr., K. D. Jamison, and R. P. Hellmer, “Identification of phosphorus in diamond thin films using electron paramagnetic-resonance spectroscopy,” *Appl. Phys. Lett.* **65**, pp. 2287–2289, Oct. 1994.
- [135] J. Isoya, M. Katagiri, T. Umeda, S. Koizumi, H. Kanda, N. Son, A. Henry, A. Gali, and E. Janzn, “Pulsed EPR studies of phosphorus shallow donors in diamond and SiC,” *Physica B* **376-377**, pp. 358 – 361, 2006.

- [136] M. Katagiri, J. Isoya, S. Koizumi, and H. Kanda, “Electron paramagnetic resonance study of phosphorus-doped n-type homoepitaxial diamond films grown by chemical vapor deposition,” *Phys. Status Solidi A* **203**(13), pp. 3367–3374, 2006.
- [137] B. Butorac and A. Mainwood, “Symmetry of the phosphorus donor in diamond from first principles,” *Phys. Rev. B* **78**, p. 235204, Dec 2008.
- [138] R. Jones, J. E. Lowther, and J. Goss, “Limitations to n-type doping in diamond: the phosphorus-vacancy complex,” *Appl. Phys. Lett.* **69**(17), pp. 2489–2491, 1996.
- [139] J. M. Baker, J. A. van Wyk, J. P. Goss, and P. R. Briddon, “Electron paramagnetic resonance of sulfur at a split-vacancy site in diamond,” *Phys. Rev. B* **78**(2), p. 235203, 2008.
- [140] J. P. Goss, R. Jones, S. J. Breuer, P. R. Briddon, and S. Öberg, “The twelve-line 1.682 eV luminescence center in diamond and the vacancy-silicon complex,” *Phys. Rev. Lett.* **77**(14), pp. 3041–3044, 1996.
- [141] R. M. MacLeod, S. W. Murray, J. P. Goss, P. R. Briddon, and R. J. Eyre, “Model thermodynamics and the role of free-carrier energy at high temperatures: Nitrogen and boron pairing in diamond,” *Phys. Rev. B* **80**(5), p. 054106, 2009.